



# Identification of Fatigue and Resonance Frequency Influencing Parameters of an Offshore Wind Turbine via Data Analysis of Real Measurements

Mikk Laanes

May 12, 2021



# Identification of Fatigue and Resonance Frequency Influencing Parameters of an Offshore Wind Turbine via Data Analysis of Real Measurements

Master of Science Thesis

**Author:** Mikk Laanes

**Committee:**

Prof. A.V. Metrikine	TU Delft - Chairman
Asst. Prof. F. Pisano	TU Delft
Asst. Prof. E.-M Lourens	TU Delft
Ir. E. Kementzetzidis	TU Delft
Dr. P. Verstijlen	Siemens Gamesa Renewable Energy
Dr. A. Iliopoulos	Siemens Gamesa Renewable Energy
Ir. S. Panagoulas	Siemens Gamesa Renewable Energy

May 12, 2021



# Summary

Technology improvements and growing maturity of the offshore wind industry have resulted in significant cost reductions and rise in demand. More can be achieved by focusing on improving the understanding of key design areas of an offshore wind turbine (OWT). Since fatigue is one of the main design criteria for offshore structures and little is known about fatigue cumulative development in time under operating conditions, it formed the basis of this thesis. However, fatigue is a complex phenomenon that is dependent on numerous interlinked parameters, such as damping, loading type, and stiffness of support structure (SUS).

For the purpose, data analysis was performed on measurements which were gathered over a period of four years from a monopile-supported OWT site. The measurement data included information about the environmental and operational conditions of the OWT; and strain, acceleration and inclinometer readings from its SUS.

Use of different data acquisition systems during the measurement campaign inherently required significant efforts to synchronise and preprocess raw data to appropriate state for data analysis. Time-dependent lag was identified via computation of cross-correlation sequences between data segment pairings, and the lag was successfully corrected.

With the use of a standardized rainflow cycle counting algorithm, strain-derived moment time series were converted to constant amplitude events, which could be used to derive damage equivalent bending moments, M-N curves and fatigue damage accumulation frequency spectra.

Short-term damage equivalent bending moment (STEL) was revealed to have a linear dependency with turbulence intensity when the OWT was in the run-up operational state. Additionally, the fatigue damage was demonstrated to be higher for downstream turbines due to wake effects. Also, fatigue life consumption of OWT SUS increases above rated wind speed conditions despite decrease in load magnitude due to increase in SUS response frequency.

The latter was confirmed with fatigue damage accumulation frequency spectra, which revealed that the importance of high frequency band (1 – 5 Hz) increases in conjunction with wind speed at above rated wind speed conditions. However, most of the overall fatigue damage is accumulated at the low frequency band, which associated with wind and wave loading, first SUS bending modes, 1P and 3P rotor harmonics.



# Acknowledgements

I would like give a special thanks to Ir. Stavros Panagoulas and Dr. Alexandros Iliopoulos for their great supervision and guidance throughout my thesis. Their advice helped to resolve many of the encountered obstacles and made a big difference in the final outcome of this project.

Also, I would like to express my gratitude to Dr. Pim Versteijlen and Dr. Federico Pisanò for their help and introducing me to the opportunity of carrying out my master's thesis with SGRE.

Moreover, I grateful for occasional brainstorming sessions with Ir. Evangelos Kementzetzidis and shared words of wisdom that helped to keep the project on the correct track.

Additionally, I am grateful that Dr. Andrei Metrikine accepted to be the Chairman of my graduation committee and that Dr. Eliz-Mari Lourens accepted to join the committee as well. It has been a joy puzzling over the committee's comments, questions and suggestions.

Furthermore, I would extend my thanks to all colleagues at SGRE for the pleasant working atmosphere and their willingness to take a bit of time out of their busy schedules to help or share some fascinating ideas.

Lastly, the support of my family and friends has been invaluable.





# Contents

<b>Summary</b>	<b>i</b>
<b>Acknowledgements</b>	<b>ii</b>
<b>List of Figures</b>	<b>vii</b>
<b>List of Tables</b>	<b>x</b>
<b>Nomenclature</b>	<b>xiii</b>
<b>1 Introduction</b>	<b>1</b>
1.1 Motivation . . . . .	1
1.1.1 Rise of Renewable Energy . . . . .	1
1.1.2 Offshore Wind Industry . . . . .	2
1.1.3 Joint Industry Project - DISSTINCT . . . . .	3
1.1.4 Problem Analysis . . . . .	4
1.2 Objective . . . . .	6
1.3 Scope & Approach . . . . .	7
1.4 Outline . . . . .	8
<b>2 Data Acquisition &amp; Synchronisation</b>	<b>9</b>
2.1 Data Availability . . . . .	9
2.1.1 RNA Data . . . . .	9
2.1.2 Support Structure Data . . . . .	11
2.1.3 Soil Data . . . . .	11
2.1.4 Data Availability Timeline . . . . .	13
2.2 Synchronisation of Datasets . . . . .	13
2.2.1 Methodology . . . . .	14
2.2.2 Synchronisation of RNA Data and Support Structure Data . . . . .	15
2.2.3 Synchronisation of Soil Data and Support Structure Data . . . . .	24
2.2.4 Synchronisation of RNA Data and Soil Data . . . . .	31
2.3 Summary & Discussion . . . . .	32
<b>3 Data Analysis</b>	<b>35</b>
3.1 Performance Curves & Operational States . . . . .	35
3.2 Wind Speed, Damping & Resonance Frequency Dependencies . . . . .	37
3.3 Wind Turbine Tilt Analysis . . . . .	40
3.4 Moment Lines . . . . .	44

3.4.1	Calculation of Moments from Strain & Sign Convention . . . . .	44
3.4.2	Determining Usability of Resistive Strain Sensors . . . . .	46
3.4.3	Additional Assumptions and Preprocessing for Derivation of Bending Moments . . . . .	50
3.4.4	Results and Comparison with Design Values . . . . .	51
3.5	Fatigue Analysis . . . . .	54
3.5.1	The Rainflow Counting Method . . . . .	54
3.5.2	M-N Curves in Characteristic Operational States . . . . .	55
3.5.3	Damage Equivalent Load Curves . . . . .	57
3.5.4	Short-Term Damage Equivalent Load Relation with Wind Speed & Turbulence Intensity . . . . .	58
3.5.5	Fatigue Damage Frequency Spectrum . . . . .	61
3.6	Summary & Discussion . . . . .	64
<b>4</b>	<b>Conclusions &amp; Recommendations</b>	<b>67</b>
4.1	Conclusions . . . . .	67
4.2	Recommendations . . . . .	69
	<b>Bibliography</b>	<b>71</b>

# List of Figures

1.1	Boxplot of LCoE by technology. . . . .	2
1.2	Predicted global offshore wind growth to 2030. . . . .	3
1.3	Location of the Westermeerwind wind farm in the Netherlands. . . . .	4
1.4	Overview of external loads acting on an OWT, along with characteristic waveforms. . . . .	5
1.5	Generalised overview of forcing frequencies against power spectral density for a three-bladed wind turbine. . . . .	6
2.1	Positioning of RNA and support structure data sensors: strain gauges, accelerometers and an inclinometer. . . . .	10
2.2	Positioning of soil sensors with respect to W27 and with respect to the OWT and the orientation of strain gauges in monopile foundation. . . . .	12
2.3	Example of resampling with linear interpolation. . . . .	14
2.4	"July 2017" study period 10-minute statistics comparison - standard deviation of SUS acc. 3 readings and RNA FA acceleration. . . . .	16
2.5	RNA 10-minute average - wind direction, yaw positioning, and operational status of W27 for the period 02/07/2017 17:00:00 - 06/07/2017 18:40:00. . . . .	17
2.6	10-minute snippet of RNA acceleration recording transformed to acc. 3 orientation, with the S-transform of the corresponding signal, from the "July 2017" study period. . . . .	18
2.7	10-minute snippet of SUS acc. 3 recording, with the S-transform of the corresponding signal, from the "July 2017" study period. . . . .	18
2.8	OWT lowest frequency design position model 1 <sup>st</sup> , 2 <sup>nd</sup> and 3 <sup>rd</sup> mode shapes. . . . .	19
2.9	Scaled, bandpass filtered and lag-corrected support structure and RNA Acc3-oriented acceleration signals overlain. . . . .	19
2.10	Zoomed in from Fig. 2.9: scaled, bandpass filtered and lag-corrected support structure and RNA Acc3-oriented acceleration signals overlain . . . . .	20
2.11	July period lag identification study results from the filtered and scaled Acc3-oriented signal pairing. . . . .	20
2.12	July period lag identification study results from the filtered and scaled Acc3-oriented signal pairing after lag correction. . . . .	23
2.13	RNA FA acceleration 10-min standard deviation and lag-corrected SUS acc. 3 data 10-min standard deviation development over time. . . . .	23
2.14	August period 10-minute statistics comparison - standard deviation of SUS Acc1, soil VP-19 Acc-X, and VP-20 Acc-X accelerations. . . . .	25
2.15	10-minute snippets of SUS and soil recordings, with the S-transform of the corresponding signal, from the "August 2017" study period. . . . .	26
2.16	OWT lowest frequency design position model 1 <sup>st</sup> , 2 <sup>nd</sup> and 3 <sup>rd</sup> mode shapes. . . . .	27

2.17	Normalised, bandpass filtered and lag-corrected Acc1 and VP-19 Acc-X acceleration signals overlain. . . . .	28
2.18	Zoomed in from Fig. 2.17: scaled, bandpass filtered and lag-corrected Acc1 and VP-19 Acc-X acceleration signals overlain . . . . .	28
2.19	August period lag identification study results from the filtered and scaled VP19 X-directional displacement and SUS gauge 5C signal pairing. . . . .	29
2.20	10-minute average wind speed and rotor speed development over the "August 2017" lag identification study period. . . . .	29
2.21	August period lag identification study results from the filtered and scaled VP19 X-directional displacement and SUS gauge 5C signal pairing after the application of lag correction. . . . .	31
2.22	August period 10-minute statistics comparison - standard deviation of RNA FA acceleration, and soil sensors VP-19 and VP-20 X-directional accelerations . . . .	32
2.23	August 2017 period 10-minute statistics comparison - standard deviation of RNA FA acceleration, SUS Acc1, and soil sensor VP-19 Acc-X readings . . . . .	33
3.1	Performance curves based on RNA 10-minute statistical data. . . . .	36
3.2	10-min average resonance frequency <i>versus</i> wind speed at the defined OWT operational states . . . . .	38
3.3	(a) 10-min average SS logarithmic decerment estimate <i>versus</i> wind speed at the defined production conditions; (b) the average decrement values per wind speed range, data points are located at the centre of the respective wind speed bin. . . .	38
3.4	Average resonance frequency per wind speed range at the defined conditions, data points located at the centre of wind speed bin values. Based on values presented in Fig. 3.2 . . . . .	39
3.5	(a) Sketch of the tilting of the OWT along the $39.4^\circ - 219.4^\circ$ line according to data statistics, and a visualization of the sign convention of the inclinometer and the considered wind directions; (b) 10-min average inclination <i>versus</i> 10-min mean wind speed, only values corresponding to the wind directions $39.4^\circ \pm 20^\circ$ and $219.4^\circ \pm 20^\circ$ are included . . . . .	41
3.6	(a) Change in tilt of the OWT over time at conditions where 10-min $n_{max} < 2rpm$ and the 10-min $V_m < 2m/s$ and wind direction is $219.4 \pm 20^\circ$ , according to 10-min statistical values; (b) change in gauge 8A 10-min average strain values over the same time instants. . . . .	42
3.7	(a) Tilt and (b) strain development at the data cluster on 24/07/2016. . . . .	43
3.8	(a) 10-min average wind direction and resonance frequency development over the same time instants as in Fig. 3.6a; (b) values at the data cluster on 24/07/2016. .	44
3.9	10-min average, minimum and maximum wind direction development at the data cluster on 24/07/2016. . . . .	44
3.10	(a) Sketch on the adopted sign convention for bending moments; (b) positioning of the strain gauges; and (c) the local coordinate system for deriving FA and SS moments, drawn on the top view of the RNA. . . . .	45
3.11	Gauge 8C 10-min average strain values plotted against respective 10-min average yaw position, per wind speed range. . . . .	46
3.12	Gauge 4C 10-min average strain values plotted against respective 10-min average yaw position, per wind speed range. . . . .	47

3.13	The development of strain gauges 4C and 8C 10-min average values over time per indicated wind speed ranges, in conditions where wind direction is $219.4^\circ \pm 20^\circ$ .	47
3.14	Drifting strain gauge 4C 10-min average values over time, in conditions where 10-min average wind direction is $219.4^\circ \pm 20^\circ$ or $39.4^\circ \pm 20^\circ$ and wind speed is 10-14 m/s. . . . .	48
3.15	Non-drifting strain gauge 8C 10-min average values over time, in conditions where 10-min average wind direction is $219.4^\circ \pm 20^\circ$ or $39.4^\circ \pm 20^\circ$ and wind speed is 10-14 m/s. . . . .	49
3.16	Summary of the adjustments and assumption made to derive moments from gauge data at each ring level, only gauges located at rings 5, 6, 8 and 9 can be used to derive $M_{FA}$ and $M_{SS}$ due to no apparent drifting in their readings. . . . .	50
3.17	(a) Sine curve estimate to the curve formed from gauge 8C 10-min average values (at wind speeds 10-14 m/s) <i>versus</i> yaw position scatter plot. (b) Offset corrected strain <i>versus</i> yaw position relation per wind speed range. . . . .	51
3.18	Ratio of $M_{8FA}$ and $M_{9FA}$ 10-min average moment values <i>versus</i> 10-min average yaw position value. . . . .	52
3.19	Approximated maximum moment lines, compiled with values from Table 3.3. . .	52
3.20	Comparison between approximated maximum moment line and design ULS moment line for the case with unfactored soil. . . . .	52
3.21	10-min average bending moment <i>versus</i> wind speed at ring 8 (6.95 m above NAP). . .	53
3.22	FA and SS motion M-N curves, from readings at ring 6 (-10.15 m NAP). . . . .	55
3.23	FA and SS motion M-N curves, from readings at ring 6, composed with data records corresponding to (a) all ; (b) rated; (c) run-up; (d) idling operational states. . . . .	56
3.24	M-N curves, from readings at ring 6, composed with data records corresponding to rated, run-up, and idling operational states. . . . .	57
3.25	Damage equivalent bending moment curves. . . . .	58
3.26	STEL values at run-up operational state in approximated FA motion conditions <i>versus</i> turbulence intensity. . . . .	59
3.27	(a) Overivew of the 1 <sup>st</sup> order lines fitted to the $M_{BD,STEL}$ <i>versus</i> $TI$ scatter plots, where only data points corresponding to run-up operational state in approximated FA motion conditions were considered; (b) the slopes of the fitted lines plotted over the height of the SUS. . . . .	59
3.28	FA and SS average STEL values per wind speed range at levels 5, 6, 8 and 9; data points are located at the centre of the chosen wind speed bins. . . . .	60
3.29	FA and SS fatigue damage accumulation frequency spectra at rings 6 (-10.15 m above NAP) and 8 (6.95 m above NAP). . . . .	61
3.30	$M_{6FA,DEL}$ accumulation frequency spectra at specified wind speed conditions. . .	62
3.31	$M_{6SS,DEL}$ accumulation frequency spectra at specified wind speed conditions. . .	62
3.32	$M_{6SS,DEL}$ and $M_{8SS,DEL}$ accumulation frequency spectra at specified wind speed conditions. . . . .	63
3.33	OWT lowest frequency design position model 1 <sup>st</sup> , 2 <sup>nd</sup> and 3 <sup>rd</sup> mode shapes. . . .	63



# List of Tables

2.1	Data availability timeline . . . . .	12
2.2	Results from the application of the cross-correlation based lag identification procedure on the considered study periods. . . . .	21
2.3	Lag increase rates in-between studied periods according to the found mid-period lag values. . . . .	21
2.4	Chosen parameters for lag correction of the support structure data. . . . .	22
2.5	SUS and soil data lag identification results from 20 pairings. . . . .	30
3.1	OWT design parameters: $V_{rated}$ , $V_{in}$ , $V_{out}$ , $P_{rated}$ . . . . .	35
3.2	Definitions of W27 OWT states . . . . .	37
3.3	Summary of the results from the process of deriving approximate maximum moment values from 10-min statistics of strain data for the purpose of verifying the usability of strain sensors for further analysis. . . . .	49
3.4	Comparison between peak moment values derived from ‘hand-picked’ strain data values, and from the 10-min average $M_{FA}$ and wind speed scatter plots, for rings 5, 6, 8, and 9. . . . .	53





# Nomenclature

## Latin symbols

$C$	damping matrix	
$K$	stiffness matrix	
$M$	mass matrix	
$A$	strain gauge location - $39.4^\circ$	
$B$	strain gauge location - $309.4^\circ$	
$C$	strain gauge location - $219.4^\circ$	
$D$	strain gauge location - $129.4^\circ$	
$E$	modulus of elasticity	$\frac{N}{m^2}$
$I$	second moment of area	$m^4$
$L$	pile penetration depth	$m$
$M$	bending moment	$Nm$
$n$	rotor speed	$rpm$
$P$	power	$kW$
$r$	radius	$m$
$V$	wind speed	$\frac{m}{s}$
$x_n$	stationary random process	
$x_u$	distance between centre of pile and strain gauge along x-axis	$m$
$y_n$	stationary random process	
$y_u$	distance between centre of pile and strain gauge along y-axis	$m$

## Greek symbols

$\alpha$	angular position	$^\circ$
$\delta$	logarithmic decrement	
$\delta\epsilon$	change in strain	$\frac{m}{m}$
$\epsilon$	strain	$\frac{m}{m}$
$\psi$	constant of proportionality	
$\sigma$	standard deviation	
$\tau$	constant of proportionality	
$C_{ref}$	constant lag correction value	<i>minute</i>
$R_{cor}$	lag correction rate	$\frac{s}{day}$

*s* signal prior to min-max scaling  
*s'* min-max scaled signal

### Subscripts

*AC* with respect to 39.4° – 219.4° line  
*b* number of bins  
*BD* with respect to 129.4° – 309.4° line  
*cor* correction  
*DEL* damage equivalent load  
*FA* fore-aft  
*in* cut-in  
*max* 10-minute record maximum value  
*min* 10-minute record minimum value  
*out* cut-out  
*RNA* related to rotor nacelle assembly data  
*SS* side-side  
*STEL* short-term damage equivalent load  
*SUS* related to support structure data

### Superscripts

\*

*m* Wöhler curve slope

### Abbreviations

1P Frequency of the rotor  
3P Blade passing (tower) frequency  
Acc Acceleration  $\frac{m}{s^2}$   
acc. accelerometer  
API American Petroleum Institute  
ASTM American Society for Testing and Materials  
CCF Cross-Correlation Function  
CPT Cone Penetration Test  
DAQ Data Acquisition  
DEL Damage Equivalent Load  
dir. direction  
DNV Det Norske Veritas  
FA Fore-Aft  
GMT Greenwich Mean Time  
incl. inclinometer  
ISO The International Organization for Standardization

LAT	Lowest Astronomical Tide
LCoE	Levelized Cost of Energy
M-N	Moment range <i>versus</i> Number of cycles
NAP	Normal Amsterdam Level
No.	Number
OWT	Offshore Wind Turbine
PISA	Pile Soil Analysis project
RNA	Rotor Nacelle Assembly
S-N	Stress range <i>versus</i> Number of cycles
s.p.	Study period
SCADA	Supervisory Control And Data Acquisition
SCPT	Seismic Cone Penetration Test
SS	Side-Side
SSI	Soil-structure interaction
std	standard deviation
STEL	Short-Term Damage Equivalent Load
STFT	Short-Time Fourier Transform
Str.	Strain gauge
SUS	Support Structure
TI	Turbulence Intensity
ULS	Ultimate Limit State
VP	Soil sensor
W27	Monitored and studied offshore wind turbine



# Chapter 1

## Introduction

*This first chapter provides background for the rise of renewables; the offshore wind industry and the uncertainties in OWT design. The objectives are introduced in the second section, as the scope and approach are described in the third section. The chapter is finalized with an outline of the structure of this report.*

### 1.1 Motivation

#### 1.1.1 Rise of Renewable Energy

An unprecedented year with the constant evolution of the COVID-19 pandemic has imposed significant changes in the global energy demand, which is approximated to be around 6% lower than in previous year [5]. The main culprits being reduced mobility and economic activity, together with the required lock-downs around the world. During the year, signs of longer-lasting implications for the energy transition away from fossil fuels became evident [5, 17].

In April 2020 the high economic volatility of fossil fuel was exemplified by the price of oil turning negative for the first time in history, just after the first hit of the pandemic when lock-downs were ordered and demand for oil plummeted. Although its prices have recovered to a stable, but lower, level, more reliable renewable energy sources rose into bigger demand [31].

Because of low operating costs and preferential access to many power systems renewable energy demand has been estimated to have grown by 1% compared to 2019 levels, in contrast to all other energy sources [20]. Similarly can be viewed the generation of energy proportions. Thus, renewable energy has demonstrated to be the most resilient energy source to COVID-19 lock-down measures [20].

What is more, the European Union remained on track to reach its 20% renewables target by 2020 and EU leaders endorsed a plan to achieve 55% - up from previous 40% - cut in greenhouse gas emissions by 2030, compared to 1991 levels. The latter decision came as part of a broader European Green Deal programme, which aims to reach climate neutrality by 2050. A big part of the programme involves phasing out fossil fuels for renewable sources like wind energy [12].

Additionally, over the years it has been observed that newly installed renewable power capacity increasingly costs less than the cheapest power generation options based on fossil fuels, if the Levelized Cost of Electricity (LCoE) is viewed (see Fig. 1.1). LCoE is the ratio of lifetime costs to lifetime electricity generation - a parameter often used to compare the cost of different sources of energy [22]. Lifetime costs refer to the expenditures related to building and operating the power generating asset. However, the LCoE does not capture the whole picture and continuing

to find cost-outs from the renewable energy sources is required to make low-cost climate and decarbonisation solutions more appealing [22, 2].

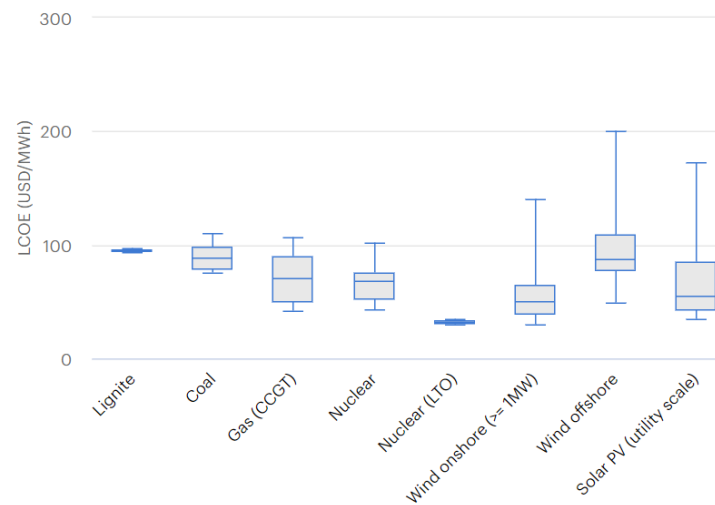


**Figure 1.1:** Boxplot of LCoE by technology.

Note: Values at 7% discount rate. Box plots show maximum, median and minimum values, the boxed area represents central 50% of values. Source: [2]

### 1.1.2 Offshore Wind Industry

Offshore wind could be seen, from Fig. 1.1, to produce clean electricity that sometimes is cheaper than existing fossil fuel-based technology – more often so, as time has gone by. Over the last few decades offshore wind energy technology has advanced significantly - a single offshore wind turbine now possesses more capacity than two of the world’s first offshore wind parks together [13]. Turbines can be made larger, blades longer, hub height higher, and site locations farther from offshore than ever before.

The previous year - 2020 - demonstrated that wind power is one of the energy sources that reduces the exposure of our economies to fuel price volatility. Despite pandemic-caused equipment supply disruptions and slowed construction due to lockdown measures, the impact of COVID-19 on offshore deployment remained limited. Although impact beyond 2021 may be of more significance, the global offshore wind market outlook to 2030 has grown more promising over the past year. Multiple governments have raised their ambition levels and new countries aspire to climb the ranks in the market shares. Japan set out a goal to increase offshore wind power generation up to 45 GW 2040 from the current level of 4 GW – leveraging Japan to 3rd largest offshore wind generator. Their set out plan estimated that the cost to generate electricity from offshore wind power is expected to become cheaper than thermal power energy around 2030 - 2035 [4].

Also, EU Strategy on Offshore Renewable Energy proposes to increase Europe’s offshore wind capacity from its current level of 12 GW to 300 GW by 2050 [11].

Offshore wind currently accounts for 5% of global wind energy and generates a mere 0.3% of global electricity production, but the potential for further growth is enormous[49, 13, 11]. Current estimates provide an average annual growth rate of 18.6 percent until 2024 and 8.2 per cent up to the end of the decade, as shown in Fig. 1.2.

Technology improvements and growing maturity of the industry have resulted a 29% decline

in the global weighted average LCoE of offshore wind between 2010 and 2019 [13]. Continued effort to seek further cost reductions can only improve the outlook of a sustainable future.

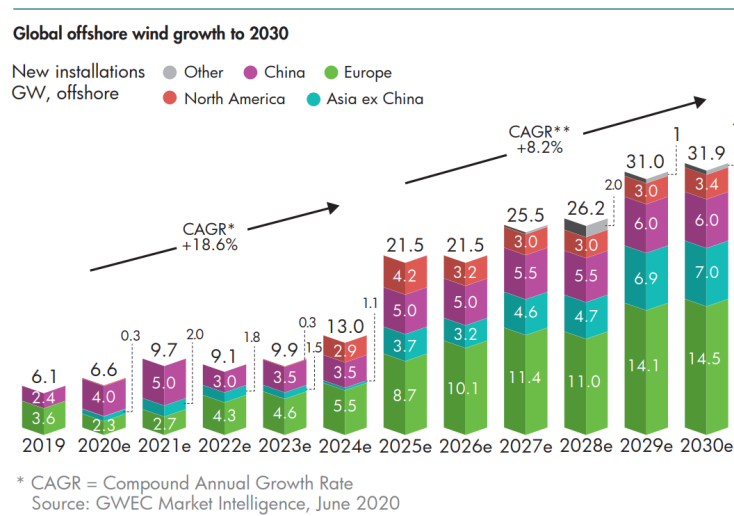


**Figure 1.2:** Predicted global offshore wind growth to 2030.

### 1.1.3 Joint Industry Project - DISSTINCT

Research is an integral part of seeking cost-outs: one of the examples is the DISSTINCT project - a 4-year joint industry research project of Siemens Wind Power BV, BMO Measurement Solutions BV, Fugro Geoservices, KEMA Nederland BV, Siemens Nederland NV, Delft University of Technology and DNV-GL aimed at improved dynamic soil characterization and modelling for offshore wind turbines [42]. The main contribution of this project was the development of the ‘Effective Stiffness method’ for the estimating the lateral stiffness of rigidly behaving piles [45]. The method was validated to predict the measured response of an in-situ monopile better than the conventional p-y curves, mainly developed in the 1960–1980s [47].

It was demonstrated that the developed stiffness method, provided a 8% saving potential for the primary steel (shell) mass of the complete offshore wind turbine support structure (MP, transition piece and tower). To be noted, fatigue driven base case was utilized for the exercise. Following the estimation of the MP support structures constituting more that 20% of the total capital cost of an offshore wind farm, the method provided a beneficial impact on the feasibility of future offshore wind projects [47].

The shaker measurement campaigns, carried out as part of the project, were performed in the Westermeerwind wind park in the Netherlands, in 2015 (see Fig. 1.3). The campaign included equipping a monopile-only installed structure with numerous strain gauges along its length, accelerometers and an inclinometer near the top of it, and a shaker for force-controlled excitation. Additionally, accelerometer probes were inserted in the surrounding soil of the monopile. The gathered measurement data has contributed to numerous research projects and revelations [25, 46, 47].

Since the installation of the wind farm in spring 2016, as a continuation of the DISSTINCT project, measurements continued to be collected from the operating wind turbines. Parts of this data - gathered over more than four years from the wind turbine that is circled in red in Fig. 1.3 - will be analysed in Ch. 3 of this thesis.

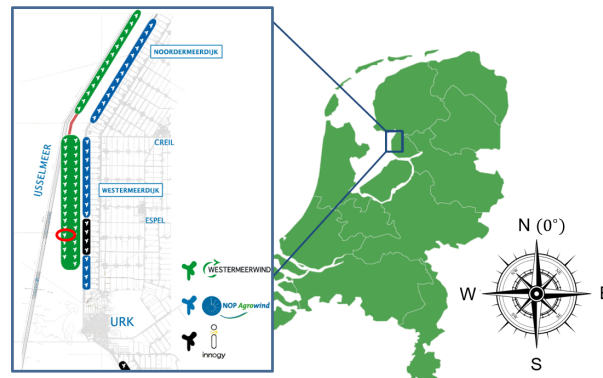


**Figure 1.3:** Location of the Westermeerwind wind farm in the Netherlands. Red circle indicates the testing site. Source: [47]

Rotor nacelle assembly (RNA) data originates from the supervisory control and data acquisition (SCADA) system, which is located at the RNA, at the level of the axel of the rotor at approximately 95 m NAP (see 2.1). The RNA data includes information about wind turbine operational state and surrounding environmental conditions – exact parameters can be found in Sec. 2.1.1.1.

Support structure (SUS) data has been acquired with a system commissioned by a company called HBM in March 2016. The installed measurement setup, which is depicted in Fig. 2.1, includes 36 strain gauges – eight on the tower and 28 on the inner wall of the monopile foundation –, three accelerometers and an inclinometer. More elaborate description of SUS data acquisition system is in Sec. 2.1.2.

Soil data comprises of soil parameter profiles from geotechnical and geophysical characterization – these can be found in [47, 45]. In general, the site is characterized by saturated and stiff sandy soil conditions – similar to sandy North Sea sites.[47]. Additionally, soil data involves soil acceleration and pore pressure measurement from eleven soil probes, which were placed at various depths and radial distances from the pile. The positioning of soil sensors (Fig. 2.2) and a more intricate information on soil DAQ system is provided in Sec. 2.1.3.

#### 1.1.4 Problem Analysis

Offshore wind turbines are structurally exposed to a variety of excitations, such as hydrodynamic loads, earth-induced loads, aerodynamic loads, loads from turbine dynamics (such as blade shadowing effects), and in the Northern regions ice loads [37]. Neglecting ice and earth-induced loading, the main loads wind, wave, 1P, and 3P have been schematized in Fig. 1.4. Each of these loads can be seen to have unique characteristics in amplitude and frequency. Wind and wave loads are stochastic and are thus often described statistically, whereas the 1P loading stems from mass and aerodynamic imbalances of the rotor [37]. Hence, 1P forcing frequency equals the rotational frequency of the rotor and 3P loading - caused by the blade shadowing effect - is 3 times the 1P frequency.

The combined effect of interactions between these excitations and the OWT leads to complex dynamics, with many uncertainties [28, 38]. Many of the uncertainties are related to the interaction between the surrounding soil and the OWT's foundation, which is mostly a monopile. Due to the 'simplicity' in construction and proven success of driven piles in supporting offshore oil and gas infrastructures, compared to other foundation types, monopile foundation has been



widely adopted [28, 21]. The proven track record has definitely now extended to offshore wind energy sector. In Europe, in 2019 70% of OWTs were constructed with a monopile, and above 75% during 2013 – 2018 [50].

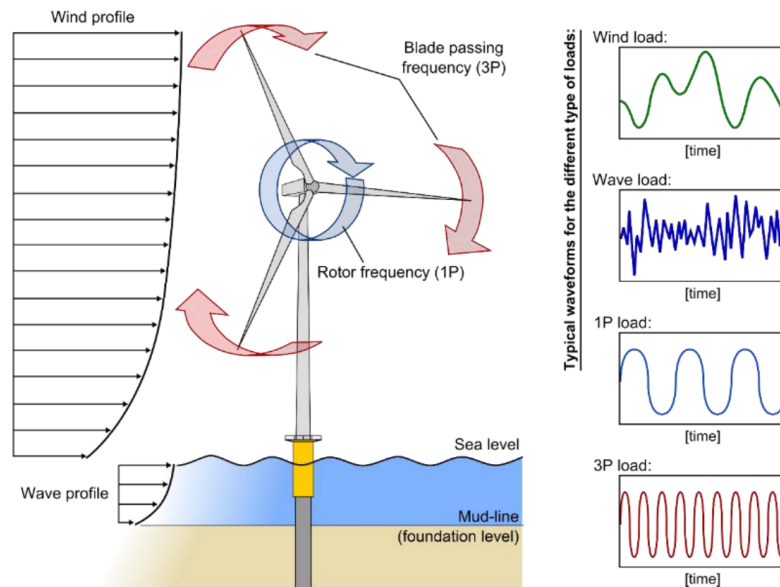


**Figure 1.4:** Overview of external loads acting on an OWT, along with characteristic waveforms.  
Source: [2]

However, the increase in diameter of monopiles for OWTs has led the designers to venture outside the original envelope of engineering knowledge from offshore oil and gas [28]. Hence, the recommended usage of p-y curves by the current codes of practice (for example API, ISO, DNV) for the design of monopile foundations of OWTs leads to conservative results. The reason being that the proposed formulation of the p-y curves is based on small-scale tests of slender piles ( $L/D$  ratio  $> 20$ ) under static loading for oil and gas application in the 1960s – 1980s [47]. A typical length to diameter ratio for a monopile would be less than seven – making the behaviour of pile more rigid [8].

The importance of accurately assessing the stiffness of the soil-structure system stems, among others, from the matter that the first eigenfrequency of the OWT can only lie in a relatively narrow band without causing detrimental damage to the structure. In general, it is economically optimum if the OWT first eigenfrequency is within a range called soft-stiff [3], as shown in Fig. 1.5. In such a manner, the resonance from wind, wave, 1P and 3P excitation frequencies is avoided. Soft-soft range would imply a rather flexible structure and stiff-stiff range a heavy and rigid structure [3]. If the natural frequency of the OWT structure was to fall into the excitation frequency bands, for instance via erroneous design methods, the lifeline would be compromised.

Fatigue is often the governing design parameter of OWTs, and consequently defines the turbine's age. The intended life time of an OWT is typically 25-30 years, but incorrect estimation of natural frequency of an OWT can shorten it significantly [28]. In monopile support structure, fatigue critical zones are located near or below the seabed, at the location of the highest bending moments. Typically the first welds beneath the sea bed are most fatigue critical [19]. Given the inherent conservatism of the p-y method, or other design assumptions, the real life fatigue progression in offshore monopile foundations will most probably differ from design. In case of the existing wind farms, decisions on lifetime extension are thus best supported by continuous

monitoring of the accumulated fatigue damage of the offshore wind turbine (OWT) [21]. For that, the complete distribution of stresses along the structure, especially at the fatigue hot-spots, should ideally be known. However, retrieving such information requires direct measurement of these hot-spot stresses – implying installation of strain gauges on the relevant structural parts, and the monopile prior to pile driving [41, 19]. Unfortunately, this is unfeasible to be done on existing OWTs and a costly activity for the future wind farms; hence rarely done. Examples of strain measurement campaigns, where also other types of data were collected, include the DISSTINCT project, but also the Nobelwind measurement campaign.

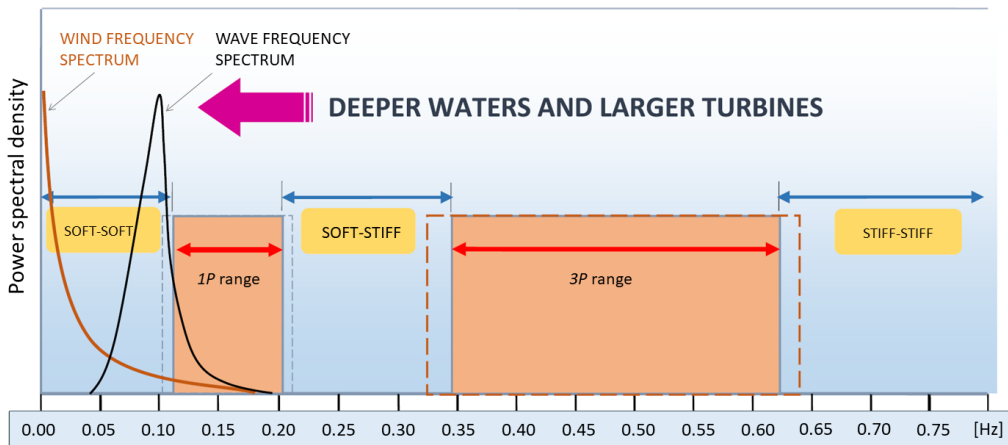


**Figure 1.5:** Generalised overview of forcing frequencies against power spectral density for a three-bladed wind turbine.

Source: [3]

It can be realized that strain data, coupled with RNA and soil data, from an operational OWT can provide invaluable insight with respect to uncertainties in soil-structure-environment interaction and associated dependencies, accumulated fatigue damage, as well as existing non-linearity effects in and around the support structure of the OWT. Eventually, measurements and data analysis allows to identify differences between design models and the reality at the cost-critical design points of the OWTs.

## 1.2 Objective

Since fatigue is one of the main design criteria for offshore structures and little is known about fatigue cumulative development in time under random loading [28, 23], it will form the basis of this thesis together with the data collected from an OWT in the Westermeerwind wind farm. To distil information about fatigue from the collected strain data, cumulative fatigue damage analysis procedures are to be employed. One of the procedures includes rainflow counting, which is widely used in practice and implemented in design codes. Therefore, the first objectives of the thesis can be formulated as follows:

*Preprocess measured data and evaluate the fatigue damage accumulation of a monopile-supported offshore wind turbine under normal operating conditions.*

However, fatigue is a complex phenomenon that is influenced by multiple of variables such as damping in the system, loading types, structural materials, imperfections and many more. Similarly it is influenced by the resonance frequency of the OWT. It is envisioned that the gathered data, which is introduced in Chapter 2, allows to provide insight to the underlying relations between fatigue, resonance frequency, and environmental and operational conditions. Thus, the second objective of this thesis:

*Identify qualitatively the parameters that influence the fatigue accumulation and the resonance frequency of a monopile-supported offshore wind turbine.*

### 1.3 Scope & Approach

Fatigue and data analysis are topics with a broad spectrum and herein it is tried to define the scope of the current work and additionally outline the chosen approach to arrive at the objectives.

The available data has been gathered as part of a joint industry project and consequently different data acquisition (DAQ) systems from different companies were used for data collection. Inherently, synchronization of the three available data sets will be needed as part of the preprocessing to ensure that relevant info can be extracted from the same point in time for the purpose of combining data and exploring dependencies as part of both objectives. During the synchronization, it is anticipated that the usability of sensor readings becomes apparent. It is known that resistance strain gauges, which were also used, are susceptible to drifting over a longer measurement period. Hence, the scope of data preprocessing would be limited to synchronization, identification of abnormal readings and drifting in readings, and interpolating data to a common sampling frequency – if possible.

To reach the first objective of assessing the fatigue damage accumulation, several steps are required. The measured strain readings would need to be converted to stresses and bending moments via laws of classical mechanics. The calculated moment-time histories are random, and calculating the number of moment or stress cycles and ranges, which are required for advancement, is required. Hence, in order to relate a moment sequence to the damage it inflicts to the material a standard cycle counting algorithm – rainflow counting – is going to be applied on the moment-time history. Having shrunk a complex stress and bending moment histories into a series of counted constant amplitude events, the most widely used S-N or M(moment)-N curves can be constructed for different operational states of the OWT. Furthermore, post-processing of counted results lead to damage equivalent loads (DELs) – constant load values that represent the damage that is caused by a time varying load over a certain period of time.

The aim behind making the M-N curves and calculating DELs, is to make the measurement data relatable with the design parameters used in the design guidelines and models. This would provide an opportunity to identify discrepancies between the real world and design models. Additional elements in the scope of fatigue analysis are the assessment of the spectral content of accumulated fatigue damage and investigation of short-time damage equivalent loads, which are determined from ten-minute recordings of the bending moments. The spectral content is of particular interest as it shows the frequency characteristics of the loads causing the highest contribution to the fatigue damage.

The information of resonance frequency of an OWT is included in the recordings terms of 10-minute average data points. Having followed the previous steps, the relations between different types of data are sought through trial. Focus will be given to identifying if the turbine has tilted

with the usage of inclinometer data. To add, given the large amount of data, clustering and prioritization of data points will be required.

To identify OWT characteristic operational and environmental conditions, well-known performance curves, for example wind speed – rotor speed curve, would be formed with the use of RNA data. Additionally, behaviour of the OWT can be studied with the usage of performance curves – allowing to identify first dependencies as part of the second objective of this thesis.

Next, data regarding the resonance frequency of the wind turbine throughout the measurement campaign would be investigated, and its dependencies on parameters such as wind speed, blade pitch position, tilting of the OWT structure are of interest. Inclinometer together with strain readings could reveal permanent tilting of the OWT – possibly leading to a change in the resonance frequency of the structure.

Due to time limitation on the current project, modelling for validation and comparison of results from data analysis is left out of the scope. Modelling would be helpful for assuring that the dependencies that are unravelled with data analysis are not biased or incorrect due to false preprocessing of data, for instance. Hence, recommendations are to be provided to facilitate the verification or adoption of the herein presented analyses. What is more, soil data that is preprocessed and synchronized with other data sources in Sec. 2.2 is left out of the data analysis part in Chapter 3 due to time limitations and short duration of available readings.

Throughout this research, MATLAB 2020a software will be used for programming appropriate algorithms together with its in-built functions. Majority of used functions and tools are part of MATLAB's Signal Processing Toolbox [34].

## 1.4 Outline

In Chapter 1, an introduction to the motives of this work is provided. Additionally, the objectives of the research and the structure of the report are presented.

Chapter 2 is split into three sections. The first part provides an overview of the measurement data and its availability. In the second part, the centre of attention is on synchronization of datasets – the biggest part of data preprocessing. The last section of the chapter summarizes the performed data preprocessing and highlights some of the assumptions and possible sources of errors that were found and introduced.

Chapter 3 contains the data analysis and is separated into six sections. In Sec. 3.1 the monitored OWT's performance curves, such as rotor speed dependence on the wind speed, are given to understand the quality of the RNA data and the 'behaviour' of the OWT. Some data clustering is additionally done for improving the quality of work in the upcoming sections. Section 3.2 extends the RNA data analysis to finding dependencies between wind speed, resonance frequency and damping data. This is followed by inclinometer data analysis in Sec. 3.3 and evaluation of usability of strain gauge readings in Sec. 3.4. Fatigue analysis according to the defined scope is presented in Sec. 3.5, and lastly a summary of findings is presented in Sec. 3.6.

Chapter 4 extends the discussion of results to the conclusions of the whole project, with recommendations for possible future studies.

## Chapter 2

# Data Acquisition & Synchronisation

*This chapter presents an overview of the data that has been gathered from the wind turbine, located in the near-shore Westermeerwind farm in The Netherlands, situated at the East side of the IJsselmeer Lake. In addition to introducing the availability and the types of collected data in the first part, an applied method to correct for the identified synchronisation issues is described and supported by several case-studies in the second part of this section.*

### 2.1 Data Availability

The SWT 3.0-DD offshore monopile-supported wind turbine, referenced as W27 from now onwards, has been extensively monitored in the period 17/06/2015 – 26/07/2018 and is the subject of the current research project. The wind turbine is situated at the East side of the IJsselmeer lake in the Westermeerwind wind park (red circle in Fig. 1.3), and the gathered data has been subdivided into three categories:

- rotor-nacelle assembly (RNA) data, in Sec. 2.1.1;
- support structure (SUS) data, in Sec. 2.1.1;
- soil data, Sec. 2.1.1;

#### 2.1.1 RNA Data

RNA data originates from the supervisory control and data acquisition (SCADA) system, which is located at the RNA. The RNA data is collected approximately at the level of the axel of the W27 rotor at approximately 95 m NAP (see Fig. 2.1), and includes the following information:

- fore-aft (FA) and side-side (SS) accelerations;
- wind direction and speed, which is measured by an anemometer installed behind the rotor;
- blade pitch angle;
- power generation level;
- nacelle/yaw position;
- rotor speed;

- resonance frequency;
- FA and SS logarithmic decrement estimates.

From the accuracy or level of error standpoint the resonance frequency and damping values are estimates from curve fitting. The reported level of error of the resonance frequency values is  $\pm 0.0002$  Hz, excluding noise-related error. Additionally, it is known that because the anemometer is located behind the rotor, there is uncertainty in the measured values. However, all reported RNA data is deemed accurate enough for the current work.

RNA data contains a separate, non-uniformly spaced, time vector for each measurement channel. Non-uniformity stems from the used event-driven SCADA system. As a result, for instance, the available time channels for the accelerations indicate a sampling frequency range between 100 Hz to less than 1 Hz, with an average around 20 Hz. Continuous time-series in the RNA dataset are utilized only during preprocessing of the data in Sec. 2.2, and 10-min statistics of the continuous readings are used elsewhere due to the limited computational memory and work capacity.

The 10-minute statistical RNA data is based on 10-min data records of each monitored parameter. From each 10-min record, over the measurement period, statistical parameters - mean, minimum value, maximum value, and standard deviation - have been collected automatically by the RNA DAQ system. Furthermore, because storing statistics of 10-min data records requires much less memory than storing all 10-min continuous data records, 10-min statistical values are always available, whereas the raw continuous data can be accessed on demand for limited periods in the data history. Hence, the RNA 10-min statistics is a preferred choice for data analysis, if there is no direct requirement for the other.

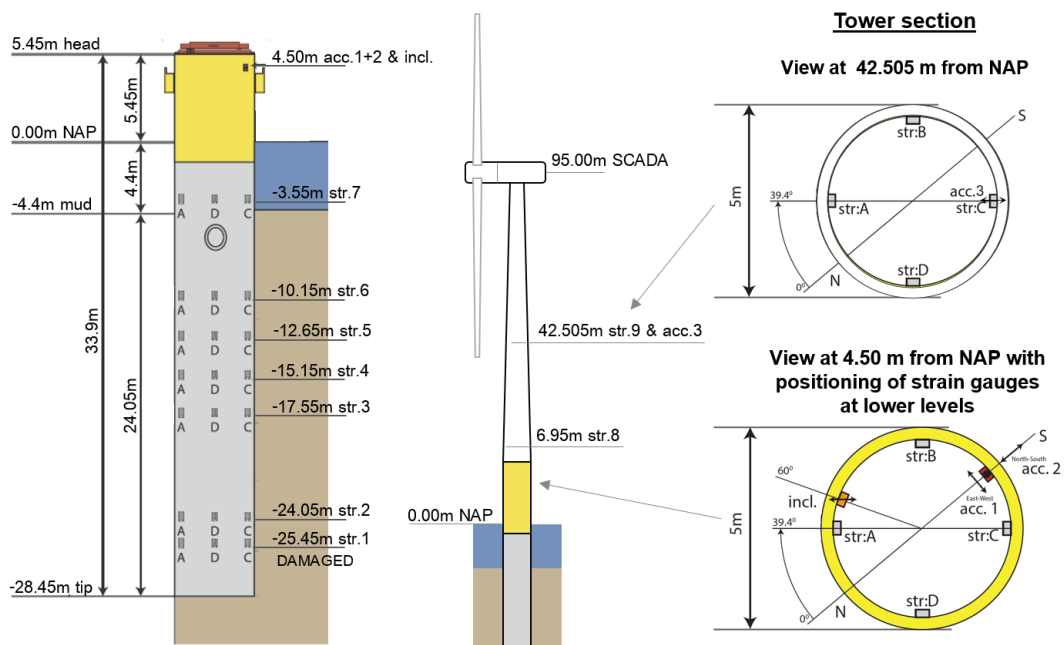


**Figure 2.1:** Positioning of RNA and support structure data sensors: strain gauges, accelerometers and an inclinometer.

Figure adopted from: [47]

### 2.1.2 Support Structure Data

The support structure (SUS) data has been acquired with a system commissioned by HBM in March 2016. The installed measurement setup, which is depicted in Fig. 2.1, includes nine rings of strain gauges, three accelerometers and one inclinometer.

The nine strain gauge rings were distributed as such: two rings of strain gauges were attached to the tower; and seven rings of strain gauges were attached to the inner pile wall, with six rings below, and one ring just above mudline. The rings were vertically distributed, with a concentration near the point where most bending was expected to occur [47]. It can be noted that the strain gauge ring 1 has not been depicted in Fig. 2.1. The reason being that strain gauge ring 1 was damaged during the driving of the pile. Each gauge ring consisted of four resistive strain gauges – one for each quadrant -, which are labelled as A-B-C-D. Similarly to gauge ring 1, gauges in rings 3, 4, 5, and 6 at D position and gauge B in ring 3 stopped working - likely also due to endured damage during the driving of the pile.

From here onwards, individual strain gauges will be referred to with a number-letter combination. The number indicates the gauge ring where the strain gauge is located, and the letter indicates the positioning of that individual strain gauge in the ring. For example, strain gauge 5C refers to the strain gauge at position C in ring 5 (-12.65 m NAP).

The unidirectional inclinometer, which measures only along the  $39.4^\circ$  -  $219.4^\circ$  line, is located at the same level as two of the three accelerometers: acc. 1 and acc. 2. The two accelerometers measure in N-S and W-E directions respectively. The third accelerometer was positioned on the same level with the strain gauge ring 9. The third accelerometer, acc. 3, measures accelerations only along the  $39.4^\circ$  -  $219.4^\circ$  line.

All devices recorded with a sampling frequency around 50 Hz and all SUS data was preprocessed with Bessel 2<sup>nd</sup> order low-pass filter with a cut-off frequency of 5 Hz. This filter was applied to avoid A/D converter receiving any frequency, which lies above half the sampling rate.

The level of error of the inclinometer and strain gauges were tested to be around  $\pm 1-2\%$  of the indicated values. For accelerometers, the reported error level was  $\pm 0.02 \text{ m/s}^2$ . In the reported error levels, the effects of incorrect attachment and misalignment of the sensors are not taken account of.

### 2.1.3 Soil Data

Soil investigations were performed by Fugro in 2012. Investigative tests and actions included CPTs and the retrieval of borehole samples, slug tests, and Seismic Cone Penetration Tests (SCPT) in order to characterize the small strain behaviour of the soils. The resulting soil parameter profiles from geotechnical and geophysical characterization can be found in [47]. In general, the site is characterized by saturated and stiff sandy soil conditions – similar to sandy North Sea sites.[47]

To monitor the soil-structure interaction during the operations of W27, eleven cones with accelerometers and piezometers for pore pressure readings were placed at various depths and radial distances from the pile. The positioning of the soil sensors in the top view can be observed from the illustrative sketch in Fig. 2.2, and the associated data table in the figure. The cones measure accelerations in two directions: vertical (Acc-Z) and radial (Acc-X), the radial direction refers towards the center of the monopile. It is to be noted that it is unknown if accelerometers, which were intended to capture the radial acceleration, remained oriented towards the center of the pile after the installation. However, with the help of dual-slope sensors in the probes the

actual depth of the sensors in the soil was confirmed.

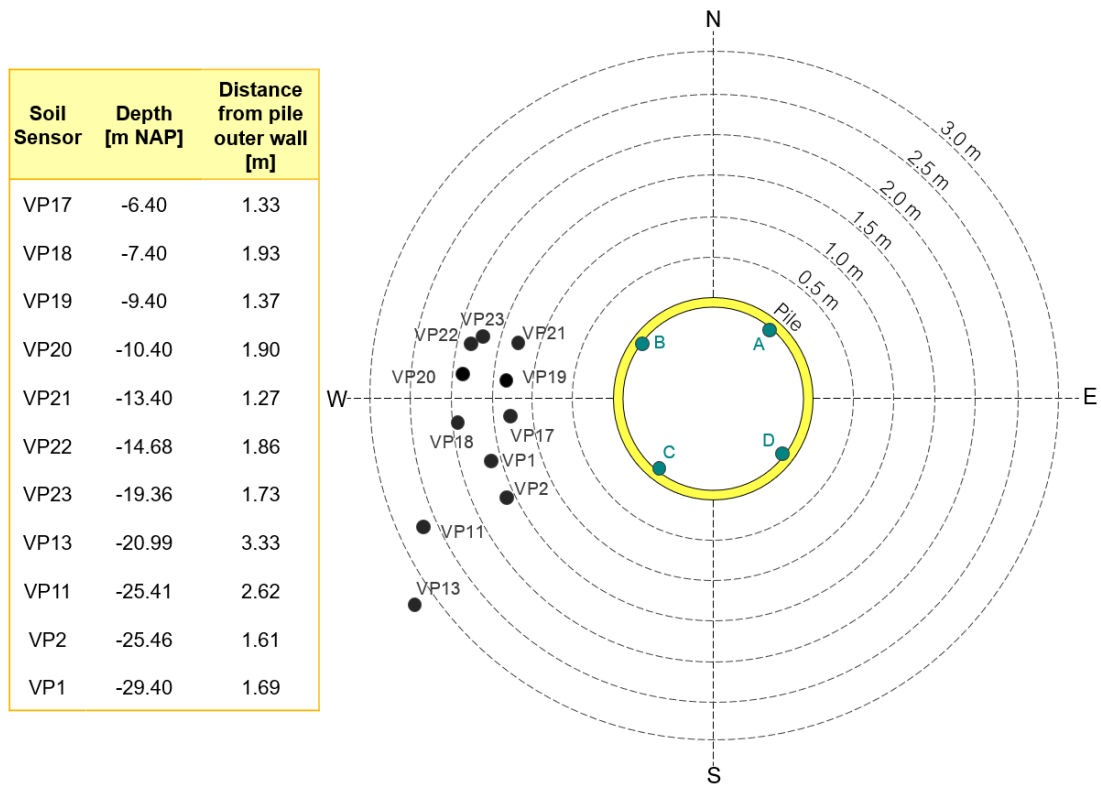


Figure 2.2: Positioning of soil sensors with respect to W27 and with respect to the OWT and the orientation of strain gauges in monopile foundation.

Table 2.1: Data availability timeline

Part 1	17-18/06/2015	24-26/06/2015	02-04/06/2015	1/1/2016	4/3/2016	27/11/2016
Soil data	█	█	█			
Support structure data	█	█	█		█	█
RNA data				█	█	█
RNA data 10-min statistics				█	█	█

(1)

Part 2	22/12/2016	18/07/2017	16/8/2017	28/8/2017	6/10/2017
Soil data			█	█	
Support structure data	█	█	█	█	█
RNA data			█	█	
RNA data 10-min statistics	█	█	█	█	█

(2) (3)

Part 3	7/10/2017	21/4/2018	6/7/2018	26/7/2018	1/3/2020
Soil data					
Support structure data	█	█	█	█	
RNA data					
RNA data 10-min statistics	█	█	█	█	█



### 2.1.4 Data Availability Timeline

For the purpose of understanding the fatigue behaviour of W27 and soil-structure interaction, it is important to have data from each one of the data sources available at the same point in time. A general availability overview of collected time signals between the period 17/06/2015 – 01/03/2020 is provided in Table 2.1, where the availability of each data set is indicated with coloured shading.

To provide more detail, the measurements between 17/06 – 04/07/2015 were done as part of the DISSTINCT project shaker tests, where SUS and soil sensors were located differently, and the tower was not installed yet. In the table, the RNA data refers to the continuous time signal. It can be observed that there are no complete overlaps between all datasets. There are, however, three periods where three out of four are available: (1) 04/03 – 27/11/2016; (2) 22/12/2016 – 18/07/2017; and (3) 16/08 – 28/08/2017. It can be noted that the RNA data statistics is always available since the commissioning of the turbine at the start of year 2016. The total overlap between the mainly used datasets in Ch. 3 - RNA data statistics and SUS data - is two years and three days between the period 04/03/2016 – 26/07/2018.

## 2.2 Synchronisation of Datasets

It is desired to have all datasets synced in time with the same sampling rate frequency. In this manner, information can conveniently be extracted from each data set from the same point in time - making it possible to combine data from different sources. In order to achieve that, the time signals had to be first re-sampled on a common time vector with a fixed sampling rate. It was decided to resample all signals with a sampling frequency of 50 Hz. The decision was motivated by the following considerations:

- Sampling frequency of RNA data goes up to 100 Hz; SUS data sampling frequency is approximately 50 Hz and soil data is sampled at 1000 Hz, which is too high and takes up a lot of memory space.
- Expected highest frequency content of interest from any of the datasets is around 10 Hz, and to ensure sufficient frequency resolution, 50 Hz is appropriate.

Linear interpolation was used as a way of resampling - it is illustrated in Fig. 2.3, where purple and green data points are the original and re-sampled signal respectively.

Having the time vectors with the same sampling frequency, a devised synchronisation procedure could be performed. Synchronisation is required as data sources utilized a different DAQ system and the exact time-zone settings were not reported for the SUS and soil data. It is known that RNA data time series corresponds to GMT+1 settings. Based on a previous study [16] on the synchronisation between the SUS and RNA data, it was found that the SUS data time series likely corresponds to GMT+0 time zone settings, but there is an additional unknown source of discrepancy besides the time zone settings. It is also found in Sec. 2.2.2.

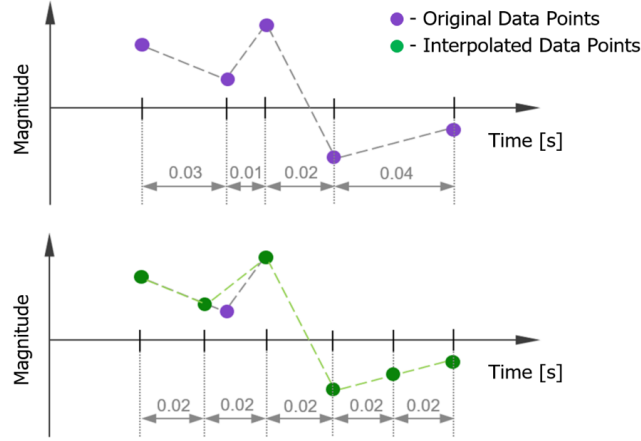


Figure 2.3: Example of resampling with linear interpolation.

### 2.2.1 Methodology

The aim of the synchronization is to find the lag between the SUS, RNA and soil data sets, which are all recorded on different DAQs. For this purpose, an approach based on computing cross-correlation sequence (CCS) between different sources of data was selected. It is a widely utilized mathematical tool in multi-sensor signal processing [51]. CCS, also called the time-ambiguity function ( $\check{R}_{xy}$ ), was defined in accordance with MATLAB's Signal Processing Toolbox guidelines [35] in the following way:

$$\check{R}_{xy}(p) = \begin{cases} \sum_{n=0}^{N-p-1} x_{n+p}y_n^* & p \geq 0 \\ \check{R}_{xy}^*(p) & p < 0 \end{cases}$$

where  $x_n$  and  $y_n$  are stationary random processes (e.g. collected acceleration, strain signals) of length  $N$  samples; the asterisk denotes the complex conjugate; and  $p$  ranges from  $-(N-1)$  to  $N-1$ .

The overall synchronisation approach consisted of several steps which had to be carried out before arriving at a CCS between different measurements. Aligning each of the datasets with the other had particularities, but the general procedure is described below:

1. Select a time period of interest and signals which are expected to have a correlation.

*For example, acceleration signals are likely correlated and similarly strain readings with acceleration measurements.*

2. Collect 10-minute statistics of chosen signals (e.g. standard deviation), and via investigation of abrupt changes in maximum, minimum or standard deviation values, a first estimate for the lag can be derived.
3. Select a segment of the continuous readings (e.g. a 2-hour segment) from one of the datasets, and another segment from the other dataset.

*Most importantly, the chosen data segments have to have some actual overlap, otherwise no correlation can be found. Thus, for determining the length of the data segments, it would be important to*

take into consideration the knowledge from statistics comparison, uncertainties related to day light saving time settings, time zone settings and other sources of differentiation.

4. Transform both data sets into a common or similar coordinate system, such as tower fixed or nacelle fixed coordinate system, to improve the performance of the approach.
5. Explore the frequency content of the chosen signals. In case of common high energy frequency bands, application of corresponding zero-phase band-pass filtering.
6. Scale the signals to a common magnitude range, as original signals may have different magnitudes. Signal shape and trend is more important for lag identification with CCS.
7. Compute the cross-correlation sequence (CCS) between the selected processed (e.g filtered, scaled) measurement signals, two signals can be correlated at a time.
8. Identify the time delay value, which theoretically corresponds to the value associated with the peak value in the CCS.
9. Make appropriate lag corrections to one of the signals and check if time-corrected signal aligns with the other.

If results are found to be satisfactory - meaning that the signals could visually be seen to be aligned appropriately -, automation and additional data segments can be reapplied to steps 4 - 8 in the established routine. This allows to verify the found lag values, before applying an appropriate correction - as step nine - to the datasets. The latter is done only if it is found necessary.

When scaling data to a common magnitude range, ranges 0 to 1 and -1 to 1 were used. Min-max scaling approach was chosen and the corresponding formula for scaling the data to either of the ranges throughout this thesis was the following:

$$s' = a + \frac{(s - \min(s))(b - a)}{\max(s) - \min(s)} \quad (2.1)$$

, where  $a$  and  $b$  are the destination range min-max values (e.g. [0, 1] or [-1, 1];  $s$  is the original signal;  $s'$  is the scaled signal of  $s$ ;  $\min(s)$  refers to the minimum value in the signal  $s$ ; and  $\max(s)$  refers to the maximum value of signal  $s$ .

Having the general lag identification and data synchronisation approach laid out, the following Secs. 2.2.2, 2.2.3 and 2.2.4 introduce how it was used on the gathered data.

### 2.2.2 Synchronisation of RNA Data and Support Structure Data

For the synchronization of continuous RNA data and SUS data, three short "study periods" (s.p) from the total overlap of approximately 1.3 years (4/3/2016 - 27/11/2016; 22/12/2016 - 18/7/2017) were studied: 10-17/3/2016; 6-9/1/2017; and 2-6/7/2017. In the same order, these study periods are referred to as "March 2016", "January 2017" and "July 2017". The synchronization procedure is herein provided more elaborately for the 4-day "July 2017" study period, but the chosen parameters and final results will be shown for all study periods.

As per the methodology introduced in the previous section, having chosen the study periods, the 10-minute statistics of acceleration signals from both data sources was studied. From Fig. 2.4, it was found from the comparison of the standard deviation of SUS acc. 3 readings and RNA FA

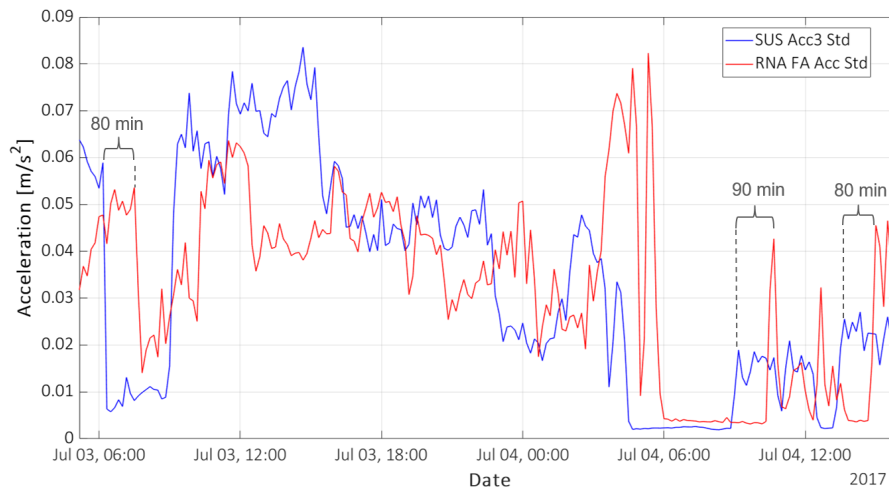


**Figure 2.4:** "July 2017" study period 10-minute statistics comparison - standard deviation of SUS acc. 3 readings and RNA FA acceleration.

motion accelerations that the estimated time delay between the two signals is around 80-90 minutes in the "July 2017" study period measurements. This estimate was based on identifying visually the abrupt changes in the 10-minute statistical parameter. The respective estimates for the "March 2016" and "January 2017" study periods were 60-70 minutes and 70-80 minutes. This increasing trend referred to the possibility that the SUS data time signal is falling behind and, hence, there is likely a time-dependent lag.

In addition, SUS acc. 3 readings were chosen instead of acc. 1 or 2, because it was located closest to the RNA accelerometer. Hence it should provide a recording that is closer to the one from the RNA sensor – regarding the 1<sup>st</sup> mode tower response reading. It must be noted that the acc. 3 has a fixed measurement direction, but the RNA accelerometer moves together with the assembly. Regardless, sudden changes in the OWT structure are still visible in the unidirectional sensors as the response of the system is global.

Having found an estimate, the continuous data sets were studied next. The first thing was to pick the duration of the data segments, which are to be cross-correlated. Trial-and-error was required for optimal performance, because more accurate results can be obtained with longer segments, but at the same time computational effort increases. However, the effect of the first - accuracy - is reduced with time-dependent lag. From trials with the time signal, it was found that using 2-hour data segments provides satisfactory results, which are shown later. Hence it was decided to go over the whole period 2-6/7/2017 in 10-minute steps, resulting a total of 575 iterations. An example of data segment lengths in each iteration is illustrated below for the "July 2017" study period:

1<sup>st</sup> iteration:

- RNA FA acc. segment: 02/07/2017 17:00:00 - 19:00:00
- SUS acc. 3 segment: 02/07/2017 18:00:00 - 20:00:00

2<sup>nd</sup> iteration:

- RNA FA acc. segment: 02/07/2017 17:10:00 - 19:10:00
- SUS acc. 3 segment: 02/07/2017 18:10:00 - 20:10:00

⋮

575<sup>th</sup> iteration:

- RNA FA acc. segment: 06/07/2017 16:40:00 - 18:40:00
- SUS acc. 3 segment: 06/07/2017 17:40:00 - 19:40:00

It can be noticed that the previous knowledge about lag from statistics has been considered, to a certain extent. It was seen in Fig. 2.4 that the SUS recordings are approximately 80-90 minutes ahead of RNA recordings, so the start of the SUS data segments was set 60 minutes later in the RNA segment, similarly was done to the end point. For optimizing efficiency a delay of around 80 or 90 minutes should have been chosen instead of the used 60 minutes.

The next step in the process is to transform both accelerometer data sets into a common coordinate system. One way would be to transfer the SUS's acc. 1 and 2 readings into the RNA data coordinate (FA and SS) system. However, this transformation would require an accurate knowledge of the lag between the two data sets, as the info about the yaw position from RNA data is used to alter the SUS acceleration readings via trigonometry. It would be a possibility if the nacelle/yaw positioning is constant for a long period of time, but - as can be examined in Fig. 2.5 – this is not the case for the "July 2017" period. Hence, an alternative transformation was chosen: the RNA FA and SS accelerations were converted to SUS acc. 3 measurement directions.

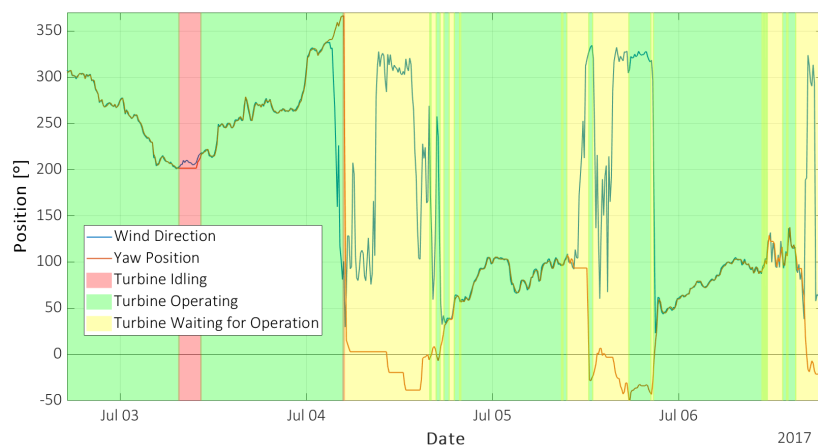


**Figure 2.5:** RNA 10-minute average - wind direction, yaw positioning, and operational status of W27 for the period 02/07/2017 17:00:00 - 06/07/2017 18:40:00.

Following the conversion of the RNA signal to a fixed coordinate system, the frequency domain of the resulting signal is studied with the aim of finding common high energy frequency bands – it improves the performance of the cross-correlation sequence for lag identification. The reason is that in case of strong excitation the signal to noise ratio increases and resultantly the correlation between studied signals increases. Examples of SUS acc. 3 and transformed RNA acceleration readings with respective signal S-transforms (a type of STFT [24]) can be found in Figs. 2.6 and 2.7.

From a general farm-wide W27-type OWT design model, it is known that the first three SUS FA and SS bending modes, according to the lowest frequency design position, are expected from frequency ranges 0.275 - 0.278 Hz, 1.508 - 1.525 Hz, and 2.752 - 3.128 Hz respectively. The corresponding mode shapes (same for FA and SS) are shown in Fig. 2.8. The lowest design frequency position of the Westermeerwind wind farm implies that the OWT is located in soft soil conditions at the deepest water position of the wind farm. However, in Sec. 3.2 it is found from

RNA data analysis that W27 resonance frequency is higher than the lowest frequency design position estimate of 0.275 - 0.278 Hz. Thus, high energy frequency bands - associated with bending modes - in signals are expected to be located at frequency ranges that are higher than the aforementioned lowest frequency design position estimates.

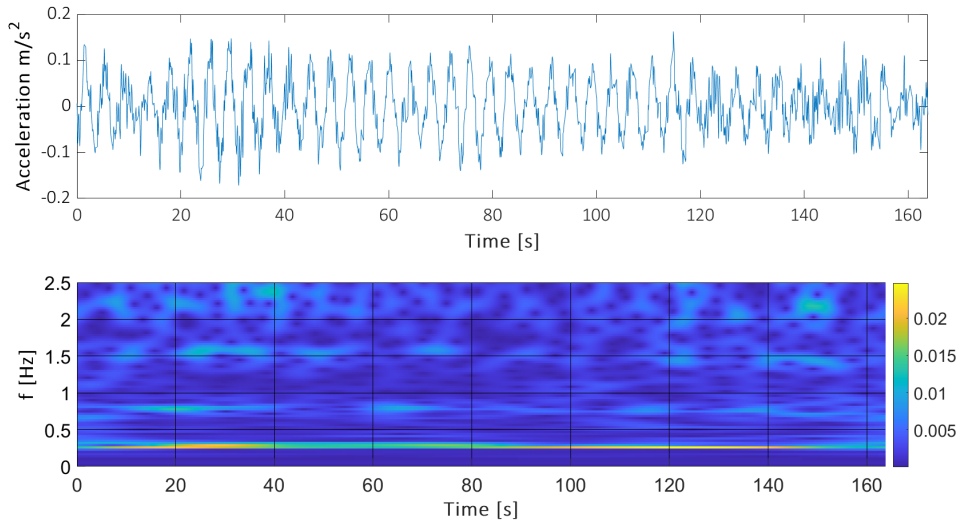


**Figure 2.6:** 10-minute snippet of RNA acceleration recording transformed to acc. 3 orientation, with the S-transform of the corresponding signal, from the "July 2017" study period.

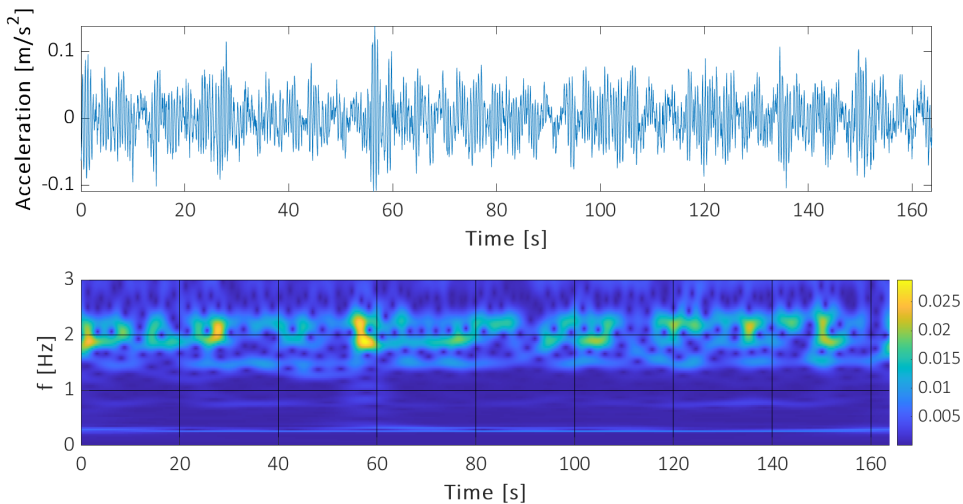


**Figure 2.7:** 10-minute snippet of SUS acc. 3 recording, with the S-transform of the corresponding signal, from the "July 2017" study period.

Observation of Figs. 2.6 and 2.7 confirms the expected. Both acceleration signals illustrate higher energy content at the first eigenfrequency that is around 0.3 Hz. It is anticipated, because the 1<sup>st</sup> SUS modes of vibration are characterised by having the largest amplitude at the top of the tower. The 1<sup>st</sup> mode amplitude reduces down the SUS, and the lowest amplitude of motion is near the bottom of the SUS (Fig. 2.8). As a reminder, the two currently studied signals originate from the top and approximately mid-point of the tower. Acc. 3 recording has,

additionally, noticeable frequency content around 2 Hz - related to 2<sup>nd</sup> FA and SS SUS bending modes. Stronger presence of the 2<sup>nd</sup> mode frequency band, in comparison to the 1<sup>st</sup> mode band, in SUS acc. 3 recording (Fig. 2.7) is related to its position. The accelerometer is located at a level, where large 2<sup>nd</sup> mode response is expected (Fig: 2.8). Following the same logic, RNA accelerometer is more susceptible to 1<sup>st</sup> mode action, as is visible in Fig. 2.6

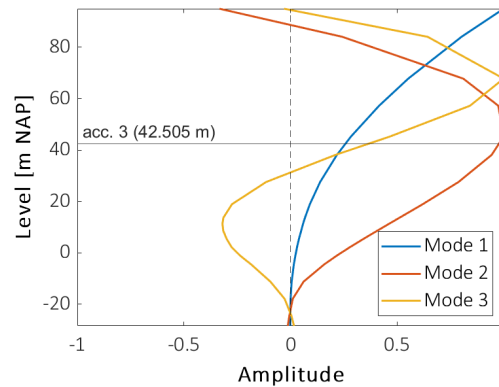


**Figure 2.8:** OWT lowest frequency design position model 1<sup>st</sup>, 2<sup>nd</sup> and 3<sup>rd</sup> mode shapes.

Having the frequency domain information of the acceleration signals, zero-phase filtering with a Chebyshev Type II bandpass filter [34] was applied. The required filter parameters were set as follows: (1) passband edges: 0.2 Hz, 0.6 Hz; (2) stopband edges: 0.1 Hz, 0.75 Hz; (3) passband ripple: 0.1 dB; (4) stopband attenuation: 100 dB. The transient effects of the filter were minimised by extending each of the signals by five times the order of the filter at the start and end of each measurement segment, for the duration of the filtering procedure.

The next steps in the process were the scaling of the signals to a common magnitude range of [-1, 1] and then setting up the discrete-time sequence pairings to calculate the CCS. CCS allows to identify the existing lag between the pairings. For example, in the lag identification between RNA and SUS data, the pairing of SUS acc. 3 and RNA Acc3-oriented signal readings was used. Acc3 refers to acceleration readings along acc. 3 measurement directions ( $39.4^\circ - 219.4^\circ$ ). After determining the CCS and considering the location of maximum value of CCS to indicate the lag between signals, the signals can be aligned and visually inspected for verification.

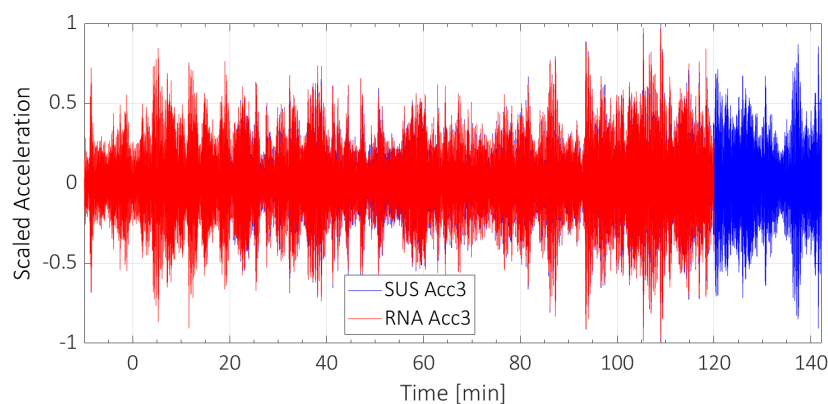


**Figure 2.9:** Scaled, bandpass filtered and lag-corrected support structure and RNA Acc3-oriented acceleration signals overlain.

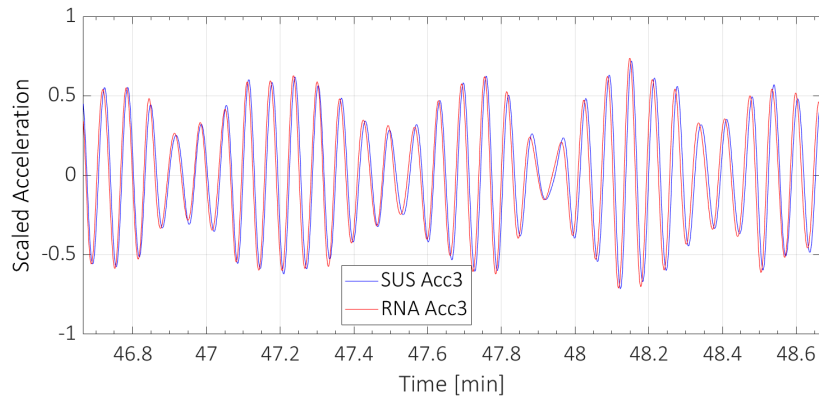


**Figure 2.10:** Zoomed in from Fig. 2.9: scaled, bandpass filtered and lag-corrected support structure and RNA Acc3-oriented acceleration signals overlain

An example of aligned signals from the results of the aforementioned 1<sup>st</sup> iteration in the "July 2017" study period are shown in Figs. 2.9 and 2.10. The lag was found to be approximately 82.25 minutes – the initially introduced 60 min delay plus an additional 22.25 min, which can be observed in Fig. 2.9.

Affirmation on the usage of the chosen approach for synchronising signals from different DAQ systems allowed to automate the process and derive the trend lines of the collected lag values between the two signals. In Fig. 2.11, the identified lag from all of the iterations was plotted with respect to the respective start time of the RNA acceleration data subset. The outliers (5 out of 575) in Fig. 2.11 did not fit into the frame of the trendline – these corresponded to periods with low wind speeds or standstill conditions where signal to noise ratio is low. It was revealed that the lag is linearly increasing within the chosen study period (2-6/7/2017), similarly to "March 2016" and "Jan 2017" period results. In Fig. 2.11, the value of the fitted linear line gradient represents the lag increase rate, for the "July 2017" period.

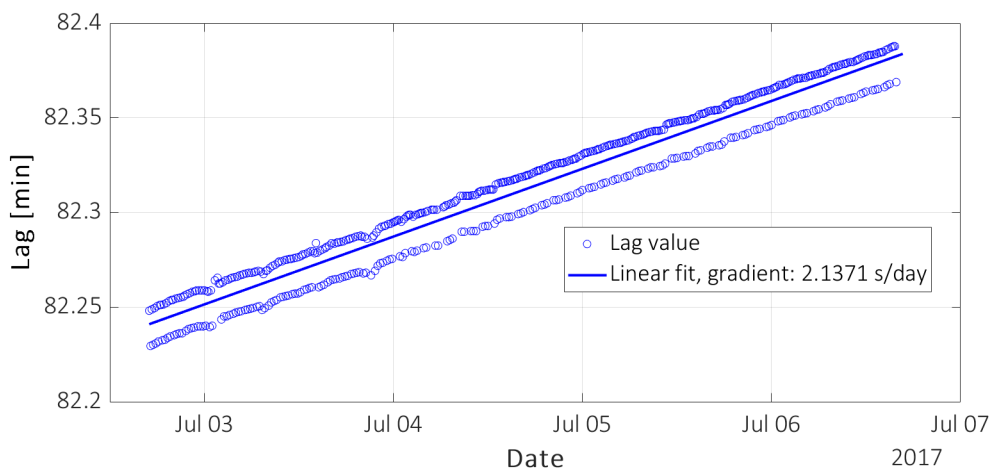


**Figure 2.11:** July period lag identification study results from the filtered and scaled Acc3-oriented signal pairing.

What is more, it can be observed that there is scatter in the results in Fig. 2.11, as the fitted linear line lies between identified lag value data points. This scatter is thought to be caused by



slight variations in the correlated signals and resulting numerical deviation in the CCS. Variations can be considered to be different noise levels, in-phase or out-of-phase signal starting and ending points between the two correlated signals. Additional deviations may come from having too long data segments in each iteration, because the lag is examined to be increasing in time.

The results from the lag estimation routines on the three study periods are summarized in Table 2.2. Comparison of the the lag increase rates in the table indicates that the lag increase rate is not constant among the study periods but increases in time. Thus, the change in lag is not completely linear, like was estimated in Fig. 2.11. In the table, in addition to the lag rates, the lag value from the mid-point of a study period, from the linearly fitted lines, is provided. These mid-period lag values were used to check the lag rate values in-between the three study periods in Table 2.3, and are eventually used as reference points in the lag correction process.

**Table 2.2:** Results from the application of the cross-correlation based lag identification procedure on the considered study periods.

Period	Lag increase rate [s/day]	Mid-period lag value [min]
Mar 2016 s.p.	1.9138	66.270
Jan 2017 s.p.	2.1141	76.165
Jul 2017 s.p.	2.1371	82.314

If theses mid-(study)period lag values in Table 2.2, would be connected by straight lines over the respective time span, the lag increase rates would differ from the ones in Table 2.2. The resulting lag increase rates are shown in Table 2.3. In Table 2.3 the three cases that could be considered are presented. For example, by taking the "March 2016" period mid-point (13/3/2016 5:30:00) value of 66.27 minutes and connecting it to "January 2017" period mid-point (8/1/2017 1:50:00) value of 76.165 minutes, a lag increase rate of 1.9804 s/day results.

**Table 2.3:** Lag increase rates in-between studied periods according to the found mid-period lag values.

Period	Lag increase rate [s/day]
Mar 2016 s.p. - Jan 2017 s.p.	1.9804
Mar 2016 s.p. - Jul 2017 s.p.	2.016
Jan 2017 s.p. - Jul 2017 s.p.	2.0736

Before a lag correction could be applied to either of the datasets, it had to be decided, which one of the readings is considered to be the 'correct' one. Consideration was given to the fact that the RNA data time series are used for high-level process supervisory management of wind farms - it inherently is tested to be accurate. At the same time, SUS DAQ system utilised a clock, which was installed for a shorter term purpose and was not tested for performance over a longer period of time. Additionally, it would not be possible to change the 10-min RNA data statistics to take account of the time-dependent lag. RNA data 10-min statistics forms an integral part of results that are presented in Ch. 3. Resultantly, SUS data time series was considered to be 'wrong' and RNA readings as 'correct'. The chosen 'correct' dataset is supported by results that are presented in Fig. 2.19 in Sec. 2.2.3.

Considering the derived time-dependent lag characteristics, it was decided to divide the whole two years (04/03/2016 – 26/07/2018) of SUS data into three "correction periods" (see

Table 2.4). The start and end points of the "correction periods" were chosen based on the locations of small data gaps in either of the datasets. In each "correction period", the data would be linearly stretched according to the values in Table 2.4 to best match RNA data. The first step in stretching involved adjusting every SUS data point,  $i$ , time value,  $T_i$  as follows

$$T_{i,new} = (T_i + C_{ref}) + (T_i - T_{ref}) \cdot (R_{cor}) \quad (2.2)$$

, where  $T_{i,new}$  is the new and corrected datetime stamp of a SUS data point;  $T_i$  is the original and 'wrong' datetime stamp of a SUS data point;  $T_{ref}$  is one of the mid-(study)period datetime points, acting as a reference datetime point;  $C_{ref}$  is the corresponding mid-(study)period constant lag value; and  $R_{cor}$  is the chosen lag correction rate.

The chosen parameters and "correction periods" are provided in Table 2.4. The chosen  $T_{ref}$  datetimes corresponded to the mid-points of the three study periods ("March 2016", "January 2017", "July 2017"). The corresponding correction values ( $C_{ref}$ ) originate from Table 2.2. The first two correction rates ( $R_{cor}$ ) were decided to be approximated from Table 2.3, and the third was guessed based on the previous values.

**Table 2.4:** Chosen parameters for lag correction of the support structure data.

Correction period	Reference datetime, $T_{ref}$	Correction rate, $R_{cor}$ [s/day]	Constant correction value, $C_{ref}$ [min]
4/3/2016 - 27/11/2016	3/14/2016 5:30	1.98	66.270
22/12/2016 - 15/8/2017	8/1/2017 1:50	2.08	76.165
16/8/2017 - 26/7/2018	4/7/2017 17:50	2.10	82.314

Stretching of the original SUS datetime vector with Eq. 2.2 reduced the sampling rate of SUS data by a small amount. Thus, SUS data had to be resampled at 50 Hz again to be able to combine SUS data with RNA data during data analysis. For that purpose, nearest neighbour interpolation [33] was utilised because it preserved the original magnitudes of all data points, while allowing to remove the time-dependent lag.

After the application of the correction, the two data sets were checked to be synchronized by rerunning the synchronization routine. The result is provided in Fig. 2.12 for the "July 2017" study period – the linear trend can be considered gone and the fitted linear least square line is close to the zero-line. The latter proves that the lag is eliminated to an acceptable level (about  $5 \cdot 10^{-3}$  min). Additional single value adjustments could be made to bring the linear fitted line closer to the zero, but was deemed unnecessary because of the shortness of the study period in comparison to the overall data availability duration, and the unknown physical reason(s) for the discovered time-dependent lag.

The guessed lag increase rate of 2.08 for the period 7/7/2017 - 15/8/2017, and 2.1 s/day for the period 16/8/2017 - 26/7/2018 (Table 2.4) are likely the biggest sources of error in the chosen correction approach. The reason being that there is no data to check how the lag would continue to develop in these periods - the increasing trend may even have stopped. The latest checkable period was the studied "July 2017" period (2-6/7/2017). The only available option for checking if the correction was performed appropriately beyond the "July 2017" period, is to compare 10-minute statistical data again. For the purpose, the alignment of RNA and SUS 10-min acceleration standard deviation values between the period 25/7/2018 14:00 - 26/7/2018 15:10 was looked. In Fig. 2.13, the corresponding progression of RNA FA acceleration 10-min standard deviation was plotted together with lag-corrected SUS acc. 3 data 10-min standard

deviation values. From the comparison of the locations of peaks and troughs between the two lines in Fig. 2.13, it is clear that the 10-min statistics of both data sets has been synchronised and the lag continued to increase after the "July 2017" study period with an increasing rate for some period of time. The latter can be stated because the accumulated increase in lag, with a rate of 2.1 s/day, over the period 7/7/2017 - 26/7/2018 would be around 13.44 minutes. Thus, if the lag increase had stopped right after "July 2017" period, the SUS data statistics peaks and troughs in Fig. 2.13 would not have aligned with RNA data 10-min statistics. Instead, an offset of at least 10 minutes - one data point in the plot - would have been visible.

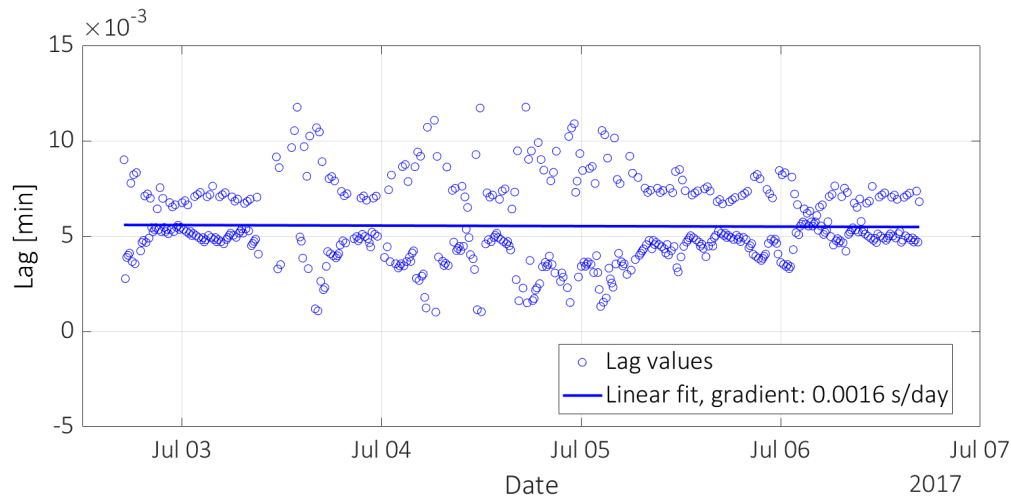


**Figure 2.12:** July period lag identification study results from the filtered and scaled Acc3-oriented signal pairing after lag correction.

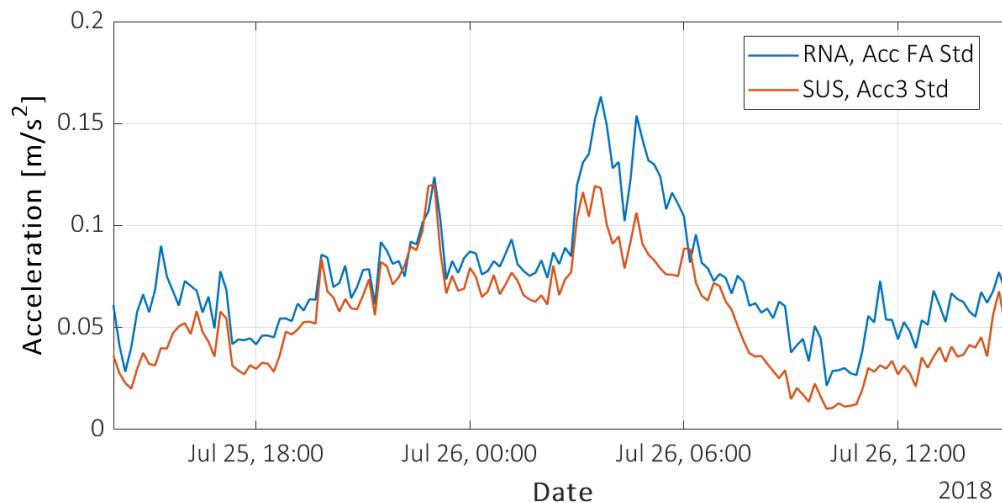


**Figure 2.13:** RNA FA acceleration 10-min standard deviation and lag-corrected SUS acc. 3 data 10-min standard deviation development over time.

What is more, with the stretching of SUS data, the signal frequency content was altered by a negligible amount. For example, in the current work, the highest relevant frequency content is 5 Hz (in Sec. 3.5.5), which implies an oscillation/wave period of 0.2 seconds. If the data is

stretched with a correction rate of 2.1 s/day, each of the data points would be moved further from the previous data point by approximately 486 nanoseconds, in case of 50 Hz sampling rate. Over a 0.2 second period, the first and last data points would be distanced by approximately 4.86 microseconds. Resultantly, the original 5 Hz frequency content in the signal would be decreased to a rounded level of 4.9999 Hz. In case of the lowest relevant frequency level of 0.02 Hz, the reduction is approximately 0.5  $\mu$ Hz with the chosen lag correction approach. The introduced change in the frequency content of the SUS recordings was deemed acceptable for current work, and so the synchronisation of RNA and SUS data was completed.

### 2.2.3 Synchronisation of Soil Data and Support Structure Data

The overlap between the soil and SUS data is approximately 11 days (16/08/2017 16:00 - 27/08/2017 14:20), as was indicated in Table 2.1. The main difficulty in the synchronization of soil and SUS data laid in finding the soil probes that provided a similar reading to acc. 1 and strain gauge recordings. Eventually it was discovered that soil sensors VP-19 (-9.4 NAP) and VP-20 (-10.4 NAP) X-directional (radial) accelerometers were suitable (see Fig. 2.2).

From the SUS data set, acc. 1 (4.5 m NAP) and strain readings from levels 4 (-15.15 m NAP), 5 (-12.65 m NAP), and 6 (-10.15 m NAP) were used (see Fig. 2.1). In the pairing of soil acceleration *versus* SUS strain readings, acceleration was double integrated to displacements – allowing to cross-correlate directly linked physical behaviors with the same phase angle. Acc. 1 (4.5 m NAP) readings were chosen because it was closer to the soil sensors than acc. 3 (42.505 m NAP). Furthermore, acc. 1 measurement direction - east-west - aligned better with the soil sensors radial acceleration (Acc-X) measurements than in the case with acc. 2, which measured along the north-south line. Strain gauge rings 4, 5 and 6 were picked due to their similar depth to soil probes VP-19 and VP-20, see Figs. 2.1 and 2.2.

Before the identification of lag between SUS and soil data, it was unknown if the lag would be linearly changing between the two like it was found to be between RNA and SUS data. Because of that, lag-corrected SUS data (Sec. 2.2.2) was not used in the process of SUS and soil data synchronisation. Instead, the original SUS data was shifted forward in time only by a single constant value of 84.01 minutes - no stretching was applied. This value was based on extrapolating the known lag value between the RNA and SUS data from the mid-point of the "July 2017" study period (04/07/2017 17:50:00) to the mid-point of the 11-day period in August (22/8/2017 03:10:00) with an increase rate of 2.1 s/day. By doing so, the SUS data would still be approximately synchronised with RNA data. Because SUS data was not stretched in this case, it would deviate from RNA data less than 13 seconds at the beginning and end of the August 11-day period. The previous holds if the lag increase rate between SUS and RNA data between the end of "July 2017" period and the 11-day "August 2017" period is 2.1 s/day. Thus, if the lag between SUS and soil data is identified and corrected, all datasets could approximately be considered synchronised.

Following the syncing methodology that was outlined in Sec. 2.2.1, the standard deviations of accelerations from SUS and soil data set were studied. A 60-minute delay in the soil data 10-min statistics with respect to the SUS data 10-min statistics was identified via Fig. 2.14. In the figure, standard deviation readings from each signal were scaled to a common range [0, 1]. It was done because soil accelerations had significantly lower values than SUS acceleration values as expected due to signal energy dissipation in the soil medium. Resultantly, it would not be possible to arrive at a lag estimate without scaling.

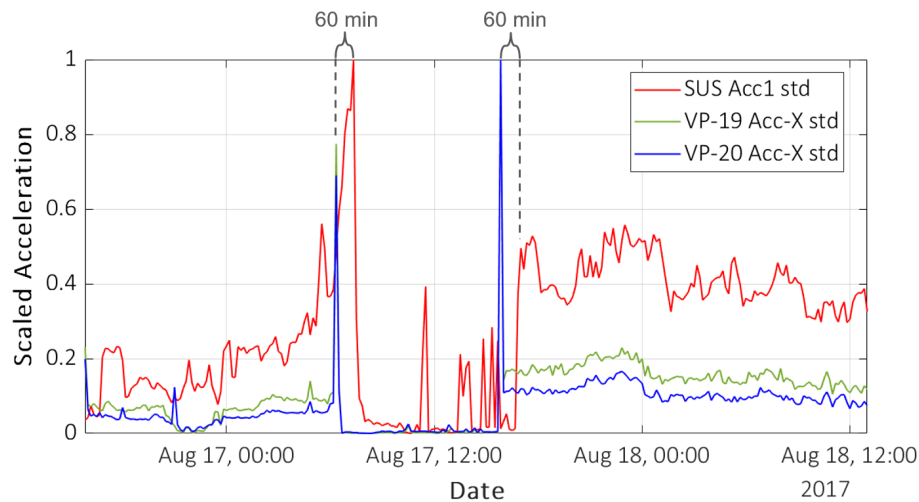


**Figure 2.14:** August period 10-minute statistics comparison - standard deviation of SUS Acc1, soil VP-19 Acc-X, and VP-20 Acc-X accelerations.

The estimate of 60 minute delay between the two data sets was taken into consideration for the next step of the synchronization procedure. It was decided to take 2-hour continuous data segments such that the start of the soil data recording would be taken an hour ahead of the SUS data segment in the common time vector. Because of small data gaps in the soil and SUS data near the start and end of the 11-day “August 2017” study period, the number of cross-correlation iterations was limited to 1000. The step size in time – as previously in Sec. 2.2.2 – was set to 10 minutes. An example of data segment lengths in each iteration is illustrated below for the “August 2017” period:

1<sup>st</sup> iteration:

- Soil (Acc-X or disp.-X) data segment: 17/08/2017 9:00:00 - 11:00:00
- SUS (Acc1 or strain) data segment: 17/08/2017 10:00:00 - 12:00:00

2<sup>nd</sup> iteration:

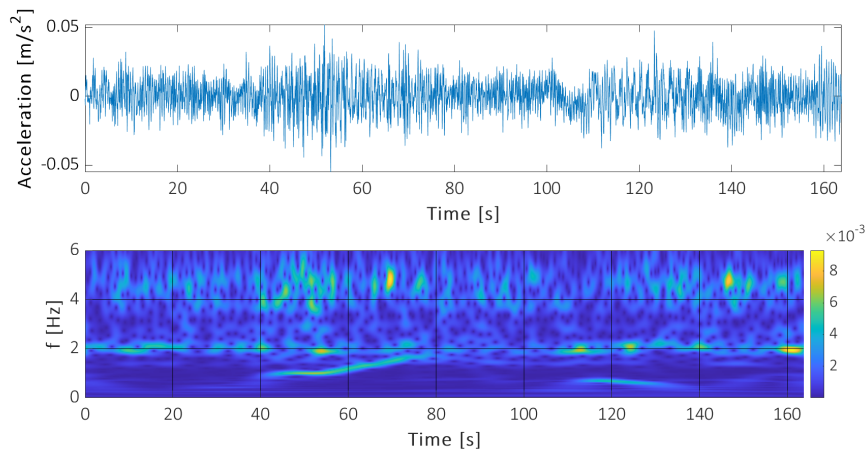
- Soil (Acc-X or disp.-X) data segment: 17/08/2017 9:10:00 - 11:10:00
- SUS (Acc1 or strain) data segment: 17/08/2017 10:10:00 - 12:10:00

⋮

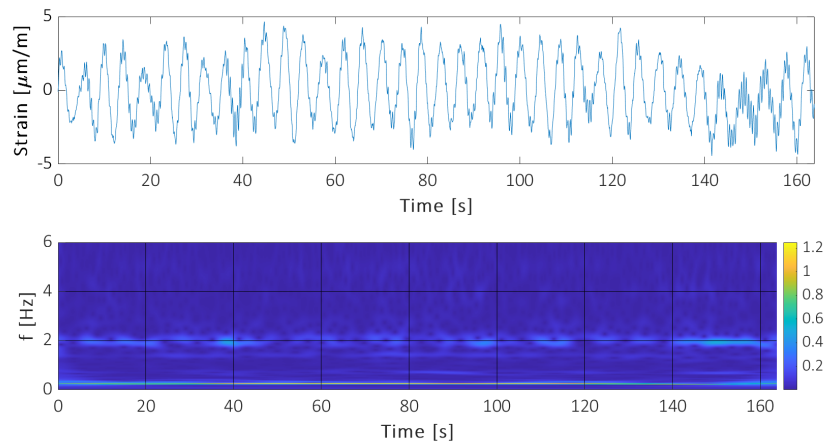
1000<sup>th</sup> iteration:

- Soil (Acc-X or disp.-X) data segment: 24/08/2017 7:30:00 - 9:30:00
- SUS (Acc1 or strain) data segment: 24/08/2017 8:30:00 - 10:30:00

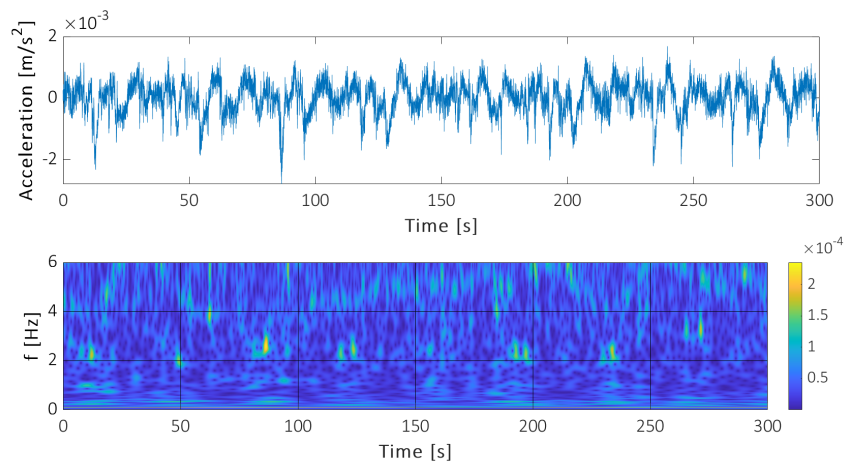
The S-transforms of signals were found to identify usable common high-energy frequency bands. Figs. 2.15a, 2.15b, and 2.15c revealed that the soil acceleration, SUS acc. 1 and gauge 5C strain readings have a common band at around 2 Hz. Figs. 2.15a and 2.15c additionally show content in the 4 – 5 Hz range. The band around 2 Hz would correspond to 2<sup>nd</sup> SUS bending modes, which were also discussed in 2.2.2. Correspondingly, the 2 Hz band in S-transforms of the soil acceleration readings (Fig. 2.15c) would come from the excitation of the SUS response to the soil. The 4 - 5 Hz range could be caused by the interplay of three effects: (1) it is a multiple of the 2 Hz band; (2) high (3<sup>rd</sup> and 4<sup>th</sup>) SUS bending modes are excited, and (3) in one of the DISSTINCT related studies [47] it was proposed that the 2<sup>nd</sup> soil mode is located at 5.42 Hz.



(a) Acc. 1 recording



(b) Strain gauge 5C recording



(c) VP-19 Acc-X recording

**Figure 2.15:** 10-minute snippets of SUS and soil recordings, with the S-transform of the corresponding signal, from the "August 2017" study period.

Marginal signs of 1<sup>st</sup> SUS bending mode frequency content at around 0.3 Hz in the signals in Figs. 2.15a, 2.15b, and 2.15c can be explained by visualising the mode shapes together with the positioning of sensors. In comparison to 1<sup>st</sup> SUS bending mode, the amplitude of the 2<sup>nd</sup> and 3<sup>rd</sup> modes is considerably higher at levels of the three sensors - acc1, strain gauge 5C, and VP-19. It must not be forgotten though, energy (e.g. wind, wave, 1P loading) which would excite the modes has to be first inserted into the structural system for any mode shape to form in reality. The closer the frequency of the input energy is to the OWT SUS mode frequencies, the stronger its presence in the measured response signals (Figs. 2.15a, 2.15b, and 2.15c).

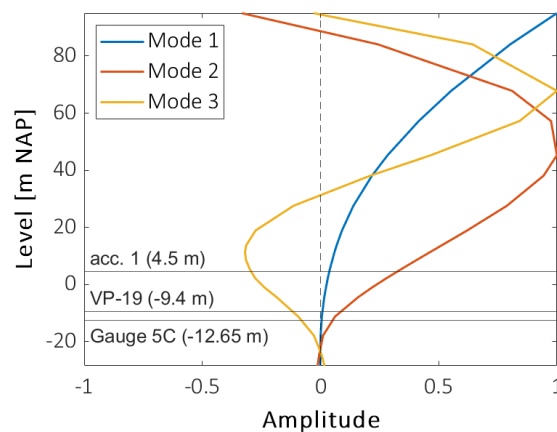


**Figure 2.16:** OWT lowest frequency design position model 1<sup>st</sup>, 2<sup>nd</sup> and 3<sup>rd</sup> mode shapes.

Because a common higher energy frequency band around 2 Hz was identified in all readings (Figs. 2.15a, 2.15b, and 2.15c), the data was zero-phase bandpass filtered with the following Chebyshev Type II filter [34]: (1) passband edges: 1.2 Hz, 2.3 Hz; (2) stopband edges: 1.0 Hz, 2.5 Hz; (3) passband ripple: 0.1 dB; (4) stopband attenuation: 100 dB. The filtering was applied to improve the accuracy and performance of lag identification.

The next step in the process was scaling each of the signals to a common scale [1,-1]. Then, discrete-time sequence pairings could be set up to calculate the CCS for identifying the existing lag between the pairings. A total of 20 data pairings were employed for the lag identification, and 16 of them provided consistent results. These 20 pairings included: SUS acc. 1 *versus* VP-19 & VP-20 Acc-X; and SUS strains from gauges A, B, C at levels 4, 5, 6 *versus* VP-19 & VP-20 X-directional displacement readings. A complete overview of pairings can be found in Table 2.5.

After determining the CCSs, the signals (in each pairing) could be aligned according to the identified lag value and visually inspected for verification. An example of aligned signals (Acc1 and VP-19 Acc-X) from the results of the 112<sup>th</sup> iteration in the "August 2017" study period are shown in Figs. 2.17 and 2.18. Unlike in Figs. 2.9 and 2.10 in Sec. 2.2.2, the two aligned recordings in Figs. 2.17 and 2.18 show less likeness. The amplitudes of the scaled signals - at approximately same points in time - vary and recordings can be seen to be out-of-phase at points. The alignment of trends of amplitude increase and decrease in the scaled acceleration signals can be observed - see readings between minutes 42.3 and 42.52 in Fig. 2.18. However, the changes in trends are not aligning consistently. It is clear that the stiff soil medium has distorted the monopile foundation response signal. Thus, the correctness of identified lag could not be visually confirmed. However, the lag was found to be approximately 59.51 minutes in that iteration - corresponding well with the expected lag of 60 minutes, which was based on the

observation of 10-min statistics (see Fig. 2.14). Hence, the devised method of synchronization (in Sec. 2.2.1) was still considered acceptable for the synchronization of SUS and soil data.

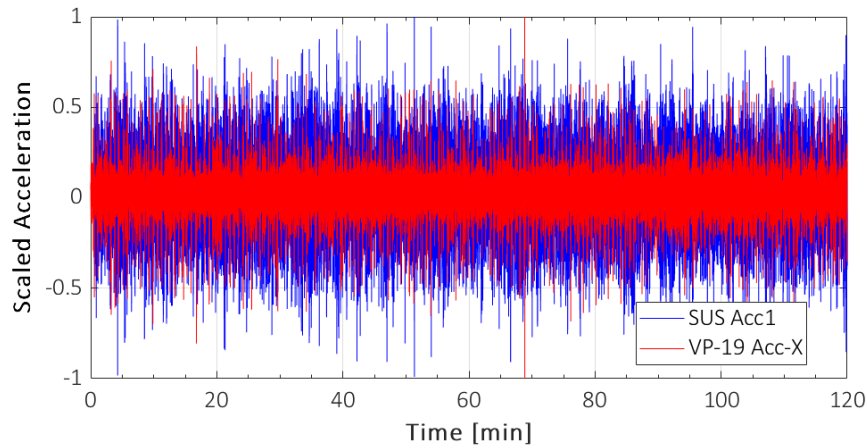


**Figure 2.17:** Normalised, bandpass filtered and lag-corrected Acc1 and VP-19 Acc-X acceleration signals overlain.

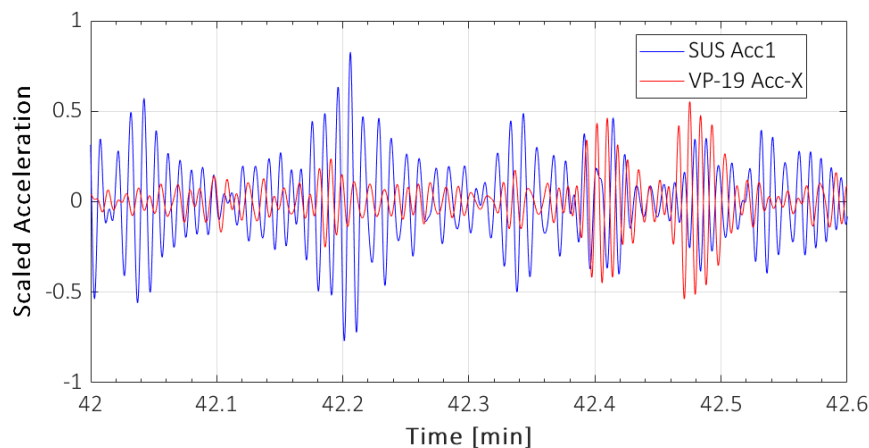


**Figure 2.18:** Zoomed in from Fig. 2.17: scaled, bandpass filtered and lag-corrected Acc1 and VP-19 Acc-X acceleration signals overlain

Completion of 1000 iterations with the chosen 20 data pairings, allowed to derive the trend lines of the collected lag values between each pairing. In Fig. 2.11, the identified lag values from all iterations, between the pairing of VP-19 X-directional displacement and SUS gauge 5C readings, were plotted with respect to the respective start time of the SUS data segment in each iteration. It can be observed that there is a time-dependent lag between SUS and soil data, which has a change rate of  $-2.0974$  s/day, according to the gradient of the linearly fitted line. Furthermore, the duration of a time unit (e.g. a second) according to SUS DAQ system clock was shorter than in the clock of the soil DAQ system - like between RNA and SUS data in Sec. 2.2.2. It can be stated because soil data was found to be lagging 59.51 minutes behind SUS data and the trend line in Fig. 2.19 is decreasing. Similar trend was found with other pairings also.

It is visible in Fig. 2.19 that several lag value data points are missing between 21-22 Aug 2017. These datapoints are missing, because the lag estimates were too far off to fit in the same



frame with the general trend. The outliers corresponded to periods with low wind speeds or standstill conditions, where signal to noise ratio is low because of low level of excitation. In Fig. 2.20, 10-min average wind speed and rotor speed have been plotted to support the statement. In the process of determining the linear trend lines and respective line gradients that show lag change rates (like in Fig. 2.19), the outliers were neglected.

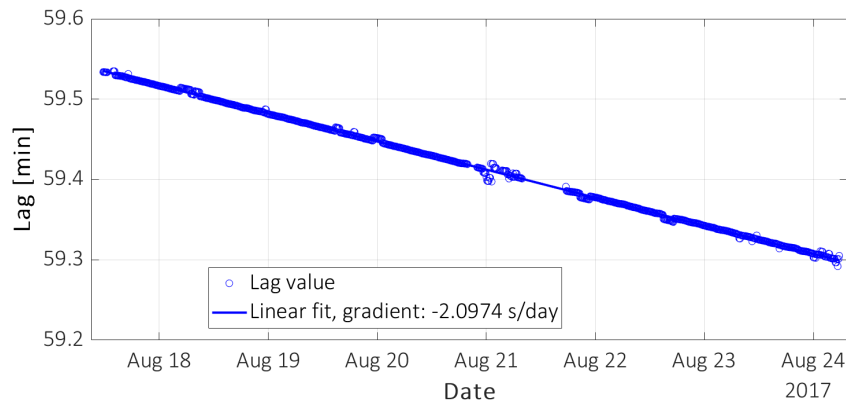


**Figure 2.19:** August period lag identification study results from the filtered and scaled VP19 X-directional displacement and SUS gauge 5C signal pairing.

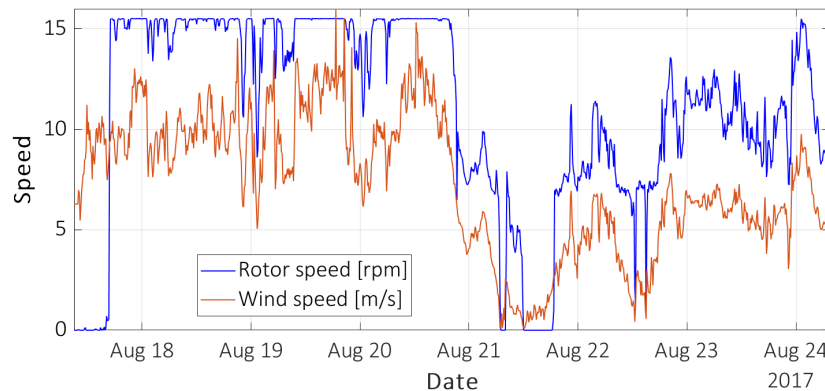


**Figure 2.20:** 10-minute average wind speed and rotor speed development over the "August 2017" lag identification study period.

In case of all studied pairings, not all lag values from 1000 iterations matched the found linear relation. Hence, the number of matches could be associated with a level of confidence in the resulting two important parameters for the lag correction - mid-period lag value and rate of change of lag. These parameters, together with the number of matches, are provided in Table 2.5 for all 20 pairings. As a reminder, "August 2017" mid-period lag value is considered to be the lag value from the linear fitted line at 22/8/2017 03:10:00.

From the complete overview of lag identification results in Table 2.5, the parameters for the lag correction were determined. To be noted, the pairings (16 out of 20), which had more than 725 matches out of 1000 iterations, provided very similar results. Thus, the results from these 16 pairings were trusted more and were used for calculating the average rate of change ( $R_{cor}$ ) and mid-period lag value ( $C_{ref}$ ). Resultantly, mid-period lag between SUS and soil data was

found to be 59.373 minutes and the average rate of change in lag as -2.1 s/day. Having these two parameters in place, synchronisation corrections could be made.

**Table 2.5:** SUS and soil data lag identification results from 20 pairings.

CCS Pairing	Lag change rate, $R_{cor}$ [s/day]	No. of matches (out of 1000)	Mid-period value, $C_{ref}$ [min]
VP19 Acc-X and Acc1	-2.10	804	59.374
VP20 Acc-X and Acc1	-1.68	702	59.408
Disp. VP19-X and Str. 4A	-2.10	890	59.373
Disp. VP20-X and Str. 4A	-2.11	876	59.373
Disp. VP19-X and Str. 4B	-2.03	725	59.375
Disp. VP20-X and Str. 4B	-2.10	896	59.373
Disp. VP19-X and Str. 4C	-2.10	893	59.373
Disp. VP20-X and Str. 4C	-2.11	874	59.372
Disp. VP19-X and Str. 5A	-2.10	867	59.373
Disp. VP20-X and Str. 5A	-2.11	860	59.372
Disp. VP19-X and Str. 5B	-2.03	715	59.375
Disp. VP20-X and Str. 5B	-2.10	899	59.373
Disp. VP19-X and Str. 5C	-2.10	864	59.373
Disp. VP20-X and Str. 5C	-2.10	879	59.373
Disp. VP19-X and Str. 6A	-2.10	892	59.373
Disp. VP20-X and Str. 6A	-2.11	884	59.372
Disp. VP19-X and Str. 6B	-2.03	711	59.375
Disp. VP20-X and Str. 6B	-2.09	890	59.373
Disp. VP19-X and Str. 6C	-2.10	884	59.373
Disp. VP20-X and Str. 6C	-2.11	871	59.373

For performing the corrections between SUS and soil data, several aspects have to be considered. Firstly, SUS data was found to be ahead of soil data by 59.373 minutes in time at mid-point of “August 2017” period. Moreover, SUS data was approximately synchronized with RNA data prior to the lag identification between SUS and soil data – only the stretching was not applied to SUS data within the “August 2017” period. Now, if soil data is corrected to align with SUS data, and SUS data is stretched, all data sets could be considered closely synchronized. What is more, similarly to the results in this section, in Sec. 2.2.2 it was found that SUS DAQ system clock had a shorter definition of a time unit. Due to the latter, the lag was identified to be time-dependent – this has been captured by the rate of change factor ( $R_{cor}$ ). In this section,  $R_{cor}$  was identified as -2.1 s/day between SUS and soil data. In Sec. 2.2.2,  $R_{cor}$  was estimated to be 2.1 s/day between SUS and RNA data over the “August 2017” period (see Table 2.4). The sign difference is caused by the fact that in this section SUS data was ahead of soil data, and in Sec. 2.2.2 SUS data was identified to be lagging behind RNA data. Consequently, lag time-dependency between SUS data and other two source in the “August 2017” period can be removed by stretching SUS data with and absolute  $R_{cor}$  factor of 2.1 s/day.

Thus, for achieving synchronisation soil data time stamps can be adjusted by adding a value of 59.373 minutes. With regards to the SUS data, no further corrections were done as part of the soil and SUS data synchronisation. Instead, the already corrected (stretched) SUS data from Sec. 2.2.2 could be used. Because the absolute rate of change of lag factor of 2.1 s/day was

approximated to be exactly the same between SUS and soil data, and SUS and RNA data over the “August 2017” period.

To demonstrate the validity of aforementioned statements and a successful application of the correction, Fig. 2.21 has been presented. If outliers are ignored, then the newly found lag values are less than 1.5 seconds. What is more, the rate of change of lag has been visibly reduced to a negligible level from 2.1 s/day in Fig 2.19.

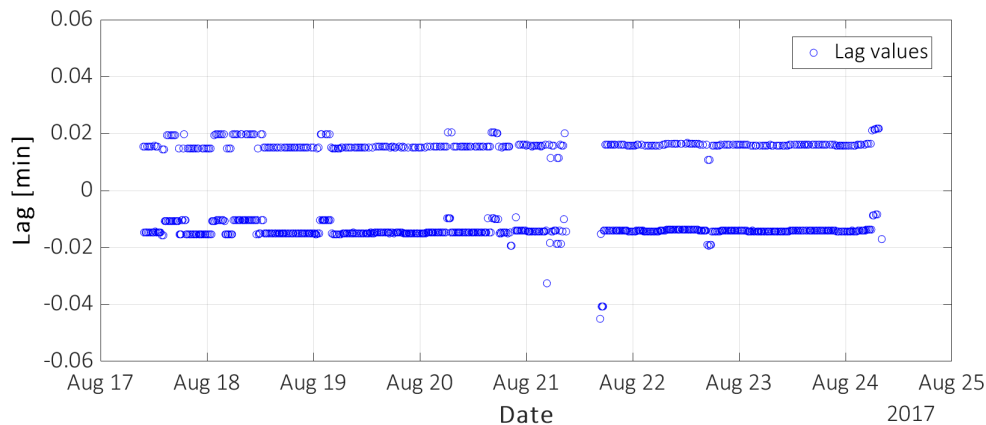


**Figure 2.21:** August period lag identification study results from the filtered and scaled VP19 X-directional displacement and SUS gauge 5C signal pairing after the application of lag correction.

#### 2.2.4 Synchronisation of RNA Data and Soil Data

The only way to identify the lag between RNA and soil data during the “August 2017” period (16/08/2017 16:00 -27/08/2017 14:20) is to check the 10-minute statistical readings as per the timeline in Table tab:timeline. In Fig. 2.22 the soil sensors VP-19 and VP-20 X-directional and RNA FA acceleration 10-minute standard deviation values have been plotted against their original time vectors. In the figure, the standard deviation readings from each source signal have been scaled to [0, 1] range.

Comparison of peaks and troughs in RNA and soil data statistics allows to detect that the lag between soil and RNA data is approximately 60 minutes. This value can differ by five minutes, because 10-min statistics was used. The exact value cannot be found because there is no continuous time series of RNA data during the “August 2017” period. However, the value of 60 minutes suggests that the soil DAQ system clock had a time-zone setting corresponding to GMT+0, whereas RNA DAQ system clock is known to correspond to GMT+1.

With this consideration, some additional adjustments were required to be made to corrected SUS and soil data sets from Secs. 2.2.2 and 2.2.3. In Sec. 2.2.3, it was determined that the soil data lagged behind SUS data by 59.373 minutes at mid-point of “August 2017” period. At the same time, SUS data was made to be in sync at that mid-point with RNA data, based on the estimated lag correction parameters in Table 2.4 in Sec. 2.2.2. Consequently, soil data timestamps had to be increased by  $60 - 59.373 = 0.627$  minutes. Similar adjustment would need to be applied to SUS data timestamps in the “correction period” 16/8/2017 - 26/7/2018, in Table 2.4. Alternatively, the stretching correction of SUS data with Eq. 2.2 - over the same “correction period” - should have been done with  $C_{ref} = 82.314 + 0.627 = 82.941$  minutes.

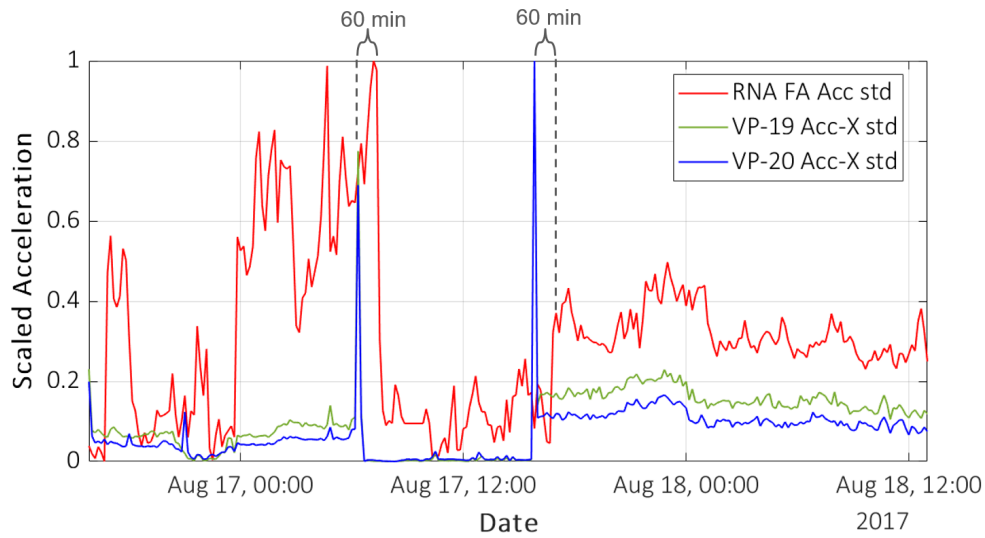


**Figure 2.22:** August period 10-minute statistics comparison - standard deviation of RNA FA acceleration, and soil sensors VP-19 and VP-20 X-directional accelerations

### 2.3 Summary & Discussion

This chapter presented an overview of the data sources and the required preprocessing of the datasets. The results of lag identification and synchronization between the three data sources, revealed that the definition of a time unit was shorter in the SUS DAQ system, than in the soil and RNA DAQ system clocks. The underlying reasons were not able to recover, as the SUS DAQ system has now been discarded.

The shorter definition of a time unit resulted in a time-dependent lag between SUS data and the other sources. What is more, in Sec. 2.2.2 it was revealed that the time-dependency of lag was changing in time - different lag increase rates were identified in each study period (Table 2.2). At the same time, lag increase could be approximated to be linear over the SUS and RNA data lag identification study periods. Hence it was decided to divide the whole two years (04/03/2016 – 26/07/2018) of SUS data into three "correction periods" (see Table 2.4), where lag change was approximated to be linear with defined parameters ( $T_{ref}$ ,  $R_{cor}$ ,  $C_{ref}$ ). With the defined parameters, SUS data was stretched, with Eq. 2.2. The resulting errors with this approach were deemed acceptable.

In Sec. 2.2.3, the absolute lag change rate between SUS and soil data in the "August 2017" period was approximated to be 2.1 s/day. The same rate was guessed to exist between SUS and RNA data in Sec. 2.2.2 during the same period - allowing to assume that the RNA and soil DAQ system clocks had the same definition of a time unit.

Thus, the only source of lag between RNA and soil data was assumed to be the difference in time-zone settings in corresponding DAQ system clocks. This assumption was supported by two results. Firstly, in Sec. 2.2.4, soil and RNA data statistics comparison showed that soil data is lagging behind RNA data by 60 minutes. Secondly, in Sec. 2.2.3, the lag identification results suggested that the lag between RNA and soil data is close to 60 minutes.

With considerations to all performed lag identification results, appropriate adjustments were performed on soil and SUS data to make these synced with RNA data. To demonstrate successful synchronisation of all data sources, acceleration data 10-min standard deviation values from all

sources over part of the "August 2017" period are presented in Fig. 2.23. Again, min-max scaling (Eq. 2.1) was applied on standard deviation readings in Fig. 2.23.

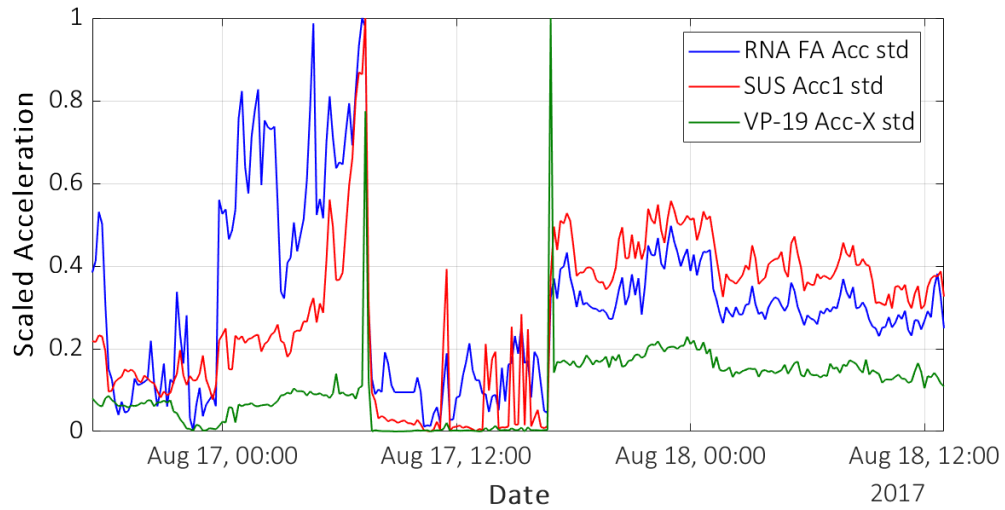


**Figure 2.23:** August 2017 period 10-minute statistics comparison - standard deviation of RNA FA acceleration, SUS Acc1, and soil sensor VP-19 Acc-X readings



## Chapter 3

# Data Analysis

Completion of synchronization of data sets now allows to explore the data to the fullest. First a look is provided into the performance curves, derived from RNA data, to look into the wind turbine behaviour. Next, the resonance frequency of the wind turbine throughout the measurement campaign is studied, followed by the analysis of inclinometer and strain data. Strain data is transformed to moments, which are used for fatigue analysis.

### 3.1 Performance Curves & Operational States

The performance or state curves of a wind turbine are considered to be, among many others, the relationships between: (a) rotor speed - wind speed; (b) power – wind speed; (c) pitch angle - wind speed; (d) power - rotor speed. These are respectively shown in Fig. 3.1 for the herein studied W27 OWT. Performance curves are necessary to monitor the operating conditions of wind turbines, allowing to observe deviations from warranted performance curves and plan maintenance. Herein the performance curves are plotted in order 1) to understand the behaviour of the main OWT control parameters in practice, 2) identify and classify usable data for analysis in this chapter and 3) justify that no evident faults are present in the operation of the turbine. The curves in Fig. 3.1 are made out of RNA 10-min statistical data collected over a four-year period (Table 2.1).

**Table 3.1:** OWT design parameters:  $V_{rated}$ ,  $V_{in}$ ,  $V_{out}$ ,  $P_{rated}$

Parameter	Design/Model Value
Rated wind speed, $V_{rated}$	12 m/s
Cut-in wind speed, $V_{in}$	4 m/s
Cut-out wind speed, $V_{out}$	25 m/s
Rated power, $P_{rated}$	3 MW

The power-wind speed curve in Fig. 3.1b confirms that power at rated wind speed ( $P_{rated}$ ) is 3 MW and rated wind speed ( $V_{rated}$ ) is around 12 m/s - point where the maximum power generation is achieved. Additionally, cut-in wind speed ( $V_{in}$ ) can be seen to lie close to 4 m/s, a point where the power curve starts to increase similarly to a sigmoid function, in case of operational conditions. A horizontal line at about zero generator output can be seen – representing idling or parked states. The data points that lie between these two curves/lines are transitional points,

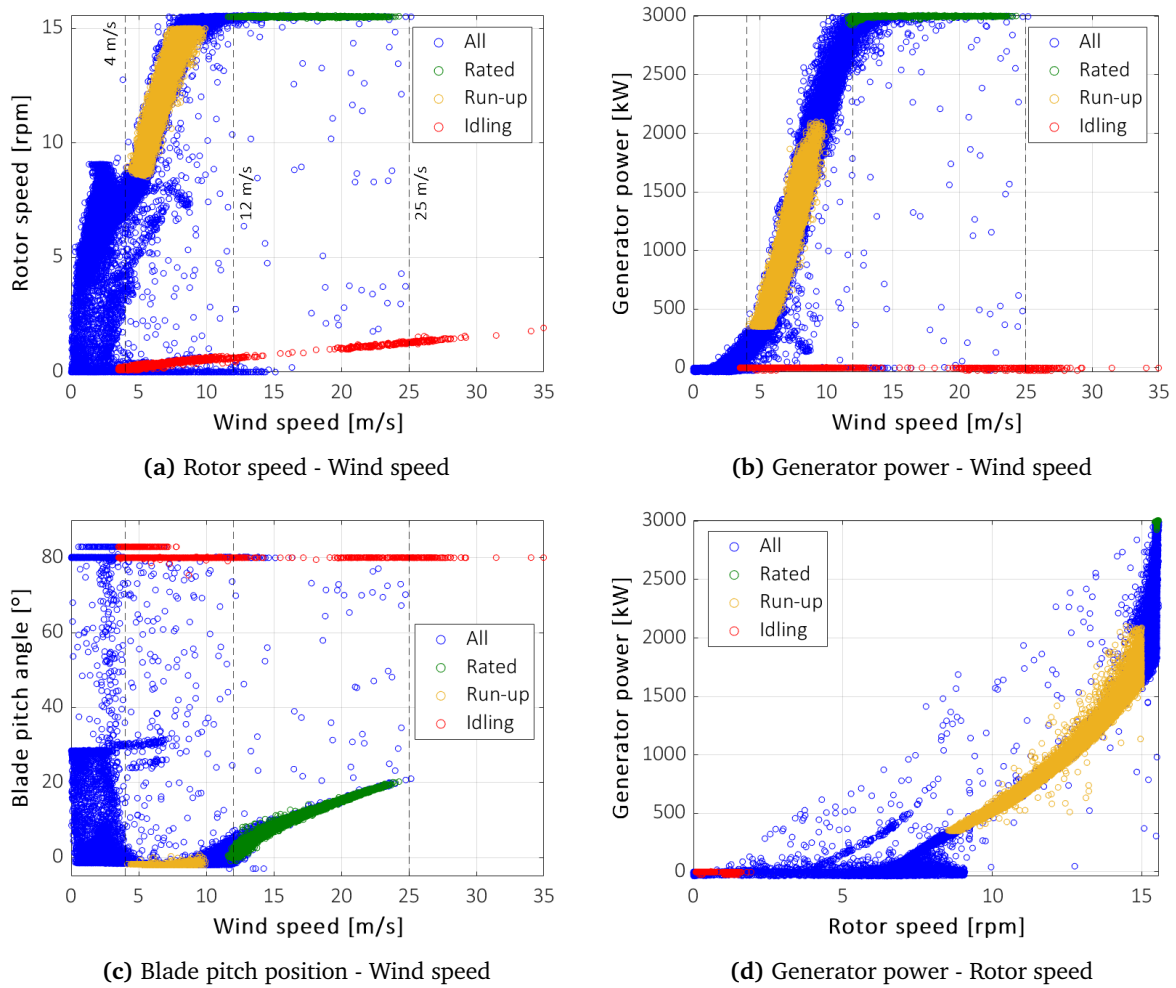


**Figure 3.1:** Performance curves based on RNA 10-minute statistical data.

the turbine is changing states. What is more, cut-out wind speed ( $V_{out}$ ) is approximately 25 m/s as the power generation drops away. The identified  $P_{rated}$ ,  $V_{rated}$ ,  $V_{in}$  and  $V_{out}$  match the chosen model parameters that were used in the design phase of W27 – these are presented in Table 3.1.

In Fig. 3.1a, the wind speed–rotor speed indicates that from around  $V_{in}$  at 4 m/s there is an almost linear growth – called the run-up state – up until rated rotor speed ( $n_{rated}$ ) at 15.5 rpm. The almost linear line reaches  $n_{rated}$  at a wind speed of around 8 m/s and then remains steady until  $V_{out}$  at 25 m/s. The definition of the run-up phase that will be also used in Sec. 3.5.2 is provided in Table 3.2 and indicated in yellow in Fig. 3.1a. Other operational states that are in interest for the designers and for the study in Sec. 3.5.2 are rated and idling states. These have been defined also in Table 3.2. To note, in Table 3.2, subscript  $m$  refers to the 10-minute average value, and subscript  $min$  to the 10-minute minimum value. The remainder of data points in Fig. 3.1a are as expected and no abnormalities can be detected visually.

The wind speed– blade pitch angle curve is depicted in Fig. 3.1c. The feathering position for OWT idling and above cut-off wind speed states appears to be around 80°. Feathered position refers to a situation when blades are pitched close to parallel with wind direction to reduce unwanted rotational torque. Examining the region below  $V_{in}$  and pitch positions at less than



80°, a stand-by state can be distinguished, at which the pitch position is lowered from the fully feathering position to boost rotor speed for start-up at sufficient wind speeds. Reversely, the pitch angle is increased to slow down the rotor for shut-down [44, 26, 6]. A vertical route from 80° to 28° is evident and then there is a scattered region between 28° and -2.9°. Both regions correspond to the aforementioned functions of boosting and slowing down the rotor speed. Moreover, between  $V_{in}$  and  $V_{rated}$ , the pitch angle is predominantly at around 0° for maximum output and above  $V_{rated}$  the blades are continuously adjusted to maintain rated output. The latter implies a curvy trend.

In comparison with the theoretical state curves presented in [44], the RNA data appears valid based on figures in Fig. 3.1.

**Table 3.2:** Definitions of W27 OWT states

OWT State	Limiting Parameters
Idling	$0.08 \text{ rpm} < n_m < 1.93 \text{ rpm};$ $3.5 \text{ m/s} < V_m < 35 \text{ m/s}$
Run-Up	$350 \text{ kW} < P_m < 2100 \text{ kW};$ $8 \text{ rpm} < n_m < 15 \text{ rpm};$ $V_m < 11 \text{ m/s}$
Rated	$P_m > 2900 \text{ \& } P_{min} > 2700;$ $n_{min} > 14.5 \text{ rpm}$

### 3.2 Wind Speed, Damping & Resonance Frequency Dependencies

In this section, only RNA 10-minute statistical data from the evaluated period of four years will be used (Table 2.1). According to the different design models, which were developed with SGRE's in-house aeroelastic code – BHawC -, a range of eigenfrequencies were determined. Two distinct farm-wide design positions were reported in the design report: low frequency design position, and high frequency design position. Lowest frequency design position corresponded to the deepest water position of the nearshore wind farm and with soft soil conditions. The highest frequency position was found for conditions with shallowest water position with clamped soil conditions 1m below the seabed level.

The lowest frequency from the respective design position was determined to be 0.275 Hz and the highest frequency from the respective design position was found at 0.32 Hz. Both values correspond to their respective 1<sup>st</sup> FA SUS bending mode. The estimated design value for W27 turbine was reported as 0.279 Hz. To provide a comparison with the values in the data, the 10-min average resonance frequency dependency on wind speed is presented in Fig. 3.2.

Knowing that the RNA resonance frequency 10-min averages may be subject to some discrepancies due to the curve-fitting based method in the energy producing state, it was decided to additionally look at the data from the perspective of standstill conditions. The latter is known to provide more accurate estimates. In this case, the idling condition was defined as having a 10-min maximum power output lower or equal to 0 kW, and the 10-minute average rotor speed less than 3 rpm. Production condition was defined to have a 10-min average rotor speed above

5 rpm and the 10-minimum rotor speed as 4.5 rpm. In Fig. 3.1d, rotor speed of around 5 rpm corresponds to the point where turbine starts to generate power.

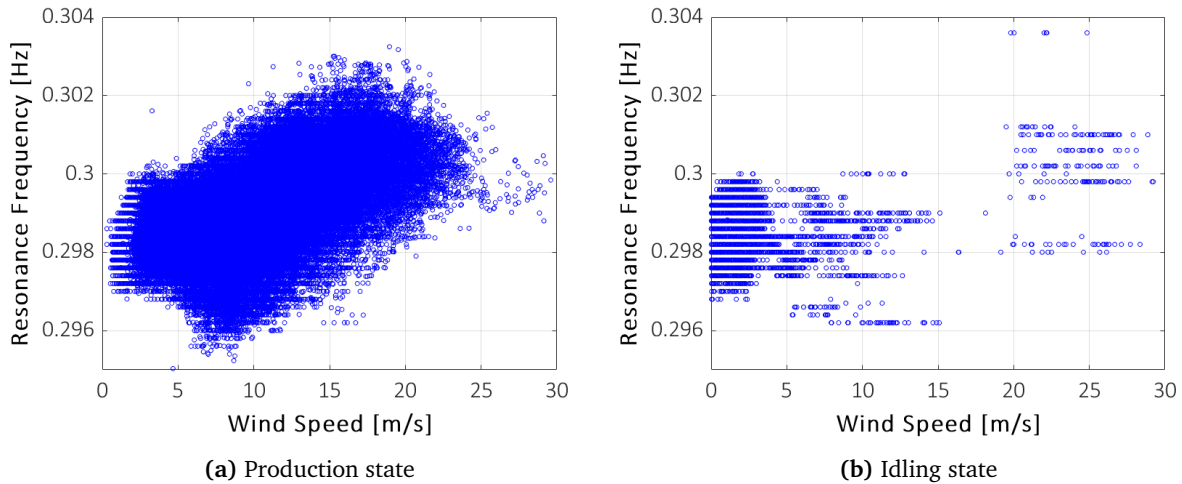


**Figure 3.2:** 10-min average resonance frequency *versus* wind speed at the defined OWT operational states

Figures 3.2a and 3.2b indicate that with the increase in wind speed the resonance frequency is also increasing. Hence, there is some stiffening effect in the system, despite the presence of higher damping at higher wind speeds due to feathering of the blades. Additionally, it can be observed that the frequency varies between 0.295 and 0.304 Hz. These values lie between the low and high design point estimates from modelling. The discrepancy between the W27 estimate of 0.279 Hz, which is close to the low frequency design point value, and values in data indicate that the turbine is located in stiffer than estimated conditions. This would mean, the soil is not as soft as in the low design point case and/or W27 is not located in the deepest water position of the farm.

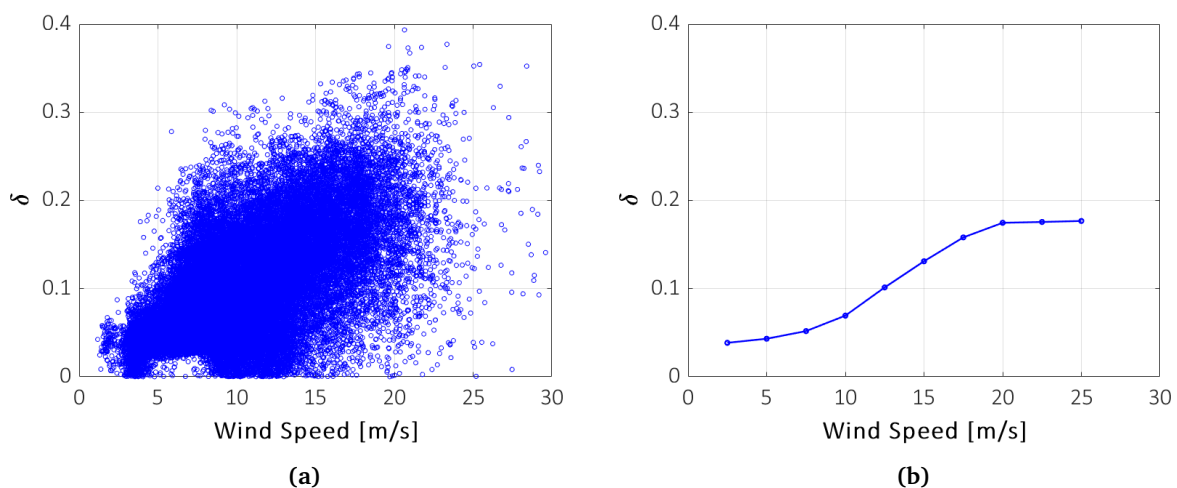


**Figure 3.3:** (a) 10-min average SS logarithmic decerment estimate *versus* wind speed at the defined production conditions; (b) the average decrement values per wind speed range, data points are located at the centre of the respective wind speed bin.

To provide evidence of higher damping due to the increase in wind speed, the SS logarithmic decrement ( $\delta_{SS}$ ) estimates in production state are plotted against wind speed, in Fig. 3.3. Side-side estimates were chosen because their estimates are known to be more reliable. For idling state  $\delta_{SS}$  estimates have not been shown because there were too few data points to cover the whole considered wind speed range. The logarithmic decrement estimates exist for only half of the evaluated period of four years. The increase in  $\delta_{SS}$  is associated with the increase in aerodynamic damping, which is related to the pitch position of the turbine blades. A noticeable increase in  $\delta_{SS}$  occurs between wind speeds 10 - 20 m/s - a range that in majority falls into rated OWT operational state. In Fig. 3.1c, the pitch of turbine blades increases from 10 m/s onwards near rated and at rated state. Thus, increased pitch of blades translates to higher aerodynamic damping and observed increasing trend in Fig. 3.3b.

In Fig. 3.4, the average resonance frequency values per wind speed are shown. Due to lack of data points in the defined idling state (Fig. 3.4b) the curve is not as smooth as in production state (Fig. 3.4a). However, the increasing trend is apparent in both figures.

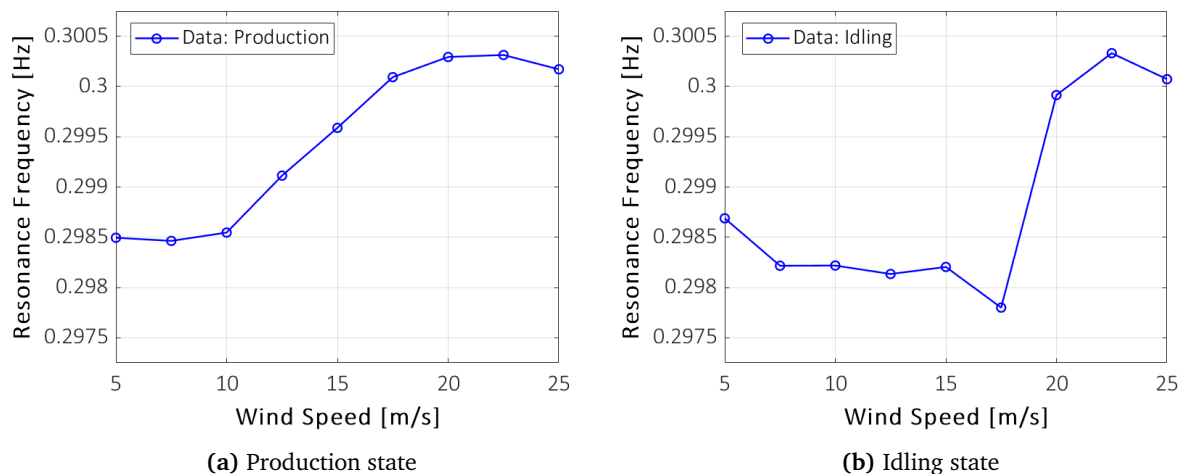


**Figure 3.4:** Average resonance frequency per wind speed range at the defined conditions, data points located at the centre of wind speed bin values. Based on values presented in Fig. 3.2

The average trend line corresponding to production state shows that the resonance frequency remains level at below rated wind speed (12 m/s) conditions. At around rated wind speed conditions, the resonance frequency starts to increase until wind speeds above 20 m/s.

In case of the trend line corresponding to idling state (Fig. 3.4b), a slight drop occurs between 5 to 7.5 m/s wind speed conditions. That is followed by a constant resonance frequency level up until a wind speed level of 15 m/s. With a slight drop at 17.5 m/s, the resonance frequency increases. It has to be noted from Fig. 3.2b, that the averaged values between wind speeds 12.5 to 20 m/s in Fig. 3.4b have been derived from little amount of data points. Thus, the results can appear biased.

In Fig. 3.4a, the difference between the highest and lowest average resonance frequency values is approximately 0.0018 Hz and in Fig. 3.4b it is 0.0025 Hz. Both differences are less than 1% of data values in Fig. 3.2a, thus the change is small. Additionally, in case of the idling state (Fig. 3.4b) the low average resonance frequency value at 17.5 m/s is heavily affected by data bias in the form being calculated from lack of data points (Fig. 3.2b). To add, the level of error in resonance frequency values was  $\pm 0.0002$  Hz, excluding noise-induced errors that have

an unknown influence on the accuracy. What is more, it was checked that according to the low frequency design model the change can be around 2%, so higher than the observed percentage change in measured data. Less than 1% change in resonance frequency can also fall into the region of statistical scatter caused by variable environmental conditions. For example, in case of Vestas V112-3.0 OWTs in the Eneco Luchterduinen wind farm, it has been found that a water level variation of 1.5 m (or more) can cause a 2% change in resonance frequency [36]. In the IJsselmeer, where W27 is located, the water level can vary by more than a meter, depending on wind speed, wind direction and time of the year [40]. In conclusion, based on the raised sources of uncertainty and scatter, the observed change in resonance frequency is considered small.

Although the changes in average resonance frequency values is small, the cause of the increasing trend in Fig. 3.4a remains a question. Due to the fact that the resonance frequency starts to increase near  $V_{rated}$ , suggests that the trend is associated with increased level of damping and the way the resonance frequencies are estimated by RNA DAQ system. Firstly, in Fig. 3.1c, it was shown that above  $V_{rated}$ , the pitch of the blades starts to increase, and consequently there is an increase in aerodynamic damping, which is the main source of damping in. The latter is demonstrated in Fig. 3.3, where the trend line is similar to the resonance frequency increase in Fig. 3.4b.

Regarding the method of resonance frequency estimation, the frequency values are found via a curve-fitting method. The method entails fitting the frequency response function of a simplified computational model of the wind turbine with the one derived from measured acceleration data. In the computational model, damping of the OWT is included via Rayleigh's formulation, which has a stiffness proportional term ( $\psi \mathbf{K}$ ) [43]. The Rayleigh equation is the following:

$$\mathbf{C} = \tau \mathbf{M} + \psi \mathbf{K} \quad (3.1)$$

where  $\mathbf{C}$  represents the damping matrix;  $\mathbf{M}$  is the mass matrix;  $\mathbf{K}$  is the stiffness matrix;  $\tau$  and  $\psi$  are constants of proportionality.

Based on Eq. 3.1, if damping increases and involved mass remains the same, stiffness has to increase, and vice versa. Stiffness is proportional to the resonance frequency and thus the trends in Figs. 3.4b and 3.3 show similar dependency with wind speed. Given the similarity in trends, the mass proportional term ( $\tau \mathbf{M}$ ) in the computational model formulation either has less influence in comparison to the stiffness proportional term or it is not included.

### 3.3 Wind Turbine Tilt Analysis

The measured inclination of the W27 turbine after the installation was  $0.14^\circ$  in an unknown direction. For reference, according to the imposed design requirements, the maximum allowed permanent pile tilt at the interface is  $0.25^\circ$  after installation and  $0.5^\circ$  by the end of the lifetime.

The unidirectional inclinometer, that is part of the SUS DAQ setup, was located inside the pile at 4.5 m above NAP (Fig. 3.5a). The device was positioned at  $39.4^\circ$  from the North and measured tilt along the  $39.4^\circ$ – $219.4^\circ$  line. Hence, to identify maximum tilt values, which correspond to FA motion, only the following environmental and operational conditions were considered:

- wind direction and RNA orientation at  $39.4^\circ \pm 20^\circ$ ;
- wind direction and RNA orientation at  $219.4^\circ \pm 20^\circ$ .

The  $\pm 20^\circ$  deviation was chosen to have sufficient data points, while retaining the directional requirement. Once the time instances meeting the directional requirements have been identified

from the RNA data, the associated 10-min statistics of the inclinometer readings are calculated. The 10-min averages of the inclination are subsequently plotted against the corresponding 10-min mean wind speed (from RNA data), as presented in Fig. 3.5b.

In the figure, a distinction has been made between the winds coming from directions  $39.4^\circ$  and  $219.4^\circ$  with allowed deviations, and several observations can be made:

- Inclination in data points is negative, the pile appears to be tilted towards the  $39.4^\circ$  side, as illustrated in Fig. 3.5a. However, because there are no records of the inclinometer being calibrated after the installation of the SUS DAQ system, it cannot be confirmed.
- Two thrust curve shapes have formed with an absolute maxima located at  $V_{rated}$ ; reproducing the figure found in literature [33].
- The points between  $-0.25^\circ$  and  $-0.30^\circ$ , in the wind speed range 5 to 30 m/s do not follow the thrust curve trends but remain level.
- Data points seem to have excessive scatter, for example the 'FA – wind  $219.4^\circ$ ' data points appear to form several thrust curves. Similarly, the points between  $-0.25^\circ$  and  $-0.30^\circ$  form multiple horizontal trend lines. This points to the possibility of permanent deformations in the soil or pile, or drifting of inclinometer output. Drifting refers to a change in the sensors zero point with time and it is known to occur in inclinometers deployed for long-term monitoring [29].

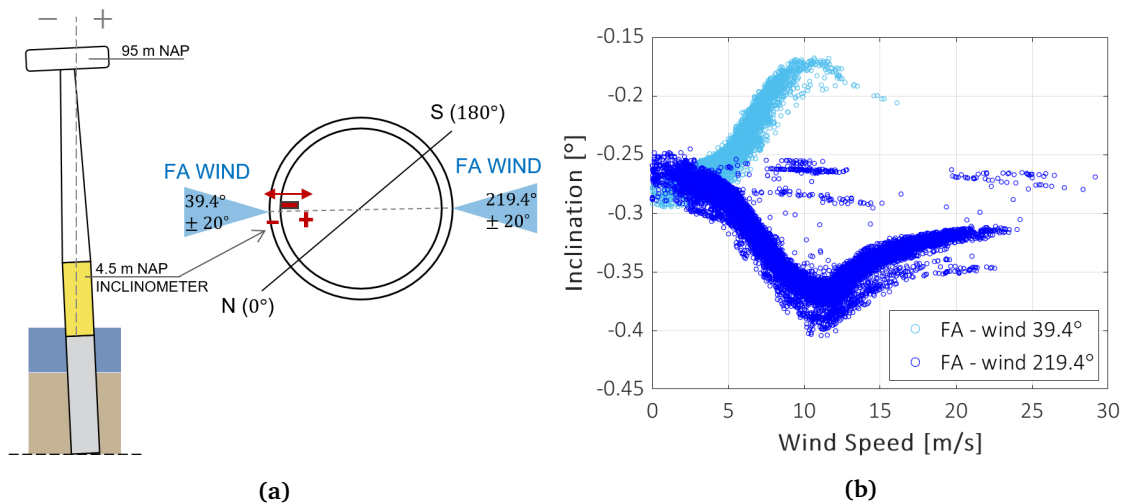


**Figure 3.5:** (a) Sketch of the tilting of the OWT along the  $39.4^\circ - 219.4^\circ$  line according to data statistics, and a visualization of the sign convention of the inclinometer and the considered wind directions; (b) 10-min average inclination *versus* 10-min mean wind speed, only values corresponding to the wind directions  $39.4^\circ \pm 20^\circ$  and  $219.4^\circ \pm 20^\circ$  are included

The presence of thrust curves in Fig. 3.5b relates to the applied loading on the OWT at corresponding wind speed conditions. It is presented in Sec. 3.4.4 that the loading also follows the thrust curve shape. In the case of the currently studied OWT, which is located in a lake, the main source of loading is wind. Wind loading can be idealised to act as a point load at the RNA level (95 m above NAP). Higher loading magnitude at the RNA level translates to larger deformation and tilt magnitudes at the location of the inclinometer (4.5 m above NAP).

The points between  $-0.25^\circ$  and  $-0.30^\circ$  correspond to time periods when the turbine was in parked or idling state, where turbine blades are feathered and thrust load is minimized. The remaining significant sources for the presence of inclination are then the existing permanent tilt and the tilt originating from the eccentricity of the centre of mass of the RNA with respect to the centre of the tower. The centre of mass of W27 RNA is in the direction where the rotor blades are directed. If the RNA is directed towards  $219.4^\circ$ , then the centre of mass is on the  $219.4^\circ$  side. These two sources are of static nature and thus the parked or idling state data points form horizontal trends in Fig. 3.5b.

In order to identify if permanent deformation or drifting has occurred, 10-min average tilt values in conditions where the system can be considered static should be observed. Thus the following additional constraints were required to be applied on the already filtered data: 10-min maximum rotor speed  $< 2$  rpm and 10-min average wind speed  $< 2$  m/s. Because the wind turbine has been highly operational, there were not enough data points that would fulfill those conditions in case of wind direction and yaw position being  $39.4^\circ$ . Hence, only the filtered input for the  $219.4^\circ$  directional case could be plotted against time (Fig. 3.6a).

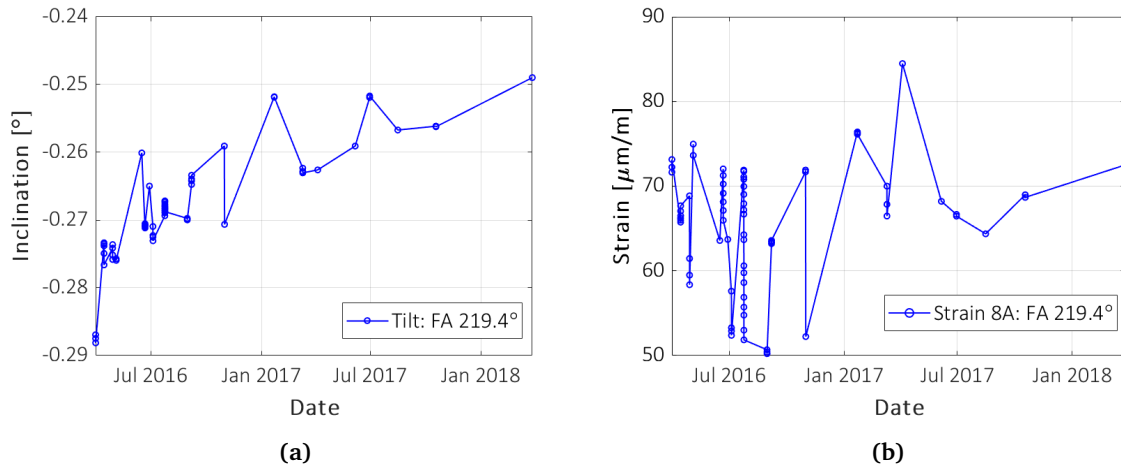


**Figure 3.6:** (a) Change in tilt of the OWT over time at conditions where 10-min  $n_{max} < 2rpm$  and the 10-min  $V_m < 2m/s$  and wind direction is  $219.4 \pm 20^\circ$ , according to 10-min statistical values; (b) change in gauge 8A 10-min average strain values over the same time instants.

Figure 3.6a shows that the OWT inclination has changed in a time span of 2 years approximately  $0.04^\circ$ . Largest change occurred at the very beginning of the shown measurement period, and since then the rate of change has decreased – indicating that the system has stabilized. On the other hand, the soundness of the readings can be debated as the inclinometer might have started drifting at some point in time. The reasoning behind the latter claim originates from the fact that the respective 10-min average strain readings from gauge 8A do not show a similar trend in Fig. 3.6b.

Gauge 8A is located 2.5 m above the inclinometer (Fig. 2.1), and thus there should be an increase in strain readings similarly to tilt. As the blades, and centre of mass, are considered to be on the  $219.4^\circ$  side, the strain gauge at location A is in tension (positive values in Fig. 3.6b). If the OWT would be tilting toward the  $219.4^\circ$  side as Fig. 3.6a suggests, then the tension should be increasing. However, this trend cannot be identified. For example, a significant change in tilt occurs before July 2016 in Fig. 3.6a, but it is not observable in Fig. 3.6b. Moreover, the difference between the first and last data points in Fig. 3.6b is close to none.

To investigate what is occurring in the data clusters that appear as vertical lines in Figs. 3.6a and 3.6b, the extended period of OWT standstill in July 24<sup>th</sup> is brought to spotlight in Figs. 3.7a and 3.7b. Inclinomometer readings suggest that at first the pile is tilting towards the 219.4° side, but then starts shifting back after 12:00, as if the soil started to recover. Alternatively, influence could have come from momentary changes in wind speed and wind direction. After all, 10-min statistical data is used and short-term changes are not entirely captured. These can cause such discrepancies. However, the strain readings, at the same point in time, suggest that tension in the gauge is decreasing, so the tilt should be increasing towards the 39.4° side from the start, whereas the centre of mass is located on the opposite side. Hence, contradicting readings from both sensors in multiple ways.

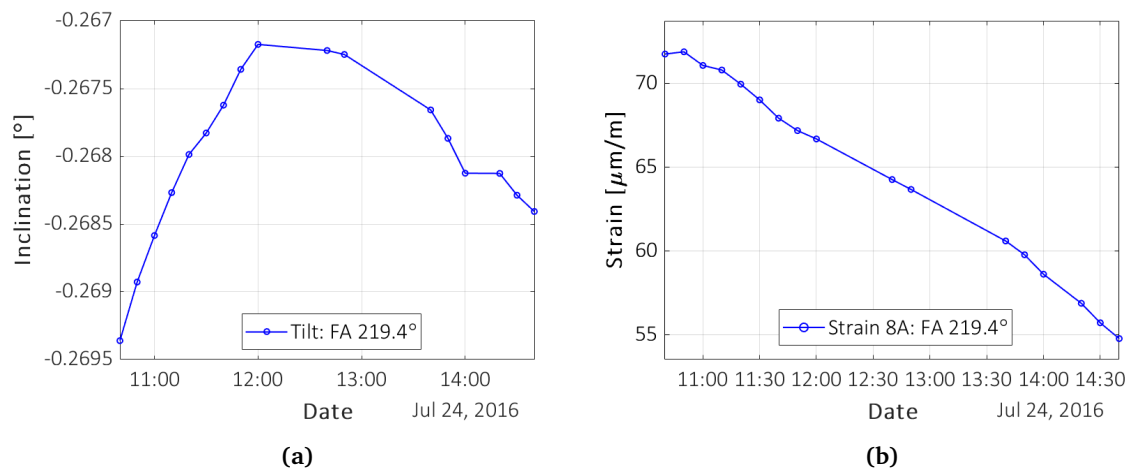


**Figure 3.7:** (a) Tilt and (b) strain development at the data cluster on 24/07/2016.

It must be highlighted that the deviation presented in Fig. 3.7a can fall into the reported level of error (1-2% of the reported values) in the readings. Moreover, the true sensitivity and accuracy of SUS sensors is unknown due to the absence of information on performed calibration after the installation of the SUS DAQ system.

In conclusion, the observed 0.04° change in tilt over a time span of two years may be due to permanent deformation or drifting, but it is small. The allowed tilt by the end of the design life of the turbine is 0.5°. If the observed change is added to the measured (after OWT installation) tilt of 0.14° in an unknown direction, the sum would be insignificant in comparison to the allowed value.

In order to identify if possible permanent deformation has occurred and caused a change in the resonance frequency of the system, the corresponding 10-min average resonance frequency values are displayed in Fig. 3.8. The start and end value have a difference of 0.0004 Hz, but no effect can be concluded because the change falls into the region of error in resonance frequency values. The level of error is known to be  $\pm 0.0002$  Hz, excluding noise-induced error.

Additionally, wind direction values are shown in Fig. 3.8, proving that the correct time periods were observed. Also, the 10-min average wind direction values in the spotlighted period (Fig. 3.8b) remain relatively constant, not providing a reasoning for change of tilting direction in Fig. 3.7a. But, 10-minute minimum and maximum wind direction readings in the spotlighted period in Fig. 3.9 do support the presence of contradicting trends in Figs. 3.7a and 3.7b, as was speculated. The minimum and maximum values significantly deviate from the 10-min average values. The duration of deviation is unknown, but an influence from these momentary deviations

is clear.

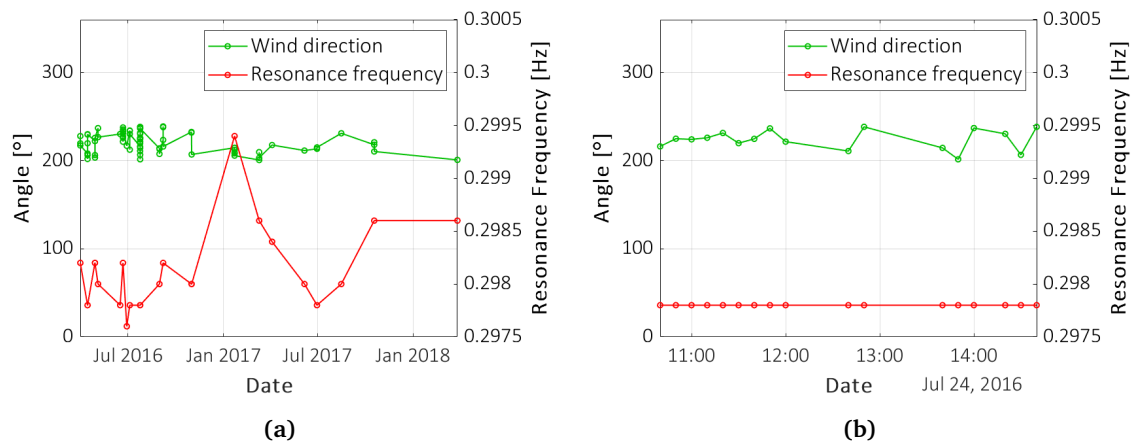


**Figure 3.8:** (a) 10-min average wind direction and resonance frequency development over the same time instants as in Fig. 3.6a; (b) values at the data cluster on 24/07/2016.

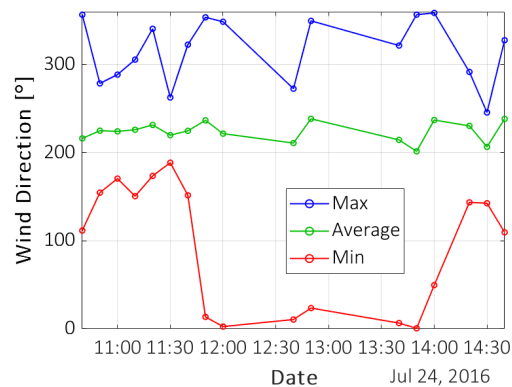


**Figure 3.9:** 10-min average, minimum and maximum wind direction development at the data cluster on 24/07/2016.

## 3.4 Moment Lines

In this section, maximum bending moments endured by the support structure over a period of 2.5 years (Fig. 2.1) are determined with the use of strain recordings and laws of mechanics, together with the information about the nacelle positioning, wind direction and rotor speed from RNA statistics. Nacelle orientation data will be used for transforming moments from their fixed coordinate system to follow the FA and SS reference system. Wind direction and rotor speed are mainly used for data filtering.

### 3.4.1 Calculation of Moments from Strain & Sign Convention

Before data analytics, the adopted sign convention and required formulas for deriving moments,  $M_{BD}$  and  $M_{AC}$ , from strain data are introduced, in junction with the information provided in Fig. 3.10.



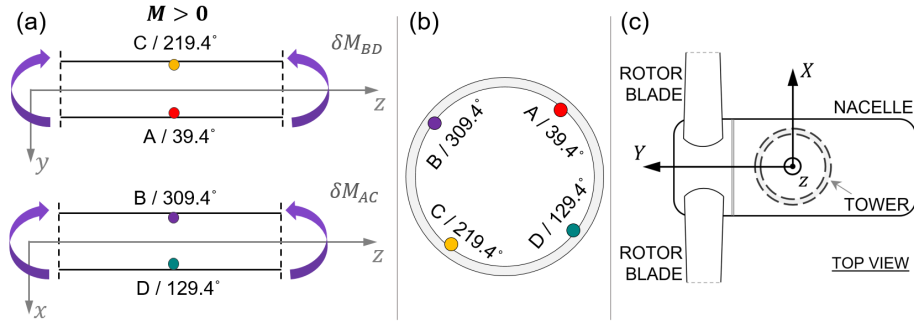


**Figure 3.10:** (a) Sketch on the adopted sign convention for bending moments; (b) positioning of the strain gauges; and (c) the local coordinate system for deriving FA and SS moments, drawn on the top view of the RNA.

The positive moment, as per Fig. 3.10, is considered when gauge A or gauge D provide positive readings – meaning that this side is in tension. Subsequently, negative strain readings would imply that there is compression on the side where the strain gauge is located. The strain-derived moments can be calculated as follows:

$$M_{BD} = \frac{EI_{xx}(\epsilon_A - \epsilon_C)}{2 \cdot y_u}; \quad M_{AC} = \frac{EI_{yy}(\epsilon_D - \epsilon_B)}{2 \cdot x_u} \quad (3.2)$$

, where  $E$  is the modulus of elasticity;  $I_{xx} = I_{yy}$  are the second moments of area about the  $x$  or  $y$  axis line;  $x_u = y_u$  are distances to the strain gauge from the centre of the pile; and  $\epsilon$  is the strain reading. Essentially, the average of the opposing strain gauge readings is multiplied with a factor to arrive at a moment value. This factor includes information about the geometry and the material properties of a cross-section. Material properties are the same at each strain gauge ring level, but the geometry – diameter and wall thickness – varies along the length of the SUS. To add, the second moment of area for a hollow circular cross-section is found as follows:

$$I_{xx} = I_{yy} = \frac{\pi(r_{outer}^4 - r_{inner}^4)}{4} \quad (3.3)$$

, where  $r_{outer}$  is the outer radius of a cross-section; and  $r_{inner}$  is the inner radius of a cross-section, found by subtracting the wall thickness of a cross-section from  $r_{outer}$ .

Bending moments,  $M_{BD}$  and  $M_{AC}$  can be transformed to bending moments in the FA and SS directions. To achieve that,  $x$  and  $y$  axes that were defined for the derivation of  $M_{BD}$  and  $M_{AC}$  in Fig. 3.10a have to align with  $X$  and  $Y$  axes that follow the movements of the yaw according to the drawn arrows in Fig. 3.10c. The  $z$ -axis is the same in both coordinate systems. According to the adopted directional conventions (Fig. 3.10),  $M_{FA}$  and  $M_{SS}$  are calculated with the use of trigonometry and information about the yaw orientation,  $\alpha_{yaw}$ , accordingly:

$$M_{FA} = M_{AC} \cos(\alpha_{yaw} - 39.4^\circ) + M_{BD} \sin(\alpha_{yaw} - 39.4^\circ) \quad (3.4)$$

$$M_{SS} = -M_{AC} \sin(\alpha_{yaw} - 39.4^\circ) + M_{BD} \cos(\alpha_{yaw} - 39.4^\circ) \quad (3.5)$$

Because the strain gauges are not located at the four cardinal directions (Fig. 3.10), but are offset by an angle of  $39.4^\circ$ , it had to be accounted for during the transformation. In equations 3.4 and 3.5, it has been done by subtracting that value from the yaw orientation value.

### 3.4.2 Determining Usability of Resistive Strain Sensors

Bonded resistive strain gauges, which were used for data acquisition, are known to be susceptible to drifting over longer measurement periods [18, 39]. Drifting is referred to as low frequency change in sensor readings with time. Reasons can include debonding of gauges from the pile surface, inaccurate temperature drift compensation or physical damage. It is known that temperature drift compensation was applied to the readings. However, the measurement duration was more than two years and strain gauges might have started to detach from the pile surface. Also, during the driving of the pile (before the start of the measurement campaign) some gauges were damaged.

Thus, a check on the usability of the survived gauges is required. For doing that, 10-min average values from periods in clean production were used. Production state was defined as having a 10-min average rotor speed as 5 rpm and the 10-minimum rotor speed as 4.5 rpm. Data points corresponding to non-production state were neglected because these appeared as irrelevant outliers in the process of identifying reliable strain gauge sensor data.

First method of evaluating the condition of the strain sensors (Fig. 2.1) is based on plotting the mean strain values with the respective 10-min average nacelle position value. In Figs. 3.11 and 3.12 that has been done with gauge 8C and 4C statistical values, per indicated wind speed ranges. In Fig. 3.11, multiple sine curves with varying amplitudes are distinguishable from the scattering of data points. It can be observed that the maxima and minima are located around  $219.4^\circ$  and  $39.4^\circ$ , as expected due to the location of C-gauges at  $219.4^\circ$  (see Fig. 3.10). Thus, at yaw positions  $129.4^\circ$  and  $309.4^\circ$ , the strain values should be zero. However, it is not the case, allowing to identify an offset of about  $35 \mu\text{m}/\text{m}$ , which must be corrected before moments are to be transformed to FA and SS directions. The found offset may originate from an initial tilt of W27 (Sec. 3.3) or some other source of static load caused offset which was not calibrated for.

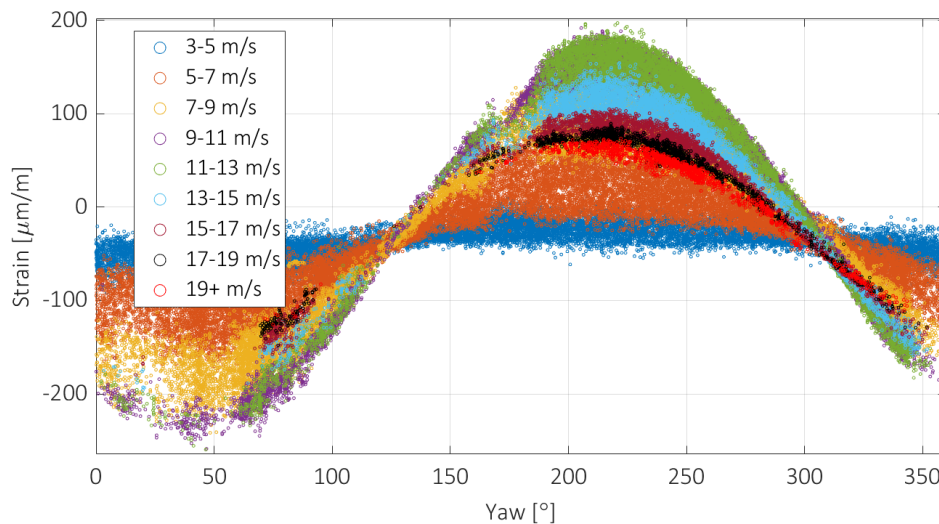


**Figure 3.11:** Gauge 8C 10-min average strain values plotted against respective 10-min average yaw position, per wind speed range.

At the same time, Fig. 3.12 reveals that 4C sensor is not working properly, because the sine curves that would be formed per wind-speed range appear to be torn into several ones. Additionally a large offset from the zero-line can be identified, but the maxima and minima are

located at right direction – similarly to gauge 8C (Fig. 3.11).

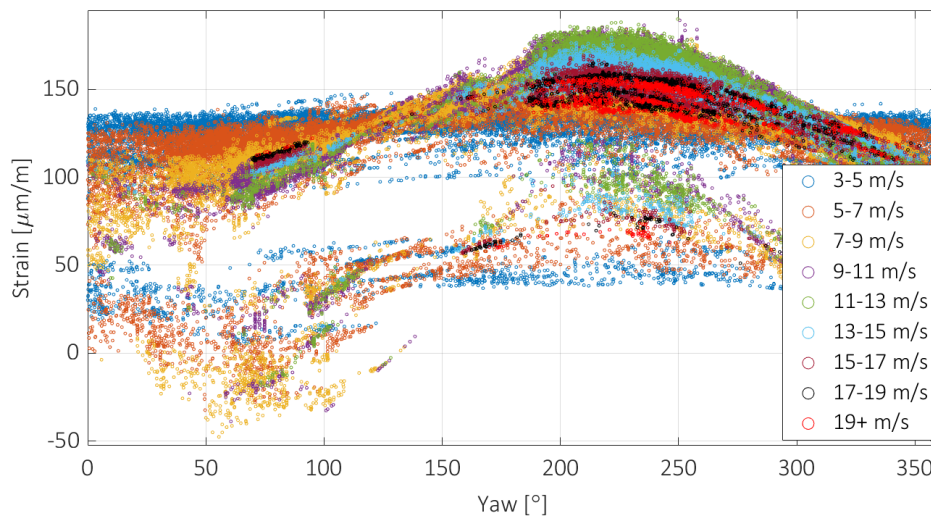


**Figure 3.12:** Gauge 4C 10-min average strain values plotted against respective 10-min average yaw position, per wind speed range.

To understand the cause for large scatter in Fig. 3.12, strain gauges 4C and 8C 10-min average values are visualized over time for several wind speed ranges, in conditions where wind direction is  $219.4^\circ \pm 20^\circ$ , in Figs. 3.13b and 3.13a. It can be observed from the comparison of these two figures that gauge 4C has drifted severely before July 2016 and has continued to waver after that. A non-drifting behavior can be seen in Fig. 3.13a, corresponding to gauge 8C data.

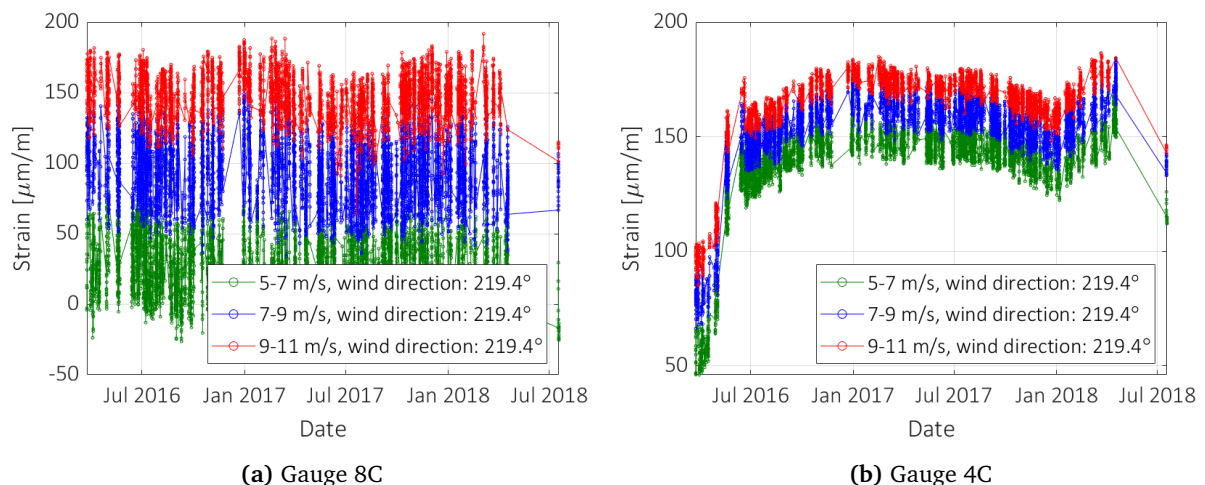


**Figure 3.13:** The development of strain gauges 4C and 8C 10-min average values over time per indicated wind speed ranges, in conditions where wind direction is  $219.4^\circ \pm 20^\circ$

Having performed the two exercises on data from all sensors, non-drifting and drifting sensors were identified. Non-drifting sensors are highlighted with green in Table 3.3. Next, a check was performed to verify that the sensitivity of sensors had not reduced as a consequence of drifting or any other reason. For the purpose of verification, the 10-min average strain values, at

conditions corresponding to approximately FA motion with respect to the location of the considered sensor at around rated wind speed, were plotted against time - see Figs. 3.14 and 3.15. Taking gauges 8C and 4C as examples for the explanation of the applied procedure, the approximate true FA moment can be found when the yaw position and wind direction are approximately  $39.4^\circ$  or  $219.4^\circ$ . By taking the opposite directions and values, which correspond to near rated wind speed levels, the maximum and minimum strain values can be identified – providing a maximum range. Next, the identified strain range can be used to calculate a maximum moment value with the following idealizing assumption, in case of gauge C:

$$M_{BD} = \frac{EI_{yy}(-\epsilon_C - \epsilon_C)}{2 \cdot y_u} \quad (3.6)$$

In comparison to equation 3.2, it can be noticed that the strain value of the opposite gauge of the reference gauge, is assumed to be the value of the reference gauge multiplied by minus one. Multiplication by minus one is required because if, for example, gauge C is providing positive readings, the opposing gauge A would provide negative readings. As a reminder, positive readings indicate tension and negative readings compression. Thus, based on the example, to compensate for the missing compressional readings, gauge C data is idealized to provide the readings with the same magnitude at both sides of the SUS. In reality, there would be some discrepancies which are dependent on the overall load level and characteristics. However, wind thrust induced bending moment is the main source of loading and linear-elastic SUS behavior is expected. Consequently, tension and compression readings from opposing sides should be of similar magnitude – so the idealization is not unrealistic. This idealizing assumption allows to test each strain gauge individually, and additionally provide an approximate maximum (quasi-)static moment value imposed on the wind turbine structure at each strain gauge ring level. To add, in case of evaluating A, B or D gauges, the subtraction of strains in respective Eq. 3.2 would respectively change to  $(\epsilon_A - (-\epsilon_A))$ ,  $((-\epsilon_B) - \epsilon_B)$ , and  $(\epsilon_D - (-\epsilon_D))$ .

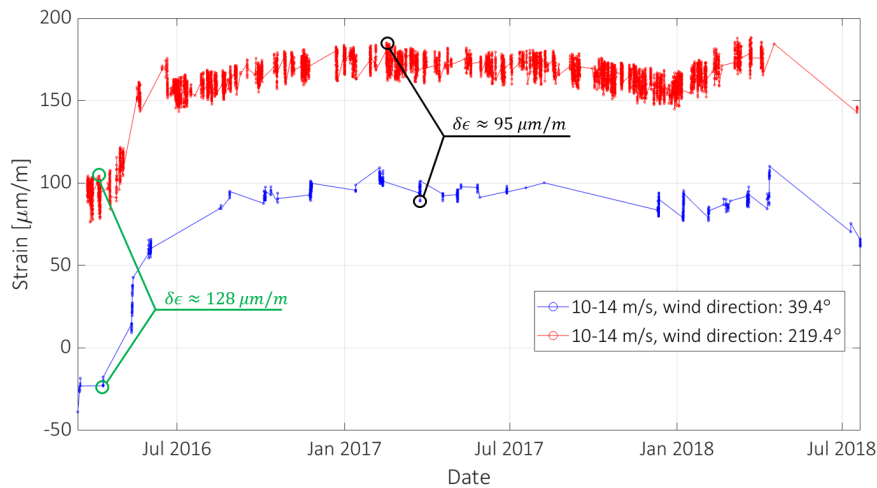


**Figure 3.14:** Drifting strain gauge 4C 10-min average values over time, in conditions where 10-min average wind direction is  $219.4^\circ \pm 20^\circ$  or  $39.4^\circ \pm 20^\circ$  and wind speed is 10-14 m/s.

Continuing the explanation of the procedure based on gauge 8C and 4C data, Figs. 3.14 and 3.15 are taken into consideration. In Fig. 3.14 gauge 4C 10-min averages corresponding to the indicated wind conditions are shown. Then, points which would give the largest strain range,

$\delta\epsilon$ , at similar points in time were picked based on visual inspection. It can be noticed that  $\delta\epsilon$  is about 26% smaller after evident drifting.

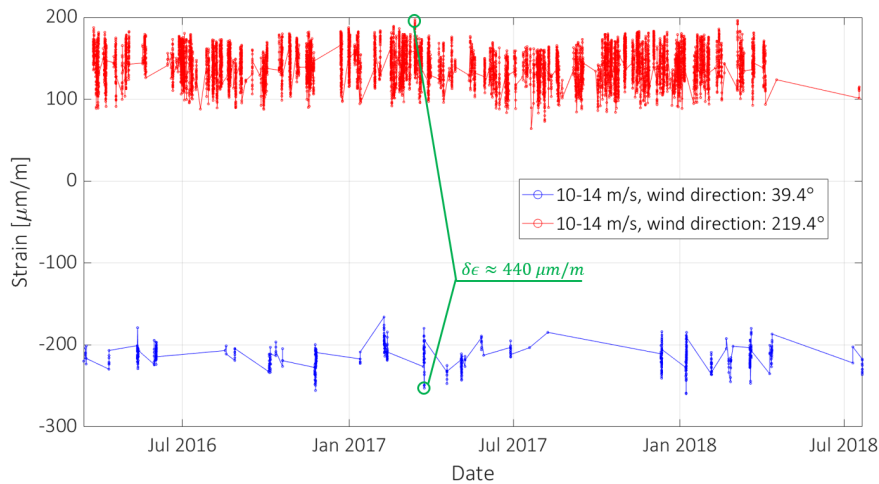
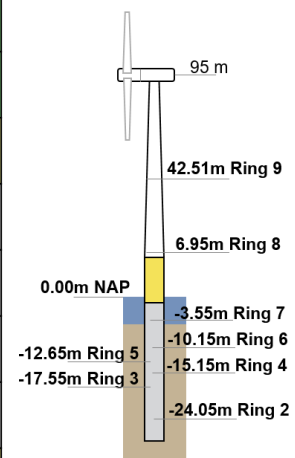


**Figure 3.15:** Non-drifting strain gauge 8C 10-min average values over time, in conditions where 10-min average wind direction is  $219.4^\circ \pm 20^\circ$  or  $39.4^\circ \pm 20^\circ$  and wind speed is 10-14 m/s.

In Fig. 3.15, roughly constant strain values allow to easily identify an appropriate range, which can then be used for calculating a moment value. The obtained value can be used for comparison with moment values from other gauges that are located at the same ring/level – see Table 3.3.

**Table 3.3:** Summary of the results from the process of deriving approximate maximum moment values from 10-min statistics of strain data for the purpose of verifying the usability of strain sensors for further analysis.

	<b>M<sub>BD</sub> : Gauge A</b>	<b>M<sub>AC</sub> : Gauge B</b>	<b>M<sub>BD</sub> : Gauge C</b>	<b>M<sub>BD</sub> : Gauge D</b>
	[MNm]	[MNm]	[MNm]	[MNm]
Ring 9	19.3	20.0	18.9	19.2
Ring 8	32.9	33.6	34.7	33.5
Ring 7	40.7	43.9	41.8	44.9
Ring 6	40.5	41.1	24.2	No data
Ring 5	34.0	35.8	34.6	No data
Ring 4	27.9	21.0	11.7	No data
Ring 3	21.8	22.8	No data	No data
Ring 2	5.55	5.95	6.55	6.00



In Table 3.3, the gauge usability from the study results are presented. A column header “ $M_{BD}$ : Gauge C” would imply that the bending moment about B(309.4°)–D(129.4°) line was calculate by assuming that gauge A readings are equal to C readings, which are multiplied by minus one. Exactly like it was demonstrated with Eq. 3.6. More on the results, five of the sensors did not provide any data to process. Drifting phenomena were identified in 13 out of the 27 working gauges, highlighted in yellow or red. Moreover, three of the sensors provided more than 20% lower values in comparison to the highest value of the respective ring and these are highlighted in red. Because the three gauge sensors (4C, 4B, and 6C) appeared to have reduced sensitivity, likely due to debonding, the data from these sensors was not used any further. The amplitude of readings is important in the data analysis in Secs. 3.4.4 and 3.5. What is more, it was found that position A gauges show the most reliable results, although at rings 2, 4, and 7 these are affected by some level of drifting. The only strain gauge rings where all sensors appear to give trustworthy results, with unnoticeable level of drifting in readings, were rings 8 and 9.

### 3.4.3 Additional Assumptions and Preprocessing for Derivation of Bending Moments

The results in Table 3.3 indicated that several sensor limitation exist and assumption were needed to proceed with moment calculations in fore-aft (FA) and side-side (SS) directions ( $M_{FA}$  and  $M_{SS}$ ). It is an integral part of the fatigue analysis in Sec. 3.5 of this report.

Since the gauges from rings 8 and 9 were seen as ‘healthy’, no modifications were required to be applied to Eq. 3.2, hence  $M_{FA}$  and  $M_{SS}$  were derived at these rings. However, due to drifting in most of the gauges at rings 2, 3, 4 and 7 only moments  $M_{BD}$  and  $M_{AC}$  with an idealizing assumption, as was first presented in Sec. 3.4.2 with Eq. 3.6, can be found. In the case of rings 5 and 6, gauges at positions A and B were deemed accurate and could thus be used to find  $M_{FA}$  and  $M_{SS}$ , by assuming that  $\epsilon_C = -\epsilon_A$  and  $\epsilon_D = -\epsilon_B$ . The aforementioned considerations are summarized in Fig. 3.16.

Rings 8 & 9

$$\delta M_{BD} = \frac{EI(\epsilon_A - \epsilon_C)}{2 \cdot y_u}$$

$$\delta M_{AC} = \frac{EI(\epsilon_D - \epsilon_B)}{2 \cdot x_u}$$

$\alpha_{yaw}$  }  $M_{FA}$   
 $M_{SS}$

Rings 7, 4, 3 & 2

$$\delta M_{BD} = \frac{EI(\epsilon_A - (-\epsilon_A))}{2 \cdot y_u}$$

$$\delta M_{AC} = \frac{EI(\epsilon_D - (-\epsilon_D))}{2 \cdot x_u}$$

Rings 5 & 6

$$\delta M_{BD} = \frac{EI(\epsilon_A - (-\epsilon_A))}{2 \cdot y_u}$$

$$\delta M_{AC} = \frac{EI((- \epsilon_B) - \epsilon_B)}{2 \cdot x_u}$$

$\alpha_{yaw}$  }  $M_{FA}$   
 $M_{SS}$

Rings 7, 3, & 2

$$\delta M_{AC} = \frac{EI((- \epsilon_B) - \epsilon_B)}{2 \cdot x_u}$$

Rings 7 & 2

$$\delta M_{BD} = \frac{EI((- \epsilon_C) - \epsilon_C)}{2 \cdot y_u}$$

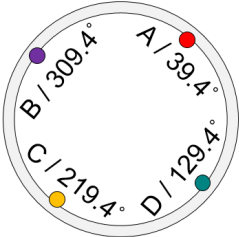


**Figure 3.16:** Summary of the adjustments and assumption made to derive moments from gauge data at each ring level, only gauges located at rings 5, 6, 8 and 9 can be used to derive  $M_{FA}$  and  $M_{SS}$  due to no apparent drifting in their readings.

The gauges that were considered usable for deriving  $M_{FA}$  and  $M_{SS}$  needed further processing by means of adjustment of the data by a constant value to avoid distorting the readings when combining two different measurements. It was identified from the 10-min average strain *versus* yaw position plot (in Fig. 3.11) that there is a constant offset, which needs to be adjusted. Thus, as shown in Fig. 3.17, the data points corresponding to wind speed level 10-14 m/s were plotted, and a sine curve was fitted to allow the identification of offset of  $-35 \mu\text{m/m}$  (Fig. 3.17a). Application of offset correction led to satisfactory results, which are shown in Fig. 3.17b, where the lowest wind speed range scatter points closely follow the zero-line and the shifts in sign occur at  $129.4^\circ$  and  $309.4^\circ$  (not visible) positions.

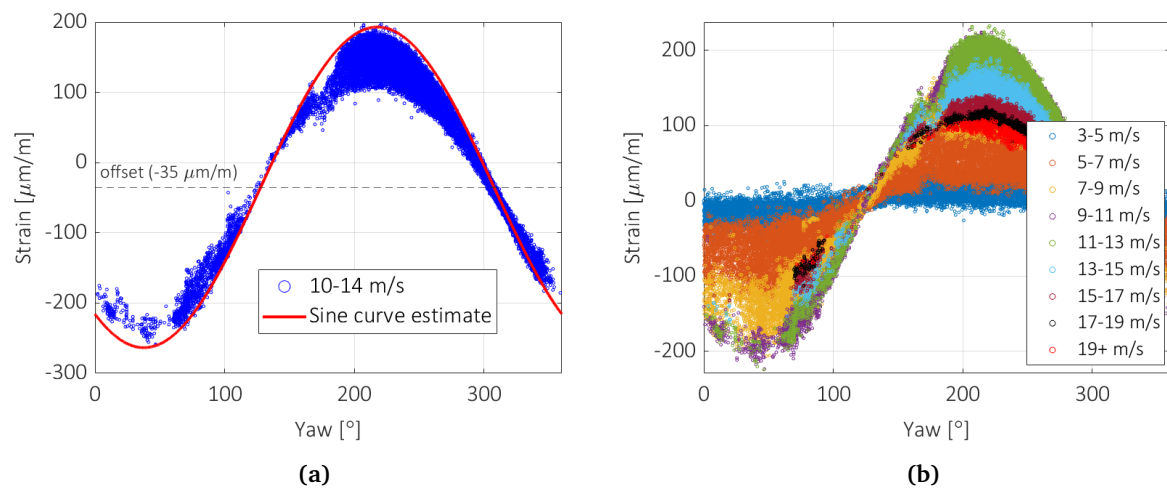


**Figure 3.17:** (a) Sine curve estimate to the curve formed from gauge 8C 10-min average values (at wind speeds 10-14 m/s) *versus* yaw position scatter plot. (b) Offset corrected strain *versus* yaw position relation per wind speed range.

### 3.4.4 Results and Comparison with Design Values

After the application of the offset correction on gauges 5A, 5B, 6A, 6B and all gauges at rings 8 and 9, FA and SS moments were derived and its 10-min maxima were then checked and compared with ULS design values.

For the verification of estimated FA and SS moments, ring 8 and 9 moment values were used. Because the OWT is located in a lake, the main source of forcing is from the wind thrust, which could be considered to be acting as a point load at the nacelle level (95 m above NAP). Hence, the ratio between ring 8 and 9 FA moments ( $M_{8FA}$  and  $M_{9FA}$ ) should be closely equal to the ratio of distances between the respective ring and nacelle level. The distance between ring 8 and nacelle level is 88.05 m and the distance from ring 9 to the nacelle is 52.495 m. The resulting ration is approximately 1.68, and by dividing each  $M_{8FA}$  data point with its corresponding  $M_{9FA}$  value, the ration should be the same (Eq. 3.7).

$$\frac{M_{8FA}}{M_{9FA}} \sim \frac{88.05}{52.495} \approx 1.68 \quad (3.7)$$

To check if the relation holds, ratios for all data points from the wind speed range of 10-14 m/s were found and plotted against their respective yaw position value - to validate consistency

of results – in Fig. 3.18. It can be seen that the relation widely holds, so results were considered acceptable. The deviations can be attributed to other load effects, sensor deviations and some level of inaccuracy in determining offset levels.

In Fig. 3.19, the approximated maximum moment values, that were presented in Table 3.3 and were not highlighted in red, are drawn over the height of the support structure. All values that were found at ring 7 (-3.55 m) – just above mudline – are the highest in the respective moment lines.

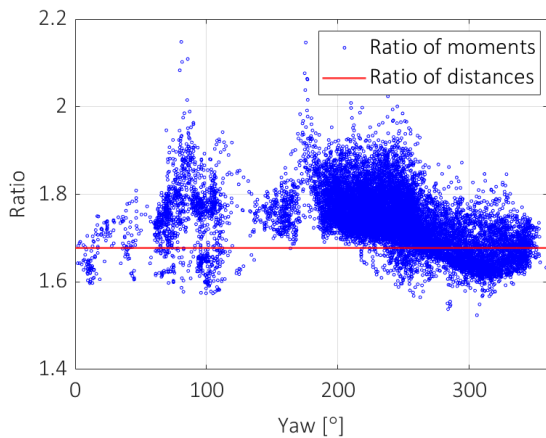


**Figure 3.18:** Ratio of  $M_{8FA}$  and  $M_{9FA}$  10-min average moment values versus 10-min average yaw position value.

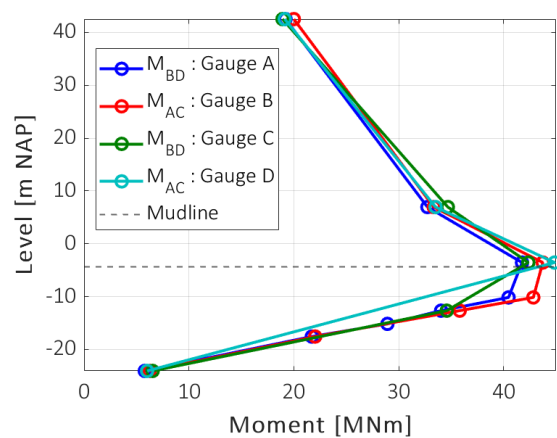


**Figure 3.19:** Approximated maximum moment lines, compiled with values from Table 3.3.

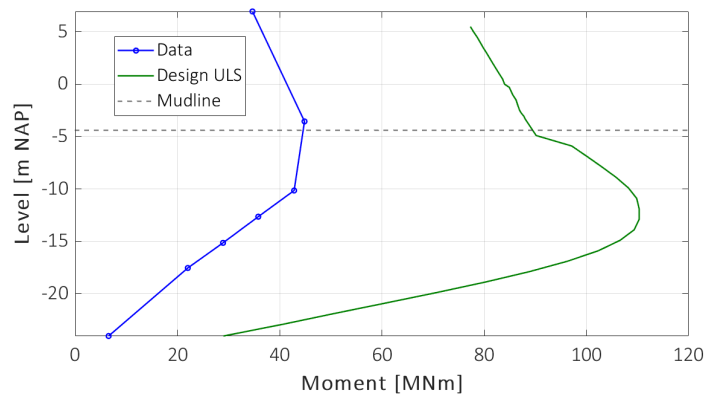


**Figure 3.20:** Comparison between approximated maximum moment line and design ULS moment line for the case with unfactored soil.

If the maximum value from each level would be considered and drawn together with the ULS design moments (in unfactored soil), Fig. 3.20 would be received. According to the measured data the highest moment occurs just near the mudline, but the design model has the peak value at -11.9 m NAP. The maximum moment value that was obtained from data is 40.7% of the ULS design peak moment value. A portion of discrepancy in the location of peak moments in the moment lines in Fig. 3.20 originates from the fact that the design ULS moment line corresponds to the worst case estimate. In the worst case design model, the mudline would be 0.5 m below the measured mudline level of -4.4 m (Fig. 3.20) and an allowance for a meter of scour was



made. Another source of discrepancy comes from modelling assumptions related to soil springs, which are defined with p-y curves that cannot capture all the particularities in the existing soil.

Having earlier affirmed the acceptability of the  $M_{FA}$  and  $M_{SS}$  values, the 10-min average moment *versus* wind speed scatterplots could be plotted. Figs. 3.21a and 3.21b include data points from all operational states of the wind turbine when the 10-min average wind speed was larger than 3 m/s. The thrust curve shape with a peak moment values near  $V_{rated}$  in Fig. 3.21a is expected. Similarly, the SS moment *versus* wind speed scatterplot has the anticipated characteristics with the moment magnitudes significantly smaller than the FA moment values. Moment values that correspond to standstill or idling states, form a horizontal line below the zero-line in Fig. 3.21a.

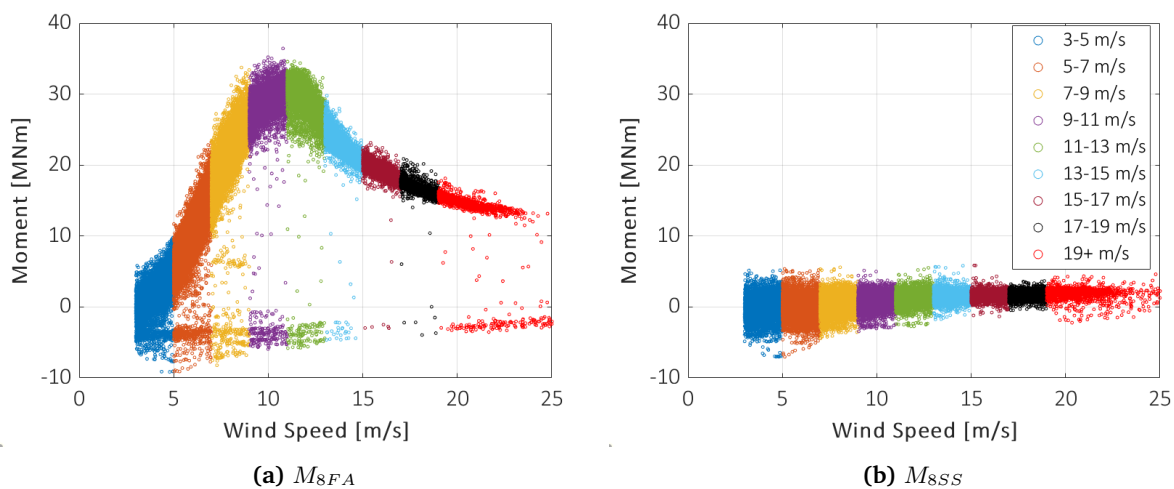


**Figure 3.21:** 10-min average bending moment *versus* wind speed at ring 8 (6.95 m above NAP).

A comparison between the idealized estimates (Figs. 3.19 and 3.20) and the maximum values from FA moment thrust curves - one of them shown in Fig. 3.21a - showed a difference of less than 8.5%. The maximum moment values can be found in Table 3.4. It must be noted that the peak values from moment *versus* wind speed plots were appearing as slight outliers and 3<sup>rd</sup> highest values were less than 3% apart with the idealized estimates from Sec. 3.4.3. As a reminder, the idealized estimates were derived with visually picked strain values. Having a good alignment between the two, the derived FA and SS moments for production conditions can be considered reliable for the process of performing the fatigue analysis. The accuracy of conversion is questionable with data recorded at standstill or idling states, as relative FA and SS moment errors can be significant due to misjudgment in determining offsets in strain gauge readings.

**Table 3.4:** Comparison between peak moment values derived from 'hand-picked' strain data values, and from the 10-min average  $M_{FA}$  and wind speed scatter plots, for rings 5, 6, 8, and 9.

Ring	Height [m NAP]	'Picked' maximum moment	Maximum from moment-wind speed plot
9	42.51	20.0 MNm	21.5 MNm
8	6.95	34.7 MNm	36.4 MNm
6	-10.15	41.1 MNm	44.5 MNm
5	-12.65	35.8 MNm	38.3 MNm

### 3.5 Fatigue Analysis

The derived moment time series can now be used to perform the fatigue analysis, which entails dissecting complex and random time series into moment cycles, which can then be used for understanding fatigue accumulation in different operational states of the wind turbine. First, the chosen fatigue analysis approach is outlined, and then M-N curves, short-term damage equivalent bending moments and damage frequency spectra are derived. Herein performed fatigue analysis is not intended to estimate the fatigue life of the turbine, thus no wind speed or turbulence weighting is applied, nor is the design life of the turbine used.

#### 3.5.1 The Rainflow Counting Method

In order to relate a moment sequence to the fatigue damage that inflicts to the material a standard cycle counting algorithm – rainflow counting – is applied on the moment-time history. Rainflow counting is a standardized procedure for determining the number of moment or stress cycles and ranges [1, 14, 23]. The chosen rainflow counting algorithm, which MATLAB provides, corresponds to the ASTM's standard [15].

Because of the long duration of the measurement campaign, the data has been stored as individual 10-min records. The rainflow cycle counting was applied to each individual 10-minute record separately, and the result was then assembled to form a single cumulative rainflow spectrum. An assumption was made here that load cycles with a period greater than ten minutes will not be considered. Thus, for example, slow variations in the wind speed may not be captured. However, the fatigue effect of these slow variations for a Vestas V112 OWT was found to be small in [48]. V112 OWT has slightly higher power output and size than W27. It has to be noted that the referenced OWT is located at a deeper offshore site and is not located in a lake like W27. Hence, influence from wave loading is increased and may have diminishing effect on the influence of slow variations in relative terms.

After shrinking a complex bending moment time histories into a series of counted constant amplitude events, the most widely used S-N or, as in the current case, M(moment)-N curves can be constructed for different operational states of the OWT. Furthermore, the analysis of the fatigue damage can be performed in terms of the damage equivalent loads (DELs), the definition of load is herein taken as bending moment. With the use of the Miner's rule [9], fatigue damage equivalent bending moment,  $M_{DEL}$ , or short-term damage equivalent bending moment,  $M_{STEL}$ , can be derived to be:

$$M_{STEL/DEL} = \left( \frac{\sum_{i=1}^{n_b} n_i \cdot M_i^m}{N_{ref}} \right)^{1/m} \quad (3.8)$$

, where  $n_b$  is the number of bins used for cycle counting;  $M_i$  is the bending moment of the  $i^{\text{th}}$  range bin of the fatigue load spectrum;  $n_i$  is the number of cycles in the  $i^{\text{th}}$  range bin of the fatigue load spectrum;  $m$  is the Woehler slope; and  $N_{ref}$  a predefined number of cycles.

In line with the values reported in the design documents of the monitored OWT,  $m$  was taken as 3 and  $N_{ref}$  for DEL calculations as  $10^7$ . However, in case of the STEL calculations,  $N_{ref}$  equals 600. STEL is considered to be the 1Hz damage equivalent bending moment for a ten minute time series [1]. Thus, STEL is found for every individual 10-min record.

To add, in the DEL and STEL calculations, the resulting half-cycles from the rainflow counting routine were taken into account with a factor of 0.5, as advised in IEC 61400-13 [1]. According

to the same standard, it is allowed not to consider the mean load effects, which have been found to increase fatigue damage, as was concluded in [7].

In the current work, the mean load effects are ignored also for two reasons. Firstly, the strain sensors were not accurately calibrated after the completion of the OWT, so knowing the mean static or mean strain/load level without an accurately calibrated computational model is complex and unfeasible. Secondly, in 13 out of 27 sensors noticeable drifting was identified – making the identification of the true mean strain/load level very difficult.

Lastly, all filtering of moment time series was performed with MATLAB's *idealfilter* [32], with considerations to the transient response effects.

### 3.5.2 M-N Curves in Characteristic Operational States

The cumulative rainflow spectra – M-N curves – require a predefined bin size to be able to construct them. According to [14] the minimum number of bins is 100. Hence, the maximum moment ranges from each moment time-series was first identified, and to have at least 100 bins in the case of the moment record at ring 2, bins with a width of 100 kNm were chosen.

The overall FA and SS moment M-N curves, in log-log scale, are shown in Fig. 3.24. These curves were derived from readings on the ring 6 (-10.15 m NAP) of the pile, where according to the design models the highest moment should occur. Additionally to the 'All'-curve, curves derived by band-pass filtering for the 0-1 Hz and 1-5 Hz range are shown. The summation of these two should ideally result in the overall line, but filtering effects cause slight discrepancies. The comparison of the two curves, reveals that the first order motion of the OWT (resonance frequency around 0.3 Hz) and response to thrust loading are responsible for the high amplitude moment cycles, as the 0-1 Hz curve follows closely the overall curve at higher moment ranges. Similarly, it can be deduced that the higher order motions are related to lower, but more frequent, moment ranges.

In case of the overall SS M-N curve, in Fig. 3.22b, there appears a distinctive top lobe, which corresponds to low-frequency dynamics. Low-frequency dynamics relates to 1<sup>st</sup> FA and SS bending modes, 1P (up to 0.258 Hz) and 3P (up to 0.775 Hz) oscillation and wind thrust. The lower lobe corresponds to the high frequency effects.

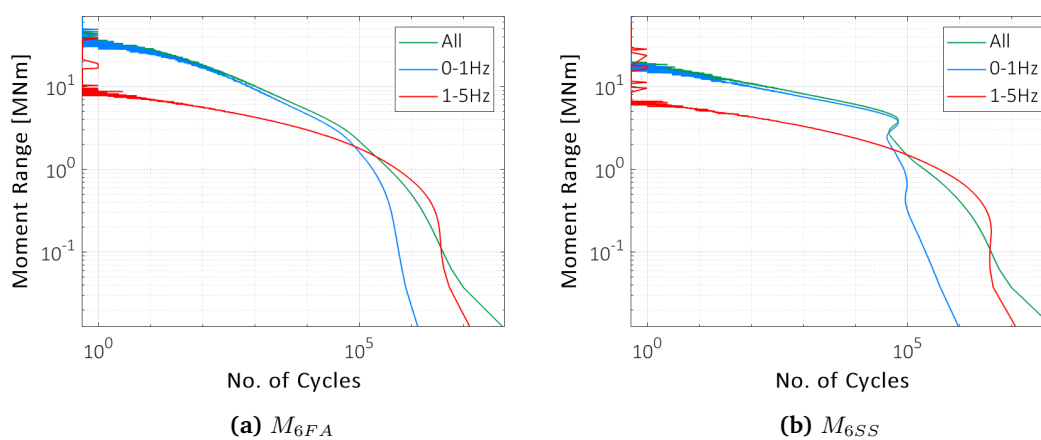


**Figure 3.22:** FA and SS motion M-N curves, from readings at ring 6 (-10.15 m NAP).

In Sec. 3.1 in Fig. 3.1a, three operational states were defined: idling, run-up, and rated. In Figs. 3.23b, 3.23c and 3.23d, the derived cumulative fatigue spectra for these three states are shown, with the overall for FA and SS motion provided in Fig. 3.23a. Some discrepancy between the three cases can be distinguished. It can be noticed that at rated conditions, SS M-N curve has two distinguishable lobes, whereas the FA curve appears to be smoothed. As was suggested in [48], this phenomenon can be related to the large aerodynamic damping in the FA direction during power production - it can be considerably stronger than SS damping [10]. Via the comparison of the curves at different conditions, it is visible that with the reduction in rotor speed, the M-N curves appear more linear on the log-log scale. This implies that the higher frequency effects are reducing, and the system's behaviour is more static.

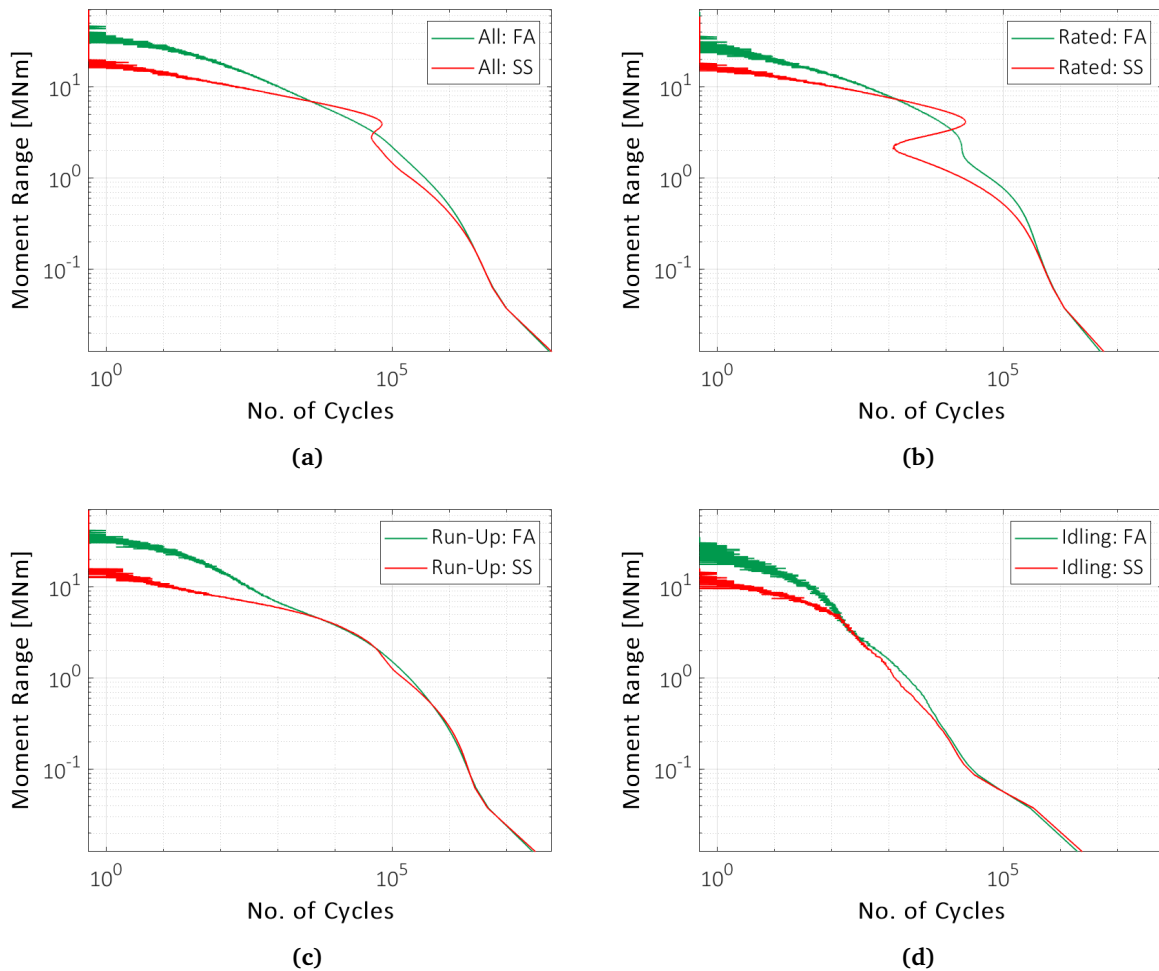


**Figure 3.23:** FA and SS motion M-N curves, from readings at ring 6, composed with data records corresponding to (a) all ; (b) rated; (c) run-up; (d) idling operational states.

The FA and SS M-N curves of the different states are plotted together in Figs. 3.24a and 3.24b, respectively, for the purpose of seeing the difference in fatigue damage from the different states relative to each other.

Both figures confirm that the idling condition, in comparison to other states, contributes more by means of low cycle high amplitude oscillations. Run-up and rated states have a higher

contribution via more high-frequent low amplitude oscillations. Although, at run-up and rated states, high amplitude low frequent oscillations do still occur.

It has to be noted that the differences in cumulative fatigue spectra on their own do not allow to assess, which of the three operational cases causes most fatigue damage. For that, the already mentioned Miner's rule could be used, but due to the fact that the turbine has been in each state for a different amount of time, it would not be very insightful without methodical scaling.

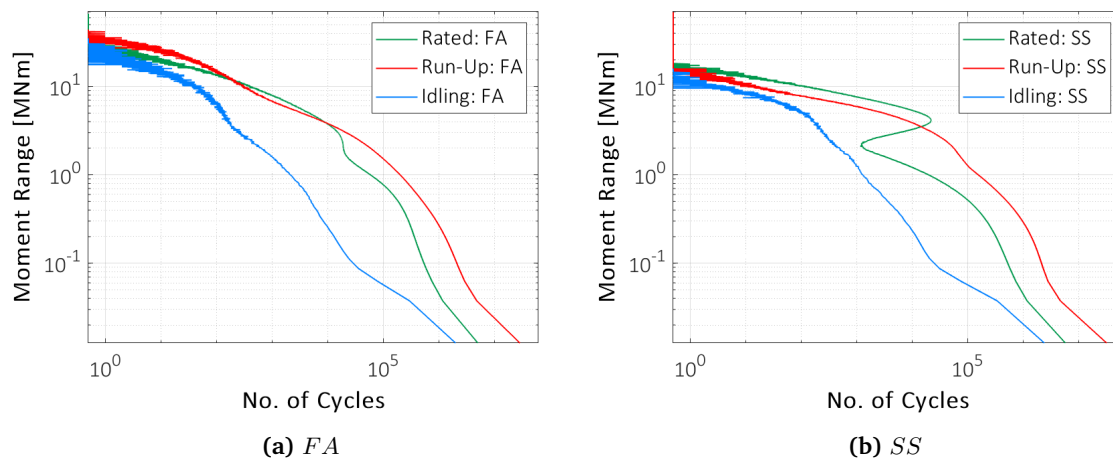


**Figure 3.24:** M-N curves, from readings at ring 6, composed with data records corresponding to rated, run-up, and idling operational states.

### 3.5.3 Damage Equivalent Load Curves

Similarly to the 10-min average static moment lines that were presented in Fig. 3.19, damage equivalent bending moment lines can be formed. Because of the drifting of some of the strain gauges and resulting restriction on transferring strains to FA and SS moments at each of the monitored OWT strain gauge rings, data filtering and approximations had to be made to arrive at approximate  $M_{FA,DEL}$  values.

The derivation of DEL started by converting strain data to  $M_{AC}$  and  $M_{BD}$ , based on Fig. 3.16. Because of the demonstrated better reliability of gauges at A and B positions at rings 2, 3, 5, 6, and 7 – only the readings from these gauges at these rings were used for the DEL calculation herein, and STEL calculation in Sec. 3.5.4. From the RNA 10-min statistical data, the time periods where the wind direction aligned with the  $39.4^\circ$ – $219.4^\circ$  (A-C directions) or  $129.4^\circ$  –  $309.4^\circ$  (B-D directions) line, were extracted and an allowance of deviation was set as  $\pm 20^\circ$ . The periods which correspond to ‘ $39.4^\circ$ – $219.4^\circ$ ’ directional conditions (Fig. 3.16), would contribute to the calculation of  $M_{BD,DEL}$ , representing approximately  $M_{FA,DEL}$  at that time period. The same logic can be applied to the contributions with periods where the wind direction aligned approximately with the  $129.4^\circ$ – $309.4^\circ$  line.

Based on the described logical filtering, damage equivalent moment lines, shown in Fig. 3.25 resulted. It is visible that the shape of the DEL lines is similar to the (quasi-)static moment lines (Fig. 3.19). Similar shapes are expected because the moment amplitudes at each ring level follow the trend in Fig. 3.19 and the number of bending moment cycles is similar at each ring. The latter holds as the response of the OWT to the main loading of wind thrust is not local to one ring only.

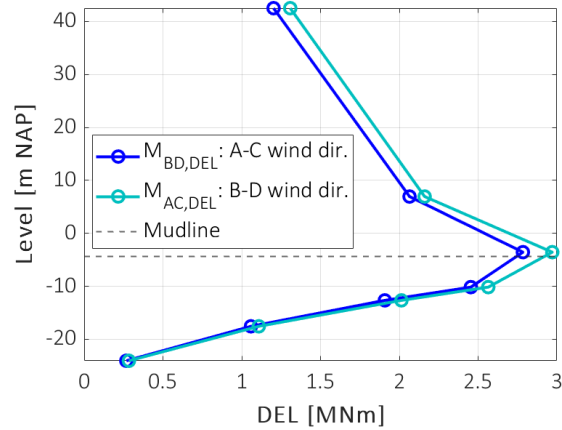


Figure 3.25: Damage equivalent bending moment curves.

### 3.5.4 Short-Term Damage Equivalent Load Relation with Wind Speed & Turbulence Intensity

The STEL relation with turbulence intensity (TI) and wind speed is explored in this subsection. Turbulence intensity is defined as the ratio of the standard deviation of wind speed and its respective mean. Because STEL values are found for a 10-min moment record, the corresponding statistical wind parameters can be directly obtained from the 10-min RNA data statistics.

It was found that FA STEL values are linearly related to the turbulence intensity if the OWT is in the run-up operational phase, see Figs. 3.26a and 3.26b. To construct these figures, the following approximations and conditions were applied:

- Only the data points corresponding to the run-up operational state were considered (defined in Table 3.2).
- Due to the limitation of transforming moments to FA and SS directions, the considered data points corresponded to periods when 10-min average wind direction aligned with either of the two lines, '39.4°–219.4°' or '129.4°–309.4°', with an allowable deviation of  $\pm 20^\circ$ .

Figure 3.26a corresponds to the  $M_{2AC,STEL}$  values (the resulting STEL value from 10-min moment,  $M_{AC}$ , record, which was derived from gauge readings at position B at ring 2), and the scattering of data points into two groups indicates another interesting relation that is also visible in Fig. 3.26b. In Fig. 1.3, the map of the wind farm was shown, including the position of the OWT. It could be noted that there are other turbines located in the directions 39.4° and 129.4° with respect to the W27 OWT. However, there are none in the 219.4° and 309.4° directions. Thus, if the wind is approaching from the East side, the turbine is located downstream. As a result of the wake effects and higher turbulence intensity, the fatigue damage on the OWT structure is, in general, higher compared to the upstream positioning - when the wind direction is from the West side.

Figure 3.27a comprises all the linear least squares fitted lines at all rings for STELs derived from  $M_{BD}$  readings. Because a linear relation was found at all rings of the turbine, it can be realized that the loading on the OWT is dominantly wind-induced. In case of significant wave-induced loading, the linear relation would not hold at lower ring levels along the SUS, unlike in the current case. What is more, the slopes of the linear lines in the figure appear

to follow the trend that has been previously revealed with damage equivalent (Fig. 3.25) and approximated (quasi-)static bending moment lines (Fig. 3.19). The trend formed with the slopes of the linear lines is presented in Fig. 3.27b. It can be explained by considering that the bending moment amplitude at each ring follows this same trend of having the peak value near the mudline (Fig. 3.19). The difference between numbers of oscillation measured at each ring cannot differ significantly as the response of the support structure is expected to be global. Thus, the STEL values and inherently the slopes of the linear lines can only form the presented trend.

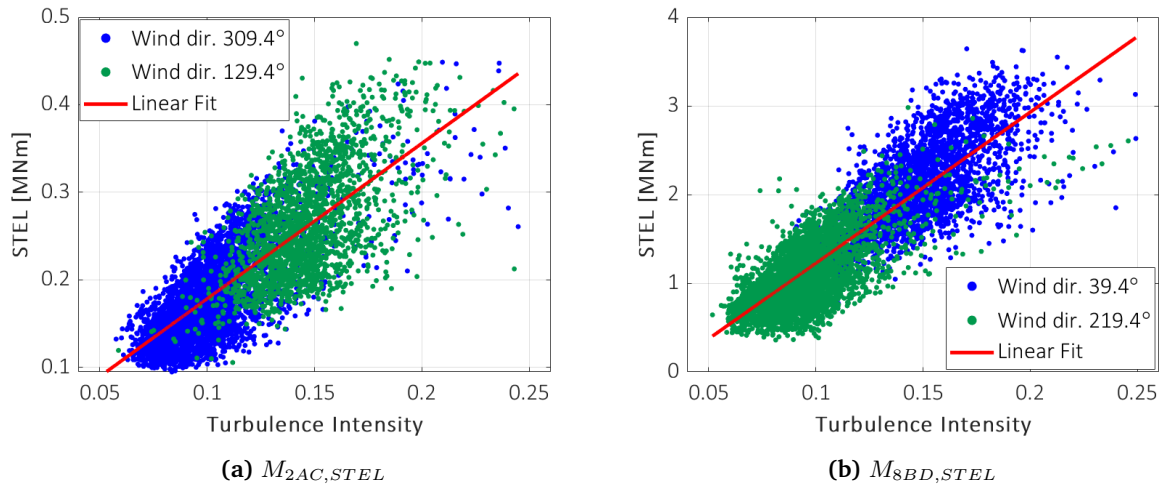


Figure 3.26: STEL values at run-up operational state in approximated FA motion conditions versus turbulence intensity.

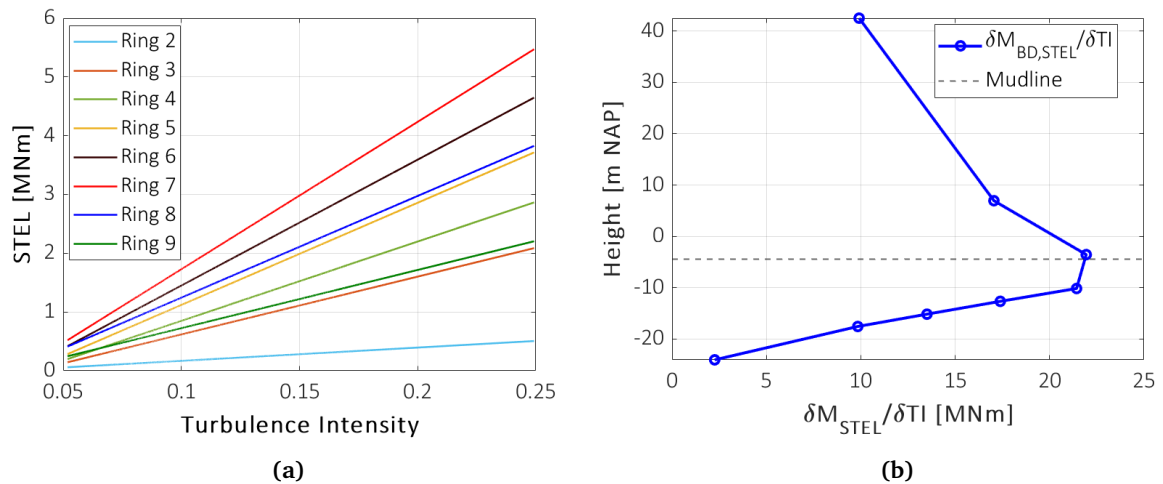
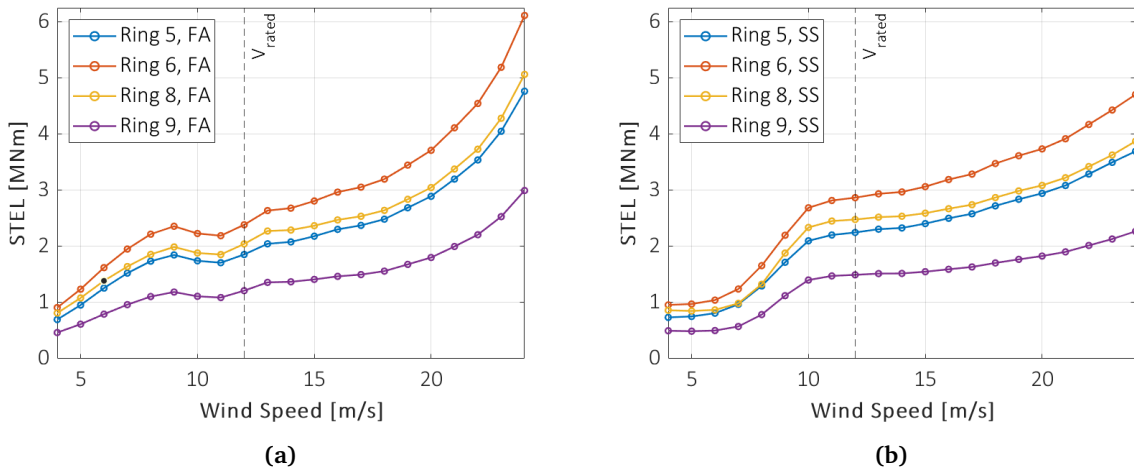


Figure 3.27: (a) Overview of the 1<sup>st</sup> order lines fitted to the  $M_{BD,STEL}$  versus  $TI$  scatter plots, where only data points corresponding to run-up operational state in approximated FA motion conditions were considered; (b) the slopes of the fitted lines plotted over the height of the SUS.

For the purpose of exploring the relation between STEL and wind speed, STEL data points, which were derived from FA and SS moment readings at rings 5, 6, 8, and 9 were considered with some additional filtering. Conditions for inclusion were set as follows: (1) 10-min minimum

rotor speed bigger than 4.5 rpm; (2) 10-min minimum wind speed bigger than 2 m/s. The reason for avoiding no production conditions was due to the chosen way of moment transformation to FA and SS directions which potentially introduces larger errors due to low excitation conditions

After determination of STEL values, these were binned according to their respective 10-min average wind speed value. The wind speed ranges were set as such: 2.5 - 3.5 m/s, 3.5 - 4.5 m/s and so forth. All the STEL values in each wind speed range were then averaged and plotted against their corresponding mid-bin (wind speed) value. The results are shown in Figs. 3.28a and 3.28b.



**Figure 3.28:** FA and SS average STEL values per wind speed range at levels 5, 6, 8 and 9; data points are located at the centre of the chosen wind speed bins.

Unlike the maximum moment *versus* wind speed curves (Fig. 3.21a), the damage equivalent bending moment continues to increase after the rated wind speed level of 12 m/s. Fore-aft STEL values show a slight drop at around  $V_{rated}$ , before the fatigue damage starts to creep up again with the increase in wind speed. The likely reason lies in the fact that at higher wind speeds, the OWT response is more dynamic – frequency of response oscillations increases. Consequently, equivalent fatigue damage increases due to higher amount of lower magnitude oscillations of W27 in FA and SS directions.

What is more, comparison between the average STEL values in Figs. 3.28a and 3.28b are of similar magnitude, unlike in (quasi-)static FA and SS bending moment *versus* wind speed plots (Figs. 3.21a and 3.21b). The results in Figs. 3.28a and 3.28b suggest that the SUS oscillations in SS direction are more frequent than in FA direction over the observed short-term periods. It was found from M-N curves in Sec. 3.5.2 that FA bending moment time series has higher amplitude cycles than SS bending moment time series. Furthermore, between the wind speed range 10 - 20 m/s in Figs. 3.28a and 3.28b, the SS STEL values are bigger than respective FA values. This can again be related to the large aerodynamic damping in the FA direction during power production [48]. Following this explanation, the aerodynamic damping in the SS direction increases noticeably more at wind speed conditions above 20 m/s, while the OWT is in production state.



### 3.5.5 Fatigue Damage Frequency Spectrum

To explore further the fatigue damage consumption over the frequency spectrum for the benefit of understanding the impact of certain dynamic events on fatigue life progression, damage equivalent bending moment calculations were coupled with a low-pass filtering routine.

Only rings 5, 6, 8, and 9 FA and SS moment records were included and production state (same as in Sec. 3.5.4) was considered. The overall routine for arriving at the results depicted in Figs. 3.29 - 3.31 included filtering the moment readings with a varying cutoff frequency, in increments of 0.02Hz from 0.02Hz to 5.00Hz. The filter was chosen as the MATLAB's low-pass 'ideal filter' for its fast computational speed and great performance. At every filtering instance, a damage equivalent bending moment value was calculated via rainflow counting and Eq. 3.8. Having obtained a total of 250 DEL values for a moment time history, the values were normalised with respect to the highest value (the value from last filtering instance) amongst these 250 DEL values, resulting a [0, 1] range to represent the consumption of fatigue damage over the frequency spectrum.

As illustrated in Fig. 3.29, FA fatigue is mainly triggered at low frequencies – at rings 6 and 8 about 68% of the total damage was inflicted in the 0 - 0.5 Hz range. In this range, the thrust load, wave loading and the first bending modes (approx. 0.3 Hz) are located, together with 1P oscillations. The rotor 3P harmonic reaches up to 0.78 Hz, where the FA curve has started to flatten. Thus, higher order dynamics bears less importance in damage equivalent FA bending moment accumulation, as the second and third SUS bending modes are located around 1.51 - 1.53 Hz, and 2.75 - 3.13 Hz respectively according to the lowest design frequency position estimates. In case of damage equivalent SS bending moment accumulation, the biggest contribution comes from low frequency thrust loading and 1P harmonics as there is a sudden change in slope at the 0.14 Hz mark. From there onwards the DEL accumulation is gradual. A slight increase in slope can be noticed near 3P highest frequency (0.78 Hz). The frequency range 0 – 1 Hz accounted for approximately 50% of the total damage.

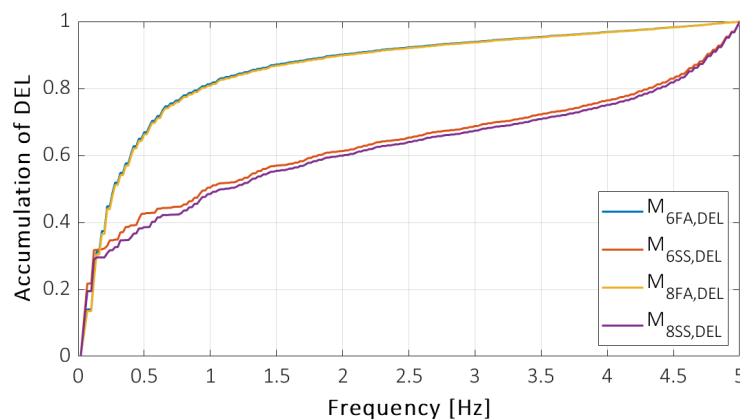


**Figure 3.29:** FA and SS fatigue damage accumulation frequency spectra at rings 6 (-10.15 m above NAP) and 8 (6.95 m above NAP).

If the damage equivalent FA and SS bending moment envelopes would be unfolded to separate DEL values per wind speed ranges and their accumulation over the frequency spectrum would be considered, Figs. 3.30 and 3.31 would be derived. In Fig. 3.30,  $M_{6FA,DEL}$  values per defined wind speed range conditions were analysed. The wind speed ranges were chosen

to have a case for below rated, at rated, and above rated wind speed conditions. It can be observed that in higher wind speed conditions, the importance of higher frequency oscillation rises, as the pronounced jump in damage accumulation at low frequencies flattens respectively. At low wind conditions, with low excitation, about 75% of the total fatigue damage is obtained by 0.5 Hz mark, whereas it is about 50% and 21% for the rated and high wind speed conditions respectively.

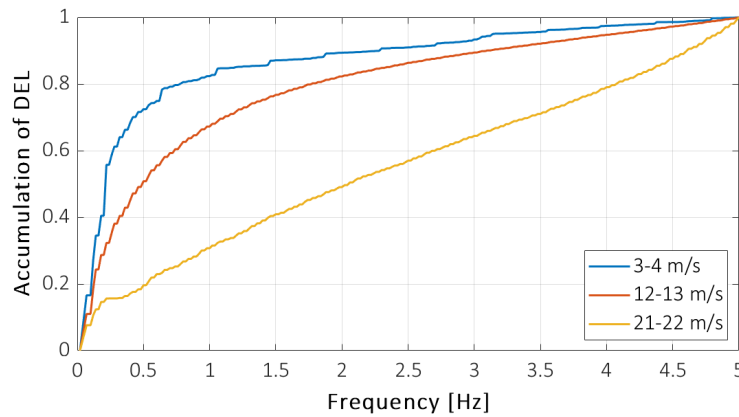


**Figure 3.30:**  $M_{6FA,DEL}$  accumulation frequency spectra at specified wind speed conditions.

Figure 3.31 provides the accumulation spectrum for the damage equivalent SS bending moments at the defined wind conditions. At light wind conditions 60% of the total damage is inflicted around 2.76 – 3.16 Hz. This region would correspond, according to the low frequency design point, to the expected 3<sup>rd</sup> SS SUS bending mode frequency range 2.75 - 3.13 Hz. At rated wind speed conditions, the 1<sup>st</sup> mode with thrust loading, wave loading and 1P oscillations have become dominant again, whereas their contribution lessens again at higher wind speed conditions. The increase in slope due to 3P harmonics at rated wind speed conditions is visible as well.

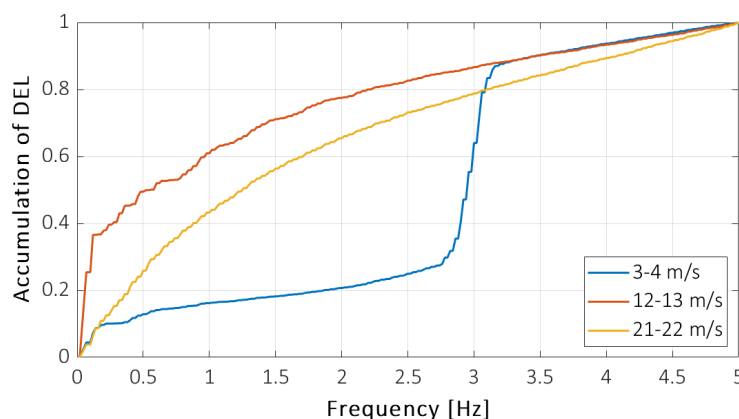


**Figure 3.31:**  $M_{6SS,DEL}$  accumulation frequency spectra at specified wind speed conditions.

Due to the appearance of significant fatigue damage accumulation at the expected 3<sup>rd</sup> SS bending mode frequency range in Fig. 3.31, additional spectra for other below rated wind speed ranges were plotted. Figure 3.32a corresponds to results from ring 6 and Fig. 3.32b to ring 8

(6.95 m above NAP). Both accumulation spectra are very similar, but the damage accumulation at low frequency range is slightly higher at ring 6. It can be explained by considering the location of ring 6 and 8. Ring 8 is positioned at a level, where the 2<sup>nd</sup> and 3<sup>rd</sup> mode shapes would have a much larger amplitude than at the position of ring 6, see Fig. 3.33. To add, the relative difference in 1<sup>st</sup> mode amplitudes between the two locations is much smaller in comparison to higher mode amplitudes.

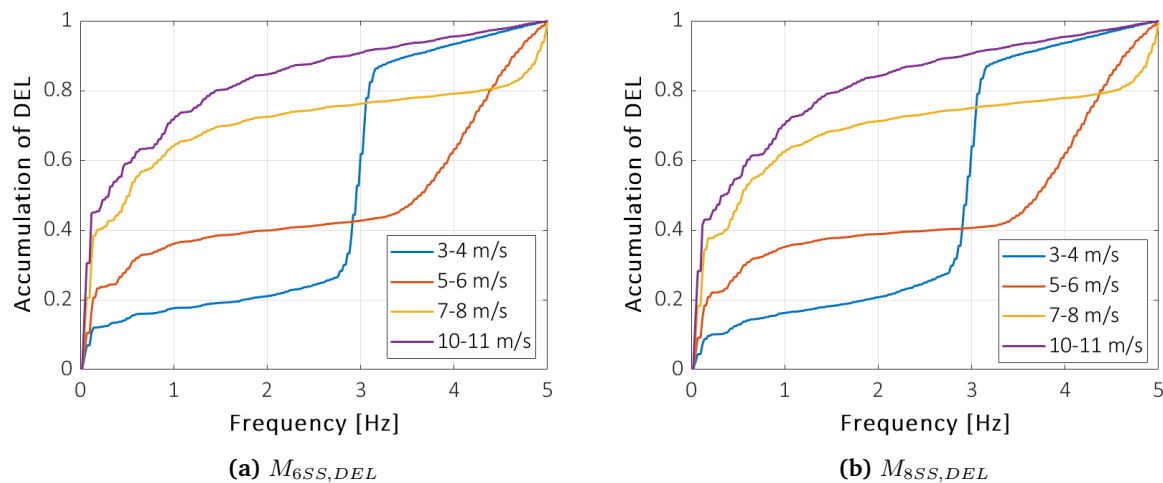


**Figure 3.32:**  $M_{6SS,DEL}$  and  $M_{8SS,DEL}$  accumulation frequency spectra at specified wind speed conditions.

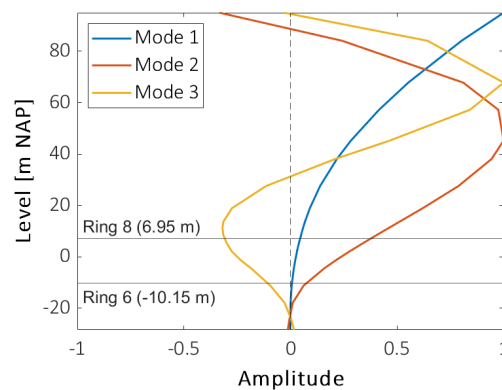


**Figure 3.33:** OWT lowest frequency design position model 1<sup>st</sup>, 2<sup>nd</sup> and 3<sup>rd</sup> mode shapes.

However, Figs. 3.32a and 3.32b show that with the increase in wind speed, significance of low frequency range increases. Also, the 60% damage gain between 2.76 - 3.16 Hz in the spectrum corresponding to 3-4 m/s wind speed conditions starts to decrease in relevance and shift towards higher frequency ranges. For instance, at 5-6 m/s wind speeds, 60% of the damage is accumulated between 3.3 – 5 Hz. This region likely also includes the presence of 3<sup>rd</sup> bending modes as W27 does not exactly correspond to low frequency design point. Additionally, in one of the DISSTINCT related studies [47] it was proposed that the 2<sup>nd</sup> soil mode is located around 5.42 Hz. The high frequency content was noticed in SUS and soil acceleration signals, which were taken from an arbitrary point in time, in Figs. 2.15a and 2.15c.

### 3.6 Summary & Discussion

The performance curves of the monitored OWT closely followed the design parameters and allowed to identify suitable data clustering for SUS data analysis as well as for RNA data analysis. Additionally the relations between environmental and operational conditions could be viewed.

Resonance frequency and side-side damping *versus* wind speed plots demonstrated a dependency – an increase in frequency is linked to an increase in damping for increased wind speeds (due to aerodynamic source). At the same time, it is to be noted that the highest and lowest resonance frequency, 0.295 Hz and 0.304 Hz respectively, fall between the design point estimates.

From the 10-min average tilt *versus* wind speed relation, in Fig. 3.5b, the anticipated thrust curve shapes were found. What is more, inclinometer data indicated that over a time span of two years, the tilt has changed about  $0.04^\circ$ . This change was investigated to have had unnoticeable influence on the monitored W27 parameters.

For the purpose of arriving at moment lines, M-N curves, DEL values and related dependencies with environmental conditions, the usability of strain gauge readings had to be checked and therefore two procedures were applied. First, the 10-min average strain values were visualized with respective yaw position per wind speed level (Fig. 3.11), with the addition of exploring the strain development over time at specific wind speed conditions (Fig. 3.13). Secondly, the amplitudes of statistical averages of strain measurement were used to evaluate sensitivity of sensors and for estimating maximum 10-min average moment values. Out of 27 working strain gauges, 13 were found to be drifting and 3 of them provided useless readings.

The previously found statistical moment values were converted into moment lines and compared with ULS design values in Fig. 3.20. As expected, the envelope of maximum bending moments across the height was much lower compared to the ULS design values. Moreover, it was noted that the measured location of peak moment did not match with the location pronounced by design model line. Reasons being that the design model corresponded to a worst-case scenario where the mudline is lowered due to excessive scour and modelling assumptions related to the soil.

After achieving an acceptable level of accuracy in the conversion of  $M_{AC}$  and  $M_{BD}$  to FA and SS moments, the cumulative rainflow spectra – M-N curves – were constructed. It was found that the low frequency (0-1 Hz band) moments account for the higher moment ranges, whereas higher frequencies are related to lower, but more frequent, moment ranges. Additionally, it could be deduced from the comparison of the M-N curves corresponding to different operational states of the wind turbine, that lower rotor speed flattens the M-N curves to a more linear line on the log-log scale (Fig. 3.23). It would suggest that the higher frequency effects are reducing respectively.

The differences in cumulative fatigue spectra on their own did not allow to assess which of the three (rated, idling, run-up) operational cases causes most fatigue damage. For that, the already mentioned Miner's rule could be used, but due to the fact that the turbine has been in each state for a different amount of time, it would not be very insightful unless some scaling parameters would be derived or it would be tried to randomly pick equal amount of time series segments for each state.

However, having the overall M-N curves, damage equivalent bending moments could be calculated using Eq. 3.8. Some assumptions and approximations had to be made in connection with the restriction on transferring moments at each strain ring level to FA and SS orientation. In the end, DEL lines that – in shape (Fig. 3.25) – aligned with the found approximated moment lines in Fig. 3.19 were derived.

Short-term equivalent bending moment values, corresponding approximately to FA motion, revealed linear dependencies with turbulence intensity, when the OWT was in the run-up operational state. The linear relation was evident at all rings of the turbine (see Fig. 3.26 and 3.27a) – suggesting that the loading of the wind turbine is dominated by wind thrust, and wave action is minor since the OWT is located in a lake after all.

Following the thread on positioning of the herein studied OWT, other OWTs are located to the East, South and North of it. From the shown STEL *versus* TI plots (Figs. 3.26a and 3.26b), it was noted that the STEL values were smaller when the wind was approaching from the West side of the turbine – meaning that it was the upstream turbine. As a result, it can be concluded that the downstream wake effects and consequent likely higher turbulence intensity leads to increased consumption of OWT fatigue life, in comparison to upstream positioning. Knowing that the dominating wind direction in the wind farm is between  $190^\circ - 300^\circ$ , the monitored OWT is mainly located upstream, thus on the safe side.

Studies on fatigue damage accumulation over the frequency spectrum demonstrated that FA fatigue is triggered at low frequencies, with approximately 68% of the total damage inflicted in the 0-0.5 Hz range (Fig. 3.29). In this range, the thrust load, wave load (identified to be small) and the first structural modes (approx. 0.3 Hz) are located, together with 1P oscillation. In the case of damage equivalent SS bending moment accumulation, the 50% of the damage was accumulated over 0-1 Hz frequency band.

Determination of damage equivalent bending moment accumulation at different wind speed conditions, revealed that the FA motion fatigue accumulation would reduce in the lower frequency band with the increase in wind speed. An unexpected result came from SS DEL accumulation curves (Figs. 3.31, 3.32a and 3.32b), where it was seen that at light wind conditions significant amount of damage is inflicted at high frequencies. However, the actual contribution of light wind conditions to the overall SS motion DEL value is limited, as the pronounced jumps in fatigue damage gain were diminished in Fig. 3.29.

With regards to the interplay between loading amplitude and response frequency, the shown wind speed dependent damage equivalent FA and SS bending moment accumulation curves over the frequency spectra (Fig. 3.30), the discovered averaged  $M_{FA,STEL}$  or  $M_{SS,STEL}$  *versus* wind speed relation (Fig. 3.28), and the 10-minute average FA moment curves (Fig. 3.21a) could be consulted. The latter showed that loading amplitude peaks at  $V_{rated}$ , and starts to decrease after that. The increasing trend of STEL values with wind speed indicated that although the moment amplitudes might be decreasing, the oscillatory action of the OWT increases. As a reminder, the damage equivalent load is a scaled relation between number of oscillations and its amplitudes. Lastly, FA DEL accumulation at higher than rated wind speed conditions was seen to possess a higher share of gain in the high frequency part than at rated wind speed conditions - higher frequency would translate to more oscillations.



## Chapter 4

# Conclusions & Recommendations

### 4.1 Conclusions

Before the formulation of objectives for this research project, several motives were identified. It was recognized that fatigue is one of the main design criteria for offshore structures and additional knowledge about fatigue cumulative development under random loading is desired. Additionally, it was acknowledged that fatigue is a complex phenomenon that is influenced by multiple of variables such as damping, resonance frequency of the OWT, loading types. With the availability of more than two and half years of extensive measurement data, the following two objectives were set:

1. Preprocess measured data and evaluate the fatigue damage accumulation of a monopile-supported offshore wind turbine under normal operating conditions.
2. Identify parameters that influence the fatigue accumulation and the resonance frequency of a monopile-supported offshore wind turbine.

With respect to the first objective, the following conclusions were reached:

- As part of the preprocessing of data, synchronization of the three - SUS, RNA and soil – data sets was required. A significant time-dependent lag was identified between SUS data and the other two sets (Secs. 2.2.2 and 2.2.3) The underlying reasons for the presence of time-dependent lag were not able to be determined, as the SUS and soil DAQ system have now been dismantled.
- Stretching of SUS data readings proved to be an appropriate method for removing the lag and synchronizing all data sets (Figs. 2.12, 2.21 and 2.23).
- After synchronization, preprocessing continued by assessing the quality of strain readings from all strain gauges (Sec. 3.4.2). Drifting of strain signals in 13 out of 27 gauges was identified and three of the gauges provided unusable readings. The occurrence of drift may have been caused by debonding of gauges from the pile surface and endured damage during the driving of the pile. The exact reasons are unknown as there are no records of the status of strain gauges prior to their removal.

Conclusions that were drawn in connection with the second objective of seeking interdependencies were the followings:

- In production state, the resonance frequency of W27 increases with a similar trend as side-side logarithmic decrement estimates for increased wind speeds (Figs. 3.4a and 3.3b). According to the trend, at noticeable increase in data values occurs between wind speeds 10 to 20 m/s. The identified dependency and similarity stemmed from the computational model, which is used for the determination of resonance frequency and side-side logarithmic decrement estimates. In the model, damping is defined to be predominantly stiffness proportional.
- Increase in damping estimates in relation with increase in wind speed was associated with increased level of aerodynamic damping due to change in pitch of the blades.
- From the observations on cumulative rainflow spectra – M-N curves – it was found that the low frequency (0-1 Hz band) moments account for the higher moment ranges, whereas higher frequencies are related to lower, but more frequent, moment ranges (Sec. 3.5.2). It was proposed that due to high FA aerodynamic damping, the distinctive top lobe, which is visible in SS M-N curves, is not apparent in FA M-N curves (Fig. 3.24).
- Fore-aft direction STEL values revealed a linear dependency with TI at all monitored levels of the SUS when the OWT was in the run-up operational state. Thus, the loading on the OWT is dominated by wind thrust (Fig. 3.26). This is explained by the fact that Westermeerwind wind park is located in a lake, where wave action is not significant.
- STEL *versus* TI relations (Fig. 3.26) showed that in wind conditions when W27 is a downstream turbine, the consumption of fatigue life is increased due to downstream wake effects. W27 can be considered a downstream turbine when wind is approaching from the East side.
- In production state fatigue life consumption of OWT SUS increases above rated wind speed conditions (Fig. 3.28a). It occurs despite a decrease in load magnitude (Fig. 3.21a), which is caused by increased pitch position of the blades (Fig. 3.1c). Increased pitch angle of blades leads to increased aerodynamic damping (Sec. 3.2) and reduced loading. The increase in fatigue damage is, thus, caused by increase in SUS response frequency, which translates to increased number of oscillations and moment cycles. Fatigue damage is a combination of bending moment amplitude and number of moment cycles (Eq. 3.8).
- At rings 6 (-10.15 m above NAP) and 8 (6.95 m above NAP), most fatigue has accumulated over the low frequency band (0-1 Hz). The percentage values for FA and SS fatigue are approximately 81% and 51% respectively (Fig. 3.29). The low frequency band is associated with wind loading, wave loading, 1<sup>st</sup> FA and SS SUS bending modes, 1P and 3P oscillations. The high frequency band (1-5 Hz) is associated with rotor harmonics and higher SUS bending modes.
- At ring 6, FA and SS damage equivalent bending moment frequency spectra were additionally derived per wind speed ranges (Figs. 3.30, 3.31). The examined wind speed ranges were 3-4 m/s, 12-13 m/s and 21-22 m/s. Fore-aft fatigue damage accumulation frequency spectra revealed that at higher wind speeds the importance of higher frequency oscillations rises. The same conclusion was found from the comparison of SS DEL accumulation spectra which corresponded to wind speeds 12-13 m/s and 21-22 m/s (Fig. 3.31). However, at wind speeds 3-4 m/s, most fatigue damage was accumulated in the frequency range that corresponds to 3<sup>rd</sup> SUS bending modes. The contribution of fatigue damage from 3-4



m/s wind speed conditions to the overall DEL value was concluded to be small. But, it was highlighted that it is important to consider SUS bending modes, which lie in the high frequency band, in the fatigue design analysis.

## 4.2 Recommendations

The recommendations for future work stem from ideas that were left out of the scope of the current research. Also, ideas that were considered as alternatives to the chosen research direction are recommended:

- In the process of synchronization of SUS data with RNA data in Ch. 2, the lag increase rate was idealised to be constant over three “correction periods”. The parameters for the “correction periods” were based on the results of lag identification on the three study periods. The total duration of the study periods was approximately 14 days, although the total overlap between RNA data time series and SUS data is about 1.3 years. Additionally, the corrections were applied on SUS data that was collected over a period of 2.5 years. Thus, in the case of using data from outside the three study periods (“March 2016, “January 2017” and “July 2017”) additional lag identification studies would be recommended if close alignment of data is required.
- During lag identification studies, the frequency content of strain and acceleration signals was explored (Secs. 2.2.2 and 2.2.3). Common higher energy frequency bands were identified between the data sets. Hence, there is potential to study dynamic soil-structure interaction (SSI) and attempt identify soil damping. Both aims would link to previous studies, where monopile-only system under shaker excitation was investigated [47, 25]. Similar studies for the operational W27 have not been performed yet, but can yield more insightful results as shaker-induced excitation was noted to be small in comparison to loading levels in fully operational state [47]. With the presence of higher loading, it may be possible to identify soil damping and soil modes [47]. Some difficulties may stem from the fact that time-dependent lag was identified between the original SUS and soil data (Sec. 2.2.3). As part of the current work, the synchronization has been achieved to an approximate level of  $\pm 1.2$  seconds (Fig. 2.21).
- What is more, the justification of higher energy frequency bands in Secs. 2.2.2 and 2.2.3 and the shapes of DEL accumulation frequency spectra curves in Sec. 3.5.5 were based on results from models that were not specific to W27. Instead, information regarding SUS bending modes corresponded to farm-wide lowest frequency design position model. The first bending mode frequency estimates from the design model provided approximately 8.3% lower values than the resonance frequency values in RNA data statistics (Sec. 3.2). Thus, to verify that correct conclusions were drawn, W27 specific modelling and modal analysis would be recommended. Existing lowest and highest frequency design position models could be adopted for the purpose.
- The performed fatigue analysis, in Sec. 3.5, was not intended to estimate the fatigue life of the turbine nor to provide a comparison with actual design values. However, as future work, these actions should be done for the purpose of verifying if real measurements align with fatigue design assumptions and DEL values. In the case where residual fatigue life is identified from the comparison of data and design values, a case for wind-farm

lifetime extension can start to be built. An additional recommendation would be to build a predictive computational model of W27 fatigue life consumption, based on published studies such as [21, 30, 27]. The found linear dependency between FA STEL and TI in OWT run-up operational state (Fig. 3.26) could form a good basis for the predictive model validation. The availability of detailed information about the soil parameters and W27 design, together with approximately two years of synchronized measurement data allow to construct trained in-depth model.

# Bibliography

- [1] IEC 61400-13. Wind turbines - part 13: Measurement of mechanical loads. Standard, International Electrochemical Commission, Geneva, Switzerland, 12 2015.
- [2] International Energy Agency. Projected Costs of Generating Electricity. <https://www.iea.org/reports/projected-costs-of-generating-electricity-2020>, 2020. [Online; accessed: 4-January-2021].
- [3] D. Amar Bouzid, S. Bhattacharya, and L. Otsmane. Assessment of natural frequency of installed offshore wind turbines using nonlinear finite element model considering soil-monopile interaction. *Journal of Rock Mechanics and Geotechnical Engineering*, 10(2):333 – 346, 2018.
- [4] Japan Wind Association. JWSA Report Detail. [http://jwsa.jp/page\\_301\\_englishsite/jwsa/detail\\_e.html](http://jwsa.jp/page_301_englishsite/jwsa/detail_e.html), 2020. [Online; accessed: 6-January-2021].
- [5] H. Badouard. Global Energy Trends Quarterly Updates. <https://www.enerdata.net/publications/reports-presentations/world-energy-trends.html>, 2020. [Online; accessed: 5-January-2021].
- [6] R. Bi, C. Zhou, and D.M. Hepburn. Detection and classification of faults in pitch-regulated wind turbine generators using normal behaviour models based on performance curves. *Renewable Energy*, 105:674 – 688, 2017.
- [7] J. Blasques and A. Natarajan. Mean load effects on the fatigue life of offshore wind turbine monopile foundations. *Computational Methods in Marine Engineering V - Proceedings of the 5th International Conference on Computational Methods in Marine Engineering, MARINE 2013*, pages 818–829. International Center for Numerical Methods in Engineering, 2013.
- [8] B. Byrne, R. Mcadam, H. Burd, G. Houlby, C. Martin, W. Beuckelaers, L. Zdravkovic, D.M.G. Taborda, D. Potts, R. Jardine, E. Ushev, T. Liu, D. Abadias, K. Gavin, D. Igoe, P. Doherty, J. Gretlund, A.M. Pacheco, A. Wood, and M. Plummer. PISA: New design methods for offshore wind turbine monopiles. *Conference: 8th International Conference for Offshore Site Investigation and Geotechnics*, London, UK, 9 2017.
- [9] O. Castro, P. Berring, K. Branner, C.F. Hvejsel, S.C. Yeniceli, and F. Belloni. Bending-moment-based approach to match damage-equivalent strains in fatigue testing. *Engineering Structures*, 226:111325, 2021.
- [10] C. Chen and P. Duffour. Modelling damping sources in monopile-supported offshore wind turbines. *Wind Energy*, 21(11):1121–1140, 2018.

- [11] European Commission. Boosting Offshore Renewable Energy for a Climate Neutral Europe. [https://ec.europa.eu/commission/presscorner/detail/en/ip\\_20\\_2096](https://ec.europa.eu/commission/presscorner/detail/en/ip_20_2096), 2020. [Online; accessed: 8-January-2021].
- [12] European Commission. State of the Union: Commission raises climate ambition and proposes 55% cut in emissions by 2030. [https://ec.europa.eu/commission/presscorner/detail/en/IP\\_20\\_1599](https://ec.europa.eu/commission/presscorner/detail/en/IP_20_1599), 2020. [Online; accessed: 7-January-2021].
- [13] Global Wind Energy Council. Global Offshore Wind Report 2020. <https://gwec.net/wp-content/uploads/2020/12/GWEC-Global-Offshore-Wind-Report-2020.pdf>, 2020. [Online; Accessed: 4-January-2021].
- [14] DNVGL-RP-C203. Fatigue design of offshore steel structures. Standard, Det Norske Veritas and Germanischer Lloyd, Oslo, Norway, 9 2019.
- [15] ASTM E1049-85. Standard practices for cycle counting in fatigue analysis. Standard, ASTM International, West Conshohocken, PA, 2017.
- [16] D.J.M Fallais. Synchronization case studies: long term consistency tests. Internal communication, 2019.
- [17] S&P Global. How is COVID-19 Impacting the Energy Transition? [https://www.spglobal.com/en/research-insights/featured/how-is-covid-19-impacting-the-energy-transition?utm\\_campaign=corporatepro&utm\\_medium=contentdigest&utm\\_source=EnergyTransition\\_COVID19](https://www.spglobal.com/en/research-insights/featured/how-is-covid-19-impacting-the-energy-transition?utm_campaign=corporatepro&utm_medium=contentdigest&utm_source=EnergyTransition_COVID19), 2020. [Online; Accessed: 4-January-2021].
- [18] HBM. Drift in bonded foil strain gauge-based sensors. <https://www.hbm.com/en/6218/drift-in-bonded-foil-strain-gauge-based-sensors/>, 2020. [Online; accessed: 11-November-2020].
- [19] M. Henkel, N. Noppe, W. Weijtjens, and C. Devriendt. Sub-soil strain measurements on an operational wind turbine for design validation and fatigue assessment. *Journal of Physics: Conference Series*, 1037:052032, 6 2018.
- [20] IEA. Global Energy Review 2020. Paris, France, 7 2020. IEA.
- [21] A. Iliopoulos, W. Weijtjens, D. Van Hemelrijck, and C. Devriendt. Fatigue assessment of offshore wind turbines on monopile foundations using multi-band modal expansion. *Wind Energy*, 20(8):1463–1479, 2017.
- [22] IRENA. *Renewable Power Generation Costs in 2019*. International Renewable Energy Agency, Abu Dhabi, 2020.
- [23] H. Karadeniz. *Stochastic Analysis of Offshore Steel Structures*, chapter 5, pages 287–314. Springer-Verlag London, 1 edition, 2013.
- [24] K. Kazemi, M. Amirian, and M.J. Dehghani. The S-transform using a new window to improve frequency and time resolutions. *Signal, Image and Video Processing*, 8:533–541, 3 2014.
- [25] E. Kementzetzidis, A.V. Metrikine, W.G. Versteijlen, and F. Pisanò. Frequency effects in the dynamic lateral stiffness of monopiles in sand: insight from field tests and 3D FE modelling. *Géotechnique*, pages 1–14, 2020.

- [26] A. Kusiak and A. Verma. Monitoring wind farms with performance curves. *IEEE Transactions on Sustainable Energy*, 4(1):192–199, 2013.
- [27] J.H. Lee. Fatigue assessment of offshore wind turbines using measurements of individual turbines and machine learning techniques. diploma thesis, Delft University of Technology, 7 2019.
- [28] L. Lombardi, S. Bhattacharya, and D.M. Wood. Dynamic soil–structure interaction of monopile supported wind turbines in cohesive soil. *Soil Dynamics and Earthquake Engineering*, 49:165 – 180, 2013.
- [29] G. Machan and V.G. Bennett. *Use of Inclinometers for Geotechnical Instrumentation on Transportation Projects*. Transportation Research Board, Washington DC, US, 10 2008.
- [30] K. Maes, G. De Roeck, G. Lombaert, A. Iliopoulos, D. Van Hemelrijck, C. Devriendt, and P. Guillaume. Continuous strain prediction for fatigue assessment of an offshore wind turbine using kalman filtering techniques. In *2015 IEEE Workshop on Environmental, Energy, and Structural Monitoring Systems (EESMS) Proceedings*, pages 44–49, 2015.
- [31] N. Martin. Big oil splutters - how will it survive the energy transition? *Deutsche Welle*, 11 2020. <https://www.dw.com/en/how-are-oil-companies-dealing-with-the-shift-to-renewables/a-55542378> [Online; accessed: 4-January-2021].
- [32] MathWorks. idealfilter. <https://nl.mathworks.com/help/matlab/ref/timeseries.idealfilter.html>, 2020. [Online; accessed: 21-December-2020].
- [33] MathWorks. interp1. <https://nl.mathworks.com/help/matlab/ref/interp1.html>, 2020. [Online; accessed: 6-January-2021].
- [34] MathWorks. *Signal Processing Toolbox User’s Guide*. MathWorks, Massachusetts, USA, 3 2020.
- [35] MathWorks. Statistical signal processing. In *Signal Processing Toolbox User’s Guide*, chapter 7, pages 196–198. MathWorks, Massachusetts, USA, 3 2020.
- [36] L. Middelweerd. Sensitivity analysis of the first natural frequency of the offshore wind turbines in the Eneco Luchterduinen wind farm. diploma thesis, Delft University of Technology, 12 2017.
- [37] G. Nikitas, N.J. Vimalan, and S. Bhattacharya. An innovative cyclic loading device to study long term performance of offshore wind turbines. *Soil Dynamics and Earthquake Engineering*, 82:154 – 160, 2016.
- [38] N. Noppe, A. Iliopoulos, W. Weijtjens, and C. Devriendt. Full load estimation of an offshore wind turbine based on SCADA and accelerometer data. *Journal of Physics: Conference Series*, 753:072025, 9 2016.
- [39] Omega. Strain gauge: Introduction to strain gauges. <https://www.omega.nl/prodinfo/strain-gauges.html>. [Online; accessed: 11-November-2020].

- [40] Rijkswaterstaat. Frequently asked questions about the ijsselmeer project. <https://www.rijkswaterstaat.nl/water/projectenoverzicht/ijsselmeer-zoetwatervoorraad-op-peil/veelgestelde-vragen.aspx>, 2018. [Online; accessed: 16-January-2021].
- [41] X.-N. Rong, R.-Q. Xu, H.-Y. Wang, and S.-Y. Feng. Analytical solution for natural frequency of monopile supported wind turbine towers. *Wind and Structures, An International Journal*, 25:459–474, 11 2017.
- [42] RVO. Efficient support structure design through improved dynamic soil structure interaction modeling. <https://www.rvo.nl/subsidies-regelingen/projecten/efficient-support-structure-design-through-improved-dynamic-soil-structure-interaction-modeling>, 2013. [Online; accessed: 30-January-2021].
- [43] E.N. Strømmen. *Structural Dynamics*, chapter 9, pages 355–408. Springer, Cham, 1 edition, 2014.
- [44] Q. Sun, C. Liu, and C. Zhen. Abnormal detection of wind turbine operating conditions based on state curves. *Journal of Energy Engineering*, 145(5):06019001, 2019.
- [45] W.G. Versteijlen. *Identification of effective 1D soil models for large-diameter offshore wind turbine foundations based on in-situ seismic measurements and 3D modelling*. PhD thesis, Delft University of Technology, Delft, NL, 2018. <https://doi.org/10.4233/uuid:55e7ff00-02ba-495d-9863-889bb92ee548>.
- [46] W.G. Versteijlen, A.V. Metrikine, and K.N. van Dalen. A method for identification of an effective winkler foundation for large-diameter offshore wind turbine support structures based on in-situ measured small-strain soil response and 3D modelling. *Engineering Structures*, 124:221 – 236, 2016.
- [47] W.G. Versteijlen, F.W. Renting, P.L.C. van der Valk, J. Bongers, K.N. van Dalen, and A.V. Metrikine. Effective soil-stiffness validation: Shaker excitation of an in-situ monopile foundation. *Soil Dynamics and Earthquake Engineering*, 102:241 – 262, 2017.
- [48] W. Weijtjens, N. Noppe, A. Iliopoulos, and C. Devriendt. Monitoring the consumed fatigue life on three offshore wind turbines. pages 2809–2816, Stanford University, Stanford, CA-USA, 9 2015.
- [49] A.B. Wilson. Offshore wind energy in Europe. *European Parliament*, 11 2020. [https://www.europarl.europa.eu/RegData/etudes/BRIE/2020/659313/EPRS\\_BRI\(2020\)659313\\_EN.pdf](https://www.europarl.europa.eu/RegData/etudes/BRIE/2020/659313/EPRS_BRI(2020)659313_EN.pdf) [Online; accessed: 4-January-2021].
- [50] Wind Europe. Offshore wind in Europe: Key trends and statistics 2019. <https://windeurope.org/wp-content/uploads/files/about-wind/statistics/WindEurope-Annual-Offshore-Statistics-2019.pdf>, 2020. [Online; accessed: 15-January-2021].
- [51] L. Zhang and X. Wu. On the application of cross correlation function to subsample discrete time delay estimation. *Digital Signal Processing*, 16(6):682 – 694, 2006.



